

**UNICAMP**

UNIVERSIDADE ESTADUAL DE  
CAMPINAS

Instituto de Física “Gleb Wataghin”

PAULO SERGIO PIVA

**Ondas gravitacionais e o espaço-tempo de  
Robinson-Trautman**

**Gravitational waves and Robinson-Trautman  
spacetimes**

Campinas

2021

Paulo Sergio Piva

## **Gravitational waves and Robinson-Trautman spacetimes**

### **Ondas gravitacionais e o espaço-tempo de Robinson-Trautman**

Dissertação apresentada ao Instituto de Física “Gleb Wataghin” da Universidade Estadual de Campinas como parte dos requisitos exigidos para a obtenção do título de Mestre em Física, na área de Física.

Dissertation presented to the Institute of Physics “Gleb Wataghin” of the University of Campinas in partial fulfillment of the requirements for the degree of Master in Physics, in the area of Physics.

Supervisor/Orientador: Alberto Vazquez Saa

Este exemplar corresponde à versão final da Dissertação defendida pelo aluno Paulo Sergio Piva e orientada pelo Prof. Dr. Alberto Vazquez Saa.

Campinas

2021

Ficha catalográfica  
Universidade Estadual de Campinas  
Biblioteca do Instituto de Física Gleb Wataghin  
Lucimeire de Oliveira Silva da Rocha - CRB 8/9174

P688g Piva, Paulo Sergio, 1997-  
Gravitational waves and Robinson-Trautman spacetimes / Paulo Sergio Piva. – Campinas, SP : [s.n.], 2021.

Orientador: Alberto Vazquez Saa.  
Dissertação (mestrado) – Universidade Estadual de Campinas, Instituto de Física Gleb Wataghin.

1. Ondas gravitacionais. 2. Espaço-tempo de Robinson-Trautman. 3. Colisões frontais. 4. Buracos negros (Astronomia). 5. Condição inicial de Brill-Lindquist. 6. Recuo gravitacional. 7. Métodos de Galerkin. I. Saa, Alberto Vazquez, 1966-. II. Universidade Estadual de Campinas. Instituto de Física Gleb Wataghin. III. Título.

Informações para Biblioteca Digital

**Título em outro idioma:** Ondas gravitacionais e o espaço-tempo de Robinson-Trautman

**Palavras-chave em inglês:**

Gravitational waves

Robinson-Trautman spacetimes

Head-on collisions

Black holes (Astronomy)

Brill-Lindquist initial data

Gravitational recoil

Galerkin methods

**Área de concentração:** Física

**Titulação:** Mestre em Física

**Banca examinadora:**

Alberto Vazquez Saa [Orientador]

Ricardo Antonio Mosna

George Emanuel Avraam Matsas

**Data de defesa:** 31-03-2021

**Programa de Pós-Graduação:** Física

**Identificação e informações acadêmicas do(a) aluno(a)**

- ORCID do autor: <https://orcid.org/0000-0002-8239-970X>

- Currículo Lattes do autor: <http://lattes.cnpq.br/6345843620075261>

MEMBROS DA COMISSÃO JULGADORA DA DISSERTAÇÃO DE MESTRADO DE **PAULO SERGIO PIVA – RA 175605** APRESENTADA E APROVADA AO INSTITUTO DE FÍSICA “GLEB WATAGHIN”, DA UNIVERSIDADE ESTADUAL DE CAMPINAS, EM 31 / 03 / 2021.

**COMISSÃO JULGADORA:**

- **Prof. Dr. Alberto Vazquez Saa – Orientador – IMECC/UNICAMP**
- **Prof. Dr. Ricardo Antonio Mosna – IMECC/UNICAMP**
- **Prof. Dr. George Emanuel Avraam Matsas – IFT/UNESP**

**OBS.:** Ata da defesa com as respectivas assinaturas dos membros encontra-se no SIGA/Sistema de Fluxo de Dissertação/Tese e na Secretaria do Programa da Unidade.

# Acknowledgements

I would like to dedicate this work to all the Teachers and Professors who helped me to understand how knowledge can be beautiful and pleasant, inspiring me to go ahead with my dream to be a physicist. Three of them deserve to be highlighted: my mother, Lucimara Helena Gallo Piva, who taught me how to walk, speak and read; my uncle, Rogerio Piva, who was my math teacher from when I started counting to the end of high school; and my supervisor, Alberto Vazquez Saa, who had the core idea of this research project, gave me the proper guidance through it and always helped me to get inspiration.

I am very grateful to my whole family for the support and my friends for all the good moments, jokes and laughs, discussions about math, physics, life, the universe and everything. Special thanks to Otavio Canton, Gabriel Ruffolo, Leonardo Leite and to Matheus Zambianco.

I also thank my brothers, Vitor Helio Piva and Lucas Velloso Blanco, and girlfriend, Julia Veiga Copertino Niro, for all love and care they have provided me during all the time I have known them.

Finally, I would like to thank UNICAMP for my entire undergraduate and master degree education, and FAPESP for supporting this research project with the grant #2018/23857-8, São Paulo Research Foundation (FAPESP).

Portuguese translation of the last paragraph:

Finalmente, eu gostaria de agradecer à UNICAMP por toda minha formação em nível de graduação e mestrado, e também à FAPESP por financiar este projeto de pesquisa com o processo nº 2018/23857-8, Fundação de Amparo à Pesquisa do Estado de São Paulo (FAPESP).

# Resumo

Neste trabalho estudamos as consequências da emissão de ondas gravitacionais a partir de uma fonte compacta sem rotação através do espaço-tempo de Robinson-Trautman. Primeiro entendemos como usar o momento de Bondi e o grupo BMS para extrair e controlar propriedades físicas da fonte. Após determinar explicitamente as expressões de energia e velocidade para a métrica de Robinson-Trautman, focamos no entendimento da evolução temporal e determinação de condições iniciais apropriadas para serem analisadas. Então, descobrimos como lidar com o caso da fase pós-mesclagem de uma colisão frontal de dois buracos negros em diferentes referenciais de Bondi, o que nos inspirou a propor uma nova condição inicial que representa a colisão frontal de um número qualquer de buracos negros. Ao fim, usamos os algoritmos desenvolvidos com um método de Galerkin para resolver a evolução temporal, possibilitando explorar a eficiência da emissão de ondas gravitacionais e velocidade de recuo de alguns dos sistemas propostos durante o texto. Uma relação qualitativa entre as propriedades físicas da fonte e as assimetrias do aspecto de massa de Bondi também foi explorado.

**Palavras-chave:** Ondas gravitacionais, Espaço-tempo de Robinson-trautman, Colisão frontal, Buraco negro, Condição inicial de Brill-Lindquist, Recuo gravitacional, Relatividade numérica, método de Galerkin.

# Abstract

In this work we study the consequences of gravitational wave emission from a compact source without rotation with aid of Robinson-Trautman spacetimes. First, we understand how to use Bondi momentum and the BMS group in order to extract and control physical properties of the source. After determining the explicit expressions of energy and velocity for Robinson-Trautman metric, we focus on understanding time evolution and determination of proper initial data to be analyzed. Then, we discover how to deal with the post merger phase of a frontal collision of two black holes in different Bondi reference frames, which inspired us to propose a new initial condition that represents the head-on collision of any number of black holes. At the end, we use the algorithms developed with a Galerkin method to solve time evolution, making possible to explore efficiency and kick velocity for some of the systems proposed during the text. A qualitative relation between physical properties of the source and the Bondi mass aspect asymmetries is also explored.

**Keywords:** Gravitational waves, Robinson-Trautman spacetimes, Head-on collision, Black hole, Brill-Lindquist initial data, Gravitational recoil, Numerical relativity, Galerkin method.

# List of Figures

Figure 1	– Two possibilities of foliation for a spacetime with a compact source represented by the black worldtube. In this figure one spatial dimension is suppressed and in (b) the past portion of each null surface is omitted for better visualization. . . . .	23
Figure 2	– Alice in the origin of the blue axis emitted the blue pulse and Bob in the origin of the black axis emitted the orange pulse. Here the red arrow represents $\delta r$ . . . . .	30
Figure 3	– Perspectives of the system for each observer. Bob sees the orange pulse and he is located at the origin of the black axis. Alice sees the blue pulse and she is located at the origin of the blue axis. Here the red vector represents Alice’s frame velocity. . . . .	31
Figure 4	– Two stages of a head-on binary collision of spherical black holes. Here red wave regions represent higher front wave densities compared to blue regions for each source. The velocity and acceleration of the center of mass frame are represented with blue and red arrows respectively. . . .	39
Figure 5	– Sketch of the Penrose diagram for a RT spacetime. Here $\mathcal{I}^+$ is the future null infinity (in blue), $\mathcal{H}^-$ is the past horizon (in orange), $i^+$ is the future timelike infinity (red dot), GWs are represented by green arrows and negative $r$ denotes an antipodal point on $(\theta, \phi)$ for the same $r$ value. . . . .	40
Figure 6	– Sketch of the Penrose diagram for a binary collision of BHs, each one generated by its own gravitational collapse. Here $\mathcal{I}^+$ and $\mathcal{I}^-$ are future and past null infinities (in blue), $\mathcal{H}^+$ is the future horizon (in orange), $i^+$ and $i^-$ are the future and past timelike infinities (red dots), $i^0$ is the spacelike infinity (black dots), GWs are represented by green arrows, the worldtubes of matter content are drawn in gray and negative $r$ denotes an antipodal point on $(\theta, \phi)$ for the same $r$ value. . . . .	41
Figure 7	– Penrose diagrams of Schwarzschild and a single spherical BH collapse. Here $\mathcal{I}^+$ and $\mathcal{I}^-$ are future and past null infinities (in blue), $\mathcal{H}^+$ and $\mathcal{H}^-$ are the future and past horizons (in orange), $i^+$ and $i^-$ are the future and past timelike infinities (red dots), $i^0$ is the spacelike infinity (black dots), the worldtube of matter content is drawn in gray and negative $r$ denotes an antipodal point on $(\theta, \phi)$ for the same $r$ value. . . . .	42
Figure 8	– Fraction of energy emitted $\Delta$ for each case of (4.9) with $\alpha_1 = \alpha_2$ . . . .	50
Figure 9	– Bondi mass aspect of a BL initial condition with $\alpha_1 = \alpha_2$ and velocities $w_1 = 0.7$ , $w_2 = 0.5$ . The velocity of the system before the stopping boost is represented by the red arrow. . . . .	50

Figure 10 – Bondi mass aspect of a BL initial condition with $\alpha_2/\alpha_1 = 0.5$ parameters and velocities $w_1 = w_2 = 0.7$ . The velocity of the system before the stopping boost is represented by the red arrow. . . . .	51
Figure 11 – Bondi mass aspect of a BL-2 initial condition with $\alpha_2/\alpha_1 = 1$ and blob velocities $w_1 = 0.7$ and $w_2 = 0.7$ . The center of mass velocity of the system is represented by the red arrow. The boost done was $0.25\hat{x}$ . . . . .	53
Figure 12 – Fraction of energy emitted $\Delta$ for each case of (4.12) with $\alpha_1 = \alpha_2$ , $w = w_1 = w_2$ and $\beta$ the angle between $\hat{n}_1$ and $-\hat{n}_2$ . . . . .	53
Figure 13 – Bondi mass aspect of a BL-3 initial condition with equal $\alpha_i$ parameters and final velocities $w'_1 = w'_2 = w'_3 = 0.7$ . The center of mass velocity in (a) is represented by the red arrow, with value of $-0.35\hat{y}$ . . . . .	54
Figure 14 – Values of $\Delta$ for some cases without recoil up to twenty blobs with all $w_i = 0.8$ and equal $\alpha_i$ parameters. The vectors $\hat{n}_i$ are disposed at the vertices of regular polygons or polyhedra. . . . .	55
Figure 15 – Bondi mass aspect of two BL-4 initial conditions with equal $\alpha_i$ parameters and blob velocities $w_1 = w_2 = w_3 = w_4 = 0.8$ . Black arrows represent the $\hat{n}_i$ vectors out of scale. In (a) the $\hat{n}_i$ vectors are disposed on the vertices of square, while in (b) they are aligned with the vertices of a tetrahedron. . . . .	55
Figure 16 – Bondi mass aspect of two BL- $n$ double pyramid initial conditions with $w_i = 0.8$ and equal $\alpha_i$ parameters. Black arrows represent the $\hat{n}_i$ vectors out of scale. The planes of reflection associated with these initial conditions are represented in orange. . . . .	56
Figure 17 – Values of $\Delta$ for all cases without recoil up to thirty blobs with all $w_i = 0.8$ and equal $\alpha_i$ parameters. The vectors $\hat{n}_i$ are disposed at the vertices of regular polygons or double pyramids. . . . .	56
Figure 18 – Bondi mass aspect of two BL- $n$ initial conditions with equal $\alpha_i$ parameters in the rest frame at $u_0$ . Black arrows represent the $\hat{n}_i$ vectors out of scale. In (a) we have $w_1 = 0.6$ and $w_2 = w_3 = 0.8$ , while in (b) $w_i = 0.8$ for all $i$ . The planes of reflection associated with these initial conditions are represented in orange. . . . .	57
Figure 19 – Modal coefficients of the $u$ evolution for (5.4) initial data with $q = 1$ , $w = 0.5$ . The axisymmetric algorithm with $N = 10$ was used with 2000 integration steps. . . . .	60
Figure 20 – Modal coefficients of the $u$ evolution for (5.4) initial data with $q = w = 0.5$ . The axisymmetric algorithm with $N = 10$ was used with 2000 integration steps. . . . .	61

Figure 21 – First modal coefficients of the $u$ evolution for (5.5) initial data with $q = 1, w = 0.5$ . The planesymmetric algorithm with $N = 7$ was used with 2000 integration steps. . . . .	62
Figure 22 – Bondi energy and momentum $u$ evolution for (5.4) initial data with $q = w = 0.5$ and 250 integration steps from $u_0 = 0$ until $u = 0.125/24m_0$ . The orange and green curves are the solutions of (5.6) for (5.4) in different Bondi frames of reference. The blue curves were built with direct calculation of Bondi momentum with the formula (2.8). . . . .	64
Figure 23 – Bondi energy and momentum $u$ evolution for stopped (5.4) initial data with $q = w = 0.5$ and 250 integration steps from $u_0 = 0$ until $u = 0.125/24m_0$ . The orange and green curves are the solutions of (5.6) for (5.4) in different Bondi frames of reference. The blue curves were built with direct calculation of Bondi momentum with the formula (2.8). . . . .	64
Figure 24 – Numerical calculations of $\Delta$ and $v_k$ for (5.4) initial data with $w = 0.5$ for 50 values of $q$ . The evolution was done with 2000 integration steps from $u_0 = 0$ until $u = (24m_0)^{-1}$ . . . . .	65
Figure 25 – Kick velocity values for results in Figure 24a boosted in the direction of the axis of symmetry (a) and in a perpendicular direction (b). . . . .	66
Figure 26 – Numerical calculations of $\Delta$ and $v_k$ for BL-3 equilateral triangle initial data with all $w_i = 0.5$ for 50 values of $q$ . The evolution was done with 2000 integration steps from $u_0 = 0$ until $u = (24m_0)^{-1}$ . . . . .	66
Figure 27 – Kick velocity values for results in Figure 26a boosted in the direction of the axis contained by the planes of symmetry (a) and in a normal direction (b). . . . .	67
Figure 28 – Numerical calculations of $\Delta$ and $v_k$ for BL-4 tetrahedron initial data with blob velocities $w_i = 0.5$ for 50 values of $q$ . The evolution was done with 2000 integration steps from $u_0 = 0$ until $u = (24m_0)^{-1}$ . . . . .	67
Figure 29 – Numerical calculations of $\Delta$ and $v_k$ for a BL-3 initial data with $w_1 = 0.5, w_2 = w_3 = 0.4$ and 50 values of $q$ . The evolution was done with 2000 integration steps from $u_0 = 0$ until $u = (24m_0)^{-1}$ . . . . .	68
Figure 30 – Numerical calculations of $\Delta$ and $v_k$ for a BL-3 equilateral triangle initial data with blob velocities $w_i = 0.5$ for 100 values of $q$ . The evolution was done with 2000 integration steps from $u_0 = 0$ until $u = (24m_0)^{-1}$ . . . . .	69
Figure 31 – Bondi mass aspect of two BL- $n$ pyramid cases with $w_i = 0.8$ and equal $\alpha_i$ parameters. Black arrows represent the $\hat{n}_i$ vectors out of scale and planes of reflection in (b) are represented in orange. . . . .	69
Figure 32 – Numerical calculations of $\Delta$ and $v_k$ for BL-5 pyramid initial data with blob velocities $w_i = 0.5$ for 50 values of $q$ . The evolution was done with 2000 integration steps from $u_0 = 0$ until $u = (24m_0)^{-1}$ . . . . .	70

Figure 33 – Numerical calculations of $\Delta$ and $v_k$ for BL- $n$ pyramid initial data with blob velocities $w_i = 0.8$ up to $n = 30$ . The evolution was done with 2000 integration steps from $u_0 = 0$ until $u = (24m_0)^{-1}$ . . . . .	71
Figure 34 – Perspectives of the rod for each observer. The picture illustrates the change in angle to each observer’s perspective. . . . .	80

# List of abbreviations and acronyms

RT	Robinson-Trautman
GW	Gravitational Wave
GR	General Relativity
GS	Goldberg-Sachs
BMS	Bondi-Metzner-Sachs
BH	Black Hole
BL	Brill-Lindquist
ADM	Arnowitt-Deser-Misner
ODE	Ordinary Differential Equation
PDE	Partial Differential Equation

# Contents

	<b>INTRODUCTION</b>	<b>15</b>
<b>1</b>	<b>GRAVITATIONAL WAVES AND COMPACT SOURCES</b>	<b>19</b>
1.1	Petrov's classification and Weyl scalars	19
1.2	Foliations and Goldberg-Sachs theorem	22
1.3	Mass definitions for black holes	25
1.4	The BMS group	29
<b>2</b>	<b>ROBINSON-TRAUTMAN SPACETIMES</b>	<b>33</b>
2.1	General properties	33
2.2	Time evolution	35
2.3	Physical systems	37
2.4	About the causal structure	39
<b>3</b>	<b>GALERKIN METHOD</b>	<b>43</b>
3.1	General case	43
3.2	Planesymmetric case	46
3.3	Axisymmetric case	46
<b>4</b>	<b>INITIAL CONDITIONS</b>	<b>48</b>
4.1	Axisymmetric binary collision	48
4.2	Non axisymmetric binary collision	52
4.3	Collisions involving more BHs	54
<b>5</b>	<b>NUMERICAL RESULTS</b>	<b>58</b>
5.1	Strategies and uncertainties	58
5.2	About Bondi momentum evolution	63
5.3	Kick velocity	65
5.4	BL- $n$ Pyramids	69
	<b>CONCLUSION</b>	<b>72</b>
	<b>BIBLIOGRAPHY</b>	<b>74</b>

<b>APPENDIX</b>	<b>79</b>
<b>APPENDIX A – ABERRATION OF LIGHT EFFECT . . . . .</b>	<b>80</b>
<b>APPENDIX B – SELECTION RULES FOR INTEGRATION OF THE MULTIPLICATION OF MANY SPHERICAL HAR- MONICS . . . . .</b>	<b>82</b>

# Introduction

Let us start presenting a brief historical revision on the study of gravitational waves (GWs), since the first attempts to understand their nature until the description of the emission process for compact sources, with focus on Robinson-Trautman (RT) spacetimes.

The interest in gravitational waves (GWs) started even before Einstein's general theory of relativity (GR), mainly by exploring the similarities between Coulomb's and Newton's inverse square law and an electromagnetic analogy. The initial ideas to describe the GW phenomena in this manner were introduced in 1893 by Heaviside [1], who dealt with the gravitational interaction in total analogy with the electromagnetic case. Later in 1905, Poincaré [2] proposed a more fundamental and simpler framework where GWs propagated at the speed of light and, moreover, were emitted by accelerating massive bodies. At the time, many physicists were skeptical about the existence of GWs due to intrinsic differences between electromagnetism and gravity - as, for instance, the absence of negative mass - and lack of experimental evidence. There were not even theoretical proposals of physical apparatuses to measure such a low intensity predicted phenomena.

During the first years of Einstein's GR, the difficulties in finding exact solutions and their physical interpretation were a huge barrier to understand the gravitational interaction, and so the progress on GW phenomena was rather slow. The earliest attempt of a GW solution was a first order approximation by Einstein [3], who introduced the linearized gravity approach as we have today [4], and claimed that three types of GW perturbations would exist in Minkowski spacetime, but just one of them was transversal<sup>1</sup>. In fact, the other two types could have any velocity of propagation depending on the choice of reference frame, *i. e.*, they were just a consequence of the coordinate system adopted in the calculations. Eddington, one of the most famous skeptical on GW, considered all perturbation modes as unphysical. His comment that "gravitational waves propagate at the speed of thought" [5] illustrates very well the mainstream position at the time. Another important result was the first exact solution of Einstein's equations containing GWs [6], a situation with cylindrical symmetry where GWs are emanating from an infinite source. Until the later fifties, the problem was far from being solved, since a crucial step was still lacking: the development of a criterion to identify precisely the GW contents of a given spacetime.

The elucidation of these questions started in 1957 with Pirani's work [7], in which he used the tetrad formalism to detect the presence of GWs as certain discontinuities

---

<sup>1</sup> The fact that GWs are transverse waves is well known today, but it definitely was not at the time.

of the Riemann tensor across specific three dimensional null hypersurfaces. Such definition excluded any kind of longitudinal coordinate dependence for GWs. These results also contributed to guide the physical interpretation of the Petrov classification of spacetimes in different types of gravitational content [8]. Also in the work [7], Pirani discussed the effect of GWs passing through a group of test particles via geodesic deviation equations, explaining the behavior of GWs in regions far from the source. This was the key theoretical tool to understand energy transport and development of measurement devices. In this context, Feynman so-called “Sticky bead argument” [9] was very important at the time to convince the remaining skeptical that GWs were indeed real. Later, a fundamental theorem connecting the Petrov classification and the behavior of families of light rays in spacetime (null congruences) was discovered by Goldberg and Sachs (GS) [10], which helped to understand the physical properties of different gravitational field types.

Another important question in the discussion was the possibility of the source “mass consumption” during radiation processes, since GWs do transport energy. The first attempt to answer such question arised with the discovery of exact plane waves by Bondi, Pirani and Robinson [11] in 1959, but these solutions could not describe properly any emission of massive compact bodies since they were built between two sheets in Minkowski spacetime. This configuration is rather unphysical and the authors argued that only a solution of a compact source of GWs would bring the discussion to an end. Within this context, the sixties papers about GWs played a huge role to build methods to understand the emission process and we will focus on their content now. For a deeper and longer historical description, including the two Nobel prizes on GWs indirect and direct detection, we recommend [9].

Inspired by the plane wave solutions, Robinson and Trautman published in 1960 a family of solutions with spherical GWs, which would be later called RT spacetimes [12]. It was not clear at the time if these solutions could represent an isolated compact source, because Schwarzschild metric was a special case of RT spacetimes, but the radiative cases seemed to have singularities in their wave fronts, which was pointed by the authors as possible ingoing mass flow in the system. Then, in the next year, Sachs formulated a condition for GW fields to be only outgoing [13], and any algebraically special metric would satisfy such condition. Since RT metric is algebraically special, it immediately become a promising candidate to describe a physically reasonable spacetime with GW content. Also in 1961, Newman and Penrose systematized and completed the ideas of the GS-Theorem based on the spinor affine connection [14], in such a way that all characteristics of null congruences were understood and the asymptotic behavior of asymptotically flat metrics was investigated with Weyl scalars<sup>2</sup>. RT spacetimes could also be derived and studied with this strategy [15].

---

<sup>2</sup> The specific name “Weyl scalars” was not used in this first approach.

In 1962, Robinson and Trautman presented a study about the details of vacuum field equations to their solution [16], with explicit examples of constants of motion and properties of the source and waves. In the same year, Bondi, van der Burg and Metzner established a metric based formalism using the null geodesics of spacetime [17, 18]. They defined the news function, which quantifies the GW flux at future null infinity, and used it to show that a compact source with outgoing GWs loses mass during the emission process. This result was really important, but the authors analyzed only axisymmetric systems, and Sachs extended it for general isolated compact sources in sequence [19]. Sachs also investigated a group of transformations which action remained the boundary conditions of the metric unchanged, the Bondi-Metzner-Sachs (BMS) group, that is a generalization of the Poincaré group and dictates asymptotic symmetries of asymptotically flat spacetimes. These new strategies were firstly applied to RT spacetimes by Foster and Newman in 1967 [20], finding cases for which the Schwarzschild metric was the stationary solution in the asymptotic future, but approximations were needed because of technical difficulties in solving field equations.

Solution existence and convergence of general initial conditions for RT field equations could only be well established at the beginning of the 90's [21, 22, 23]. In these works the authors showed the convergence of regular RT initial data to Schwarzschild solution for positive time evolution. Then, the interpretation of RT spacetimes as a perturbation of a spherical Black Hole (BH) was clarified. Even so, the equations were difficult to handle and the problem of full field evolution was solved only in 1999, when Prager and Lun proposed a spectral method to perform the task [24]. Since then, RT metrics have been studied with the aid of this numerical method. Recent works have presented the investigation of post-merger phase of binary collisions between Schwarzschild BHs using RT spacetimes, making possible to calculate precise values of energy loss and recoil due to GW emission with good precision [25, 26, 27, 28].

The main objective of this dissertation is to study the emission process of GWs for compact sources without angular momentum. In [chapter 1](#) some tools are presented in order to understand properties of asymptotically flat metrics, with focus on a derivation of the BMS group by a simple analysis of the future null infinite symmetries for Minkowski spacetime. In [chapter 2](#) we use these tools to compute physical properties of RT spacetimes, fixing all Bondi coordinates degrees of freedom. We also use a rotation and a Lorentz boost in order to prove which is the right definition of velocity for the source. In [chapter 3](#) the full spectral method to solve RT equations based on an expansion of ordinary spherical harmonics is developed, leading to a new strategy that is the most efficient one to solve RT equations for a generic initial condition, without any known symmetry. Then, we prove some properties of special cases, allowing us to classify axisymmetric and planesymmetric initial data.

---

After setting all strategies to perform time evolution and compute physical properties of RT spacetimes, we start to analyze specific examples. In [chapter 4](#) we study Brill-Lindquist (BL) initial conditions for the ordinary axisymmetric case and extend it to the non-axisymmetric case with a Lorentz boost. Then, we propose a generalization for this type of initial data, which represents the post-merger phase of a head-on (frontal) collision of any number of BHs. Also, we explore the connection between the inhomogeneities of Bondi mass aspect and efficiency of GW emission. At the end, in [chapter 5](#), we develop numerical algorithms to investigate recoil of the source, always with the aid of systems proposed in [chapter 4](#). With these results, the relation between Bondi mass aspect asymmetries and recoil direction is investigated. Throughout the entire text we will use geometric units ( $c = G = 1$ ) and the Einstein summation convention for repeated indices.

# 1 Gravitational Waves and Compact Sources

Gravitational Waves (GWs) are transversal waves that carry information about gravitational field changes and propagate at the speed of light, like photons, so they are intimately related with the causal structure of spacetime, reaching regions that other kinds of gravity ripples can not access. For this reason, their physical interpretation demands many theoretical tools besides Einstein's equations - as explained in the historical context given in the [introduction](#) -, so a full development of all needed techniques is a long journey. In this chapter, we will present the most important results about spacetimes containing GWs, with focus on vacuum compact sources, always assuming elementary knowledge about GR and differential geometry.

By compact sources we mean asymptotically flat spacetimes, the ones with a metric that approaches Minkowski for regions far enough from the origin. For us, this means that the metric can be written in usual spherical coordinates  $(t, r, \theta, \phi)$  and, for large  $r$  values, its expression reads

$$ds^2 = -dt^2 + dr^2 + (r^2 + \mathcal{O}(r)) d\Omega^2 + \mathcal{O}\left(\frac{1}{r}\right), \quad (1.1)$$

where  $d\Omega^2 = d\theta^2 + \sin^2\theta d\phi^2$  and the terms of  $\mathcal{O}(1/r)$  can be present in any component of the metric, not only in the diagonal. In this work all spacetimes considered will be asymptotically flat and the notation for coordinates introduced in (1.1) will be fixed.

## 1.1 Petrov's classification and Weyl scalars

Categorizing and understanding all kinds of gravitational content of a general spacetime can be a challenging task, and the Petrov classification [8] is the best way of doing it. To separate and study each one of them, the tetrad formalism may be introduced. Different from the coordinate basis - usually represented as  $\partial_\mu$  -, a tetrad is a general collection of four linearly independent local vector fields  $\hat{e}_\mu^A(x^\nu)$  used as basis for the tangent space, with capital Latin letters running from 0 to 3. The expression of the line element is given by

$$ds^2 = g_{\mu\nu} dx^\mu dx^\nu = \eta_{AB} \hat{e}^A \hat{e}^B \quad (1.2)$$

and a common choice of tetrad is an orthonormal one, which encodes all curvature information in the basis itself, and the expression of the metric reduces to the same as

Minkowski in Cartesian coordinate basis

$$\eta_{AB} = \begin{pmatrix} -1 & 0 & 0 & 0 \\ 0 & 1 & 0 & 0 \\ 0 & 0 & 1 & 0 \\ 0 & 0 & 0 & 1 \end{pmatrix}. \quad (1.3)$$

The Weyl tensor ( $C_{\mu\nu\alpha\beta}$ ) is the traceless part of Riemann tensor and it can be used to investigate gravitational content as well, since the only information loss by the lack of trace is about volume changes from tidal forces<sup>1</sup>. Its expression is

$$C_{\mu\nu\alpha\beta} = R_{\mu\nu\alpha\beta} - \frac{1}{2} (g_{\mu[\alpha} R_{\beta]\nu} - g_{\nu[\alpha} R_{\beta]\mu}) + \frac{1}{3} g_{\mu[\alpha} g_{\beta]\nu} R, \quad (1.4)$$

with  $R_{\mu\nu} = R^{\alpha}{}_{\mu\alpha\nu}$  and  $R = R^{\alpha}{}_{\alpha}$  being the Ricci's tensor and scalar. Also, the square brackets mean antisymmetrization of the involved indices. For compact sources, as states the Peeling Theorem, each Petrov type of gravitational field has a known asymptotic behavior that can be used to decompose the Weyl tensor, since it is written in a specific orthonormal tetrad, as:

$$C_{ABCD} = \frac{N_{ABCD}}{r} + \frac{III_{ABCD}}{r^2} + \frac{D_{ABCD}}{r^3} + \frac{II_{ABCD}}{r^3} + \frac{I_{ABCD}}{r^4} + \mathcal{O}\left(\frac{1}{r^5}\right). \quad (1.5)$$

Type  $N$  regions of spacetime indicate GW content; type  $III$  is associated with longitudinal waves with frame dependent velocity; type  $D$  is called Coulomb field, with tidal forces similar to the ones in Schwarzschild or Kerr solutions; type  $II$  is a general combination of the previous ones and type  $I$  can degenerate in types  $II$  or  $D$ . Regions where the Weyl tensor is null are called  $O$  type. Adding the vacuum condition ( $R_{\mu\nu} = 0$ ), we have  $R_{\mu\nu\alpha\beta} = C_{\mu\nu\alpha\beta}$  and the previous considerations are valid for the Riemann tensor as well. The procedure to find the tetrad that leads to (1.5) is out of the scope of this work and it is well explained in [29].

A more direct way to understand compact sources is by studying the Weyl scalars, what demands the use of a null orthonormal tetrad, which is possible only if we admit complex valued vector fields as elements for the basis. The easiest way to construct such basis is to start from a metric in spherical coordinates  $(t, r, \theta, \phi)$ , find an orthonormal tetrad  $\{\hat{e}_{\mu}^A\}$  and define:

$$\begin{aligned} k_{\mu} &= \frac{1}{\sqrt{2}} (\hat{e}_{\mu}^t + \hat{e}_{\mu}^r); \\ l_{\mu} &= \frac{1}{\sqrt{2}} (\hat{e}_{\mu}^t - \hat{e}_{\mu}^r); \\ m_{\mu} &= \frac{1}{\sqrt{2}} (\hat{e}_{\mu}^{\theta} + i\hat{e}_{\mu}^{\phi}). \end{aligned} \quad (1.6)$$

<sup>1</sup> The Weyl tensor is invariant under conformal transformations and it only differs from the Riemann tensor in the presence of matter, a case that we are not interested in this work.

The basis is given by  $\{k^\mu, l^\mu, m^\mu, \bar{m}^\mu\}$ , where  $k_\mu$  is an outgoing vector,  $l_\mu$  an ingoing one and the bar indicates complex conjugation. The metric expressed in this null tetrad reads

$$\eta_{AB} = \begin{pmatrix} 0 & -1 & 0 & 0 \\ -1 & 0 & 0 & 0 \\ 0 & 0 & 0 & 1 \\ 0 & 0 & 1 & 0 \end{pmatrix}. \quad (1.7)$$

Then, the Weyl scalars are calculated:

$$\begin{aligned} \Psi_0 &= C_{\mu\nu\alpha\beta} k^\mu m^\nu k^\alpha m^\beta; & \Psi_1 &= C_{\mu\nu\alpha\beta} k^\mu l^\nu k^\alpha m^\beta; & \Psi_2 &= C_{\mu\nu\alpha\beta} \bar{m}^\mu l^\nu k^\alpha m^\beta; \\ \Psi_3 &= C_{\mu\nu\alpha\beta} \bar{m}^\mu l^\nu k^\alpha l^\beta; & \Psi_4 &= C_{\mu\nu\alpha\beta} \bar{m}^\mu l^\nu \bar{m}^\alpha l^\beta. \end{aligned} \quad (1.8)$$

They are complex in general and, for compact sources, their asymptotic behavior is  $\Psi_n = \mathcal{O}(r^{n-5})$  [14]. Comparing the large  $r$  behaviour of (1.8) with (1.5), one can interpret  $\Psi_4$  as the  $N$  type contribution for regions far from the source. Actually, it is possible to write explicitly the lowest order approximation of  $\Psi_4$  as

$$\Psi_4^{(0)} = \frac{1}{r} \lim_{r \rightarrow \infty} r \Psi_4, \quad (1.9)$$

the outgoing GW content for large  $r$ . In the same way, asymptotic behavior of gravity can be analyzed from  $\Psi_1$  and  $\Psi_3$  for outgoing and ingoing longitudinal waves;  $\Psi_2$  for Coulomb type field; and  $\Psi_0$  for a combination of outgoing and ingoing modes of GW.

A useful feature of this approach is the ambiguity in the choice of basis, because there are transformations that maintain (1.6) as a null orthonormal tetrad, and one can have different Weyl scalars for each valid basis. The transformations of this kind that helps in our purpose are the null rotations around  $l^\mu$  or  $k^\mu$ , given by<sup>2</sup>

$$\begin{aligned} \tilde{l}^\mu &= l^\mu; \\ \tilde{m}^\mu &= m^\mu + a l^\mu; \\ \tilde{k}^\mu &= k^\mu + \bar{a} m^\mu + a \bar{m}^\mu + a \bar{a} l^\mu \end{aligned} \quad (1.10)$$

in the case of unchanged  $l^\mu$ . Here  $a$  is a complex parameter and the Weyl scalars transform as follows:

$$\begin{aligned} \tilde{\Psi}_0 &= \Psi_0 + 4a\Psi_1 + 6a^2\Psi_2 + 4a^3\Psi_3 + a^4\Psi_4; \\ \tilde{\Psi}_n &= \frac{1}{5-n} \frac{\partial \tilde{\Psi}_{n-1}}{\partial a}; \quad n = \{1, 2, 3, 4\}, \end{aligned} \quad (1.11)$$

To perform a null rotation around  $k^\mu$  the same procedure can be done, regarding that interchanging  $k^\mu$  and  $l^\mu$  leads to  $\Psi'_n = -\Psi_{4-n}$ .

The first expressions in (1.11) generates an algebraic equation  $\tilde{\Psi}_0 = 0$  that has solutions  $\{a_1, a_2, a_3, a_4\}$ , giving four specific new possibilities for  $\tilde{k}^\mu$  in general. Each one

<sup>2</sup> Again, see [29] for the full development.

of these  $\tilde{k}^\mu$  is called a principal null direction of spacetime. If all four roots are different, another null rotation around  $\tilde{k}^\mu$  can be done to make  $\Psi_4 = 0$  too, then only  $(\Psi_1, \Psi_2, \Psi_3)$  are not zero in this basis and, by the Peeling Theorem (1.5), spacetime is Petrov type *I*, the most general example for the asymptotically flat case.

Any case with at least one root repetition is called algebraically special and, when it happens, other Weyl scalars can be set to zero, making possible to determine into each other Petrov type the gravitational field degenerates to, just by knowing its large  $r$  behavior. The simplest occasion is when only one repetition occurs, so  $\tilde{\Psi}_1 = 0$  too in that direction, resulting in Petrov type *II* field. When there are two degenerated principal null directions, each null rotation (around  $l^\mu$  and  $\tilde{k}^\mu$ ) makes two scalars null, only  $\Psi_2$  survives and the field is type *D*. Another possibility is for a solution with multiplicity three, then only  $\Psi_3$  is not zero after the transformations and the field is type *III*. Only when all roots coincide, all the scalars except  $\Psi_4$  are turned into zero by the first transformation, so the null rotation around  $\tilde{k}^\mu$  does not change any Weyl scalar and the gravitational content is type *N*. These results are gathered in Table 1 that follows.

Table 1 – Weyl scalars that are always non zero for each Petrov type.

Petrov type	<i>I</i>	<i>II</i>	<i>D</i>	<i>III</i>	<i>N</i>
Weyl scalars	$\Psi_2, \Psi_3, \Psi_4$	$\Psi_2, \Psi_3$	$\Psi_2$	$\Psi_3$	$\Psi_4$

In short, compact sources of GWs can express all Petrov types, but each degenerated principal null direction restricts the possibilities for the gravitational field of the system. Then, algebraically special spacetimes are simpler and represent the greatest portion of known analytical solutions of Einstein's equations. Some examples of them are Schwarzschild and Kerr vacuums of type *D*, Kundt waves of type *III* and *N*, Bondi-Sachs vacuum spacetimes of type *II*.

## 1.2 Foliations and Goldberg-Sachs theorem

To have GW emission, at least second order time derivatives of the components of the metric must not be zero, then dynamical spacetimes are required to describe it, and only a boundary condition as (1.1) is not enough to have a well-posed problem to Einstein's equations. To handle this, one can try to slice spacetime in different hypersurfaces and write more boundary conditions with respect to some specific slices. A family of hypersurfaces chosen to represent these slices, whose union covers all spacetime, is called a foliation. The simplest way to find a foliation is with a non vanishing timelike vector field  $f^\mu(\lambda)$ , used to generate a family of three dimension normal hypersurfaces  $\Sigma_\lambda$ . These  $\Sigma_\lambda$  are spacelike and we call them a family of Cauchy surfaces if they intersect any timelike geodesic only once. If a foliation of Cauchy surfaces exists, we say that spacetime is globally hyperbolic and  $\lambda$

represents time at each  $\Sigma_\lambda$ . These Cauchy surfaces are the basis for the 3 + 1 formalism of GR [30].

If spacetime is globally hyperbolic, it is also possible to find two orthogonal null vector fields  $k^\mu$  and  $l^\mu$ , in the way that  $k^\mu k_\mu = l^\mu l_\mu = 0$  and  $k^\mu l_\mu = -1$ . These vectors span a family of null surfaces  $\mathcal{N}_{k,l}$  generating another type of foliation. The family of curves that have  $k^\mu$  or  $l^\mu$  as tangent vectors are called null congruences and the family of surfaces orthogonal to them are spacelike oriented surfaces  $S_{k,l}$ . If the congruences are geodesics<sup>3</sup>, they represent all possible photon trajectories orthogonal to  $S_{k,l}$ , so one can think of  $\mathcal{N}_{k,l}$  being guided by light rays shot by lasers, each one orthogonally attached to both sides of a specific spacelike surface of dimension two. GWs travel at the speed of light and they are transversal, so these 2 + 2 foliations are natural to understand them. Also, GWs only contribute with curvature change in  $S_{k,l}$ , *i. e.*, massive particle trajectories will be changed by a passing GW, but light rays will not. To picture the difference between the foliations, Figure 1 follows with an example of each of them for the case of a compact source with one spatial dimension suppressed. In 1a this suppression is systematized in each orange surface representing the Cauchy surfaces, different from 1b where the orange null surfaces have two dimensions indeed.

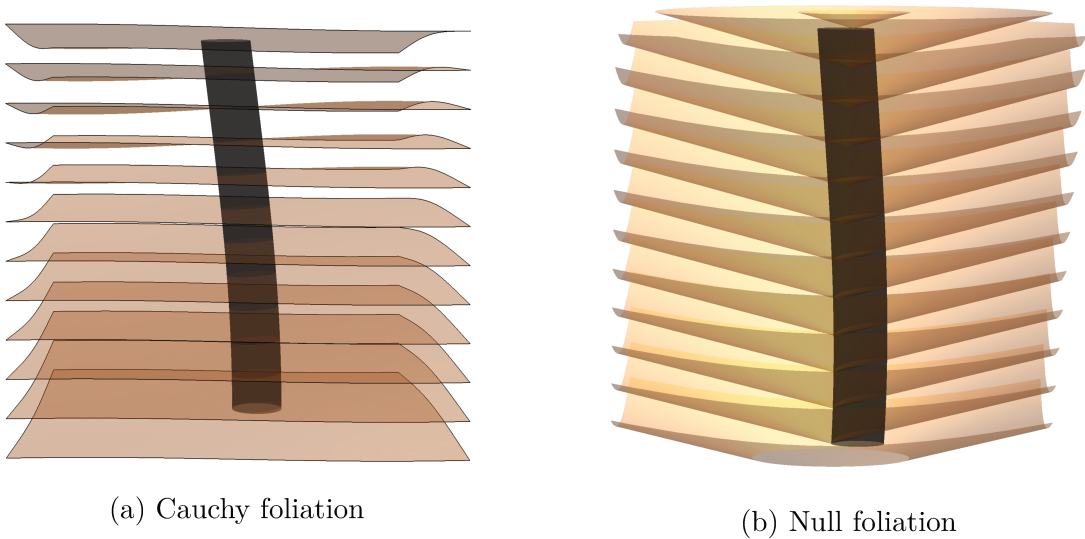


Figure 1 – Two possibilities of foliation for a spacetime with a compact source represented by the black worldtube. In this figure one spatial dimension is suppressed and in (b) the past portion of each null surface is omitted for better visualization.

Notation similarity with the last section is not coincidence, because it is always possible to find a dyad of complex null vectors  $m^\mu$  and  $\bar{m}^\mu$  tangent to all  $S_{k,l}$  surfaces and with  $m^\mu \bar{m}_\mu = 1$ . Then,  $\{k^\mu, l^\mu, m^\mu, \bar{m}^\mu\}$  is a null tetrad associated with the foliation given by  $\mathcal{N}_{k,l}$ . Also, the projector on  $S_{k,l}$  can be defined as

$$h^\mu{}_\nu = \bar{m}^\mu m_\nu + m^\mu \bar{m}_\nu \quad (1.12)$$

<sup>3</sup> The geodesic equations for  $k^\mu$  are given by  $k^\mu \nabla_\mu k^\nu = 0$ , where  $\nabla_\mu$  represents the covariant derivative.

and one can use the covariant derivative projected in this surface to understand local behavior of  $k^\mu$  (or  $l^\mu$  in the same way). Explicitly, we write

$$h^\alpha{}_\mu \nabla_\alpha k_\nu = \vartheta h_{\mu\nu} + \sigma_{\mu\nu} + \tau_{\mu\nu}, \quad (1.13)$$

with  $\vartheta$  being the trace of the decomposed tensor,  $\sigma$  its symmetric traceless part,  $\tau$  its antisymmetric part. The scalar  $\vartheta$  is called the expansion of the congruence and measures how much light rays are separating from each other;  $\sigma_{\mu\nu}$  is the shear tensor and  $\tau_{\mu\nu}$  is the twist tensor<sup>4</sup>, quantifying how much a two dimensional image on the spatial surface would be locally distorted and rotated respectively. It is also possible to write all this optical information with two complex scalars, according to spin coefficients formalism [14], in the following way:

$$\vartheta_{(k)} = -2\mathbf{Re}(\rho); \quad \sigma_{\mu\nu} = -\sigma \bar{m}_\mu \bar{m}_\nu - \bar{\sigma} m_\mu m_\nu; \quad \tau_{\mu\nu} = \mathbf{Im}(\rho)(m_\mu \bar{m}_\nu - \bar{m}_\mu m_\nu), \quad (1.14)$$

where  $\rho$  and  $\sigma$  are the complex divergence and shear respectively.

If we restrict ourselves to the case of closed  $S_{k,l}$ , we can fix  $k^\mu$  pointing outwards,  $l^\mu$  inwards and write the restriction (1.1) in the following way:

$$ds^2 = -du^2 - 2dudr + (r^2 + \mathcal{O}(r)) d\Omega^2 + \mathcal{O}\left(\frac{1}{r}\right), \quad (1.15)$$

where  $u$  is a retarded time coordinate, in the sense that  $u = t - r$  for large  $r$ . Here we also have  $k^\mu = \delta_r^\mu$  for large  $r$ .

To end this section we present the theorem proved by Goldberg and Sachs in 1962 [10], written in a different way in order to be more direct for our purposes:

**GS-Theorem.** *A vacuum metric,  $R_{\mu\nu} = 0$ , have null  $\Psi_0$  and  $\Psi_1$  Weyl scalars if and only if it has a shear-free,  $\sigma = 0$ , null geodesic congruence.*

This may look like a simple statement, but it gives a natural  $2 + 2$  foliation of spacetime, with spacelike surfaces normal to the tangent vector of the null congruence, say  $k^\mu$ , that is a degenerated principal null direction of spacetime. In other words, we must have  $\Psi_0 = \Psi_1 = 0$  in the null tetrad induced by this foliation. This means that Petrov types *II*, *III* and *N* must have one  $\sigma = 0$  null geodesic congruence and type *D* fields always present two of them<sup>5</sup>. Then, it is possible to determine the Petrov type of the field only by its Weyl scalars computed in this special basis, except when  $\Psi_2$  and  $\Psi_3$  are not zero together, because it is not possible to distinguish if the gravitational content is type *D* and *III* together, or just type *II*<sup>6</sup>.

<sup>4</sup> Also called vorticity.

<sup>5</sup> This is so powerful that made possible to find all type *D* vacuum solutions, see [31].

<sup>6</sup> See Table 1.

After all these considerations, we will follow now studying only Petrov type *II* cases (or their degenerated cases), always having in mind their potential to describe isolated massive bodies radiating GWs, since they can degenerate in Petrov types *III*, *D* and *N*, but always with  $\Psi_0 = 0$ , *i. e.*, no ingoing GWs.

### 1.3 Mass definitions for black holes

Even in vacuum solutions of Einstein's equations there can still be gravitational field, the case of black holes (BHs). They are spacetimes with curvature divergence singularities and represent very dense massive objects, so dense that gravity is too strong nearby them and even photons can not move away from their close surroundings. This inspires the definition of an event horizon, the boundary of a region where information will never be able to reach an external observer (photons can not get out of it). Also, BHs are important cases of GW sources and a definition for mass, energy and momentum associated with these objects is needed. In this section we will introduce two different mass concepts for BHs with compact event horizons.

The first concept is the Arnowitt-Deser-Misner (ADM) mass [30] and its definition is based on a foliation of Cauchy surfaces  $\Sigma_\lambda$ , introduced in section 1.2. ADM mass is a measurement of the asymptotic behavior of gravity and it is given by the medium extrinsic curvature of a two dimensional closed slice of each  $\Sigma_\lambda$ , in a region infinitely far from the event horizons of any BH. To elucidate how this is done, we will evaluate ADM 4-momentum for Schwarzschild metric in usual spherical coordinates as a toy example, like done in [32]. The metric reads

$$ds^2 = - \left(1 - \frac{2M}{r}\right) dt^2 + \left(1 - \frac{2M}{r}\right)^{-1} dr^2 + r^2 d\Omega^2 \quad (1.16)$$

and, since  $\partial_t$  is timelike,  $\Sigma_t$  can be used as Cauchy surface. Also, we just need to compute how constant  $r$  surfaces vary for a distant observer, since spacetime is spherically symmetric. The only possible variation in those surfaces is the area, so we expand its variation with respect to proper radial distance for large  $r$ . The result is

$$\frac{dA(r)}{ds} = \frac{dA(r)}{dr} \frac{dr}{ds} = 8\pi r \sqrt{1 - \frac{2M}{r}} = 8\pi r - 8\pi M + \mathcal{O}\left(\frac{1}{r}\right). \quad (1.17)$$

The first term of the expansion will always be the flat space standard variation. The lowest order contribution of spacetime curvature comes from the second term, so we define ADM mass aspect ( $M_{ADM}$ ) as [30]

$$\frac{dA(t, r, \theta, \phi)}{ds} = 8\pi r - 8\pi M_{ADM}(t, \theta, \phi) + \mathcal{O}\left(\frac{1}{r}\right), \quad (1.18)$$

which can be interpreted as the energy measured by an observer near spatial infinite. Then we can define ADM 4-momentum in this frame as

$$P_{ADM}^\mu(t) = \frac{1}{4\pi} \int_0^{2\pi} \int_0^\pi M_{ADM}(t, \theta, \phi) j^\mu \sin \theta d\theta d\phi, \quad (1.19)$$

with  $j^\mu = (1, \hat{\mathbf{r}}) = (1, \sin \theta \cos \phi, \sin \theta \sin \phi, \cos \theta)$ . This quantity can be thought as some kind of momentum of the center of mass frame, in the sense that it transforms as an authentic 4-vector by action of translations, rotations and Lorentz boosts<sup>7</sup> on the asymptotic spatial frame  $(t, \mathbf{r})$ . For the case of Schwarzschild, we have  $P_{ADM}^\mu = (M, 0, 0, 0)$  with no time dependence or spatial part of momentum, as expected for a spherical black hole at rest.

The only problem with ADM formalism is that it does not distinguish which contributions come from GWs or from Coulomb type fields of their sources. This separation can be a useful information to understand important properties of the system, as GW recoil for example. To get this separation we use Bondi-Sachs formalism [33], which can be seen as the same procedure, but changing the 3 + 1 foliation by a 2 + 2 one, in the sense that the Bondi mass aspect will define the same physical entities as ADM, but only for energy contributions that comes from the source.

The first step is to introduce the Bondi-Sachs metric in Bondi spherical coordinates

$$G_{\mu\nu} dX^\mu dX^\nu = -\frac{V}{R} e^{2\beta} dU^2 - 2e^{2\beta} dU dR + R^2 q_{ab} (dX^a - H^a dU)(dX^b - H^b dU), \quad (1.20)$$

where small Latin indices run through the usual angular coordinates ( $\Theta$  and  $\Phi$ ),  $U$  is a retarded time,  $R$  is the radius and the parameters are functions of all coordinates in general. To have an asymptotically flat spacetime in the sense of (1.15), the following boundary conditions for  $R \rightarrow \infty$  must be fulfilled:

$$\beta \rightarrow 0; \quad H^a \rightarrow 0; \quad \frac{V}{R} \rightarrow \zeta(U, \Theta, \Phi); \quad q_{ab} \rightarrow f_{ab}, \quad f_{ab} dX^a dX^b = d\Theta^2 + \sin^2 \Theta d\Phi^2, \quad (1.21)$$

with positive definite  $q_{ab}$ . The null vector  $\partial_R$  generates a shear-free geodesic congruence, then this spacetime is Petrov type *II* by the GS-theorem and it can represent a compact source surrounded by GWs. Also, constant  $U$  surfaces are spacelike and they are used to generate the natural 2 + 2 foliation.

As in ADM mass case, one can define the Bondi mass aspect ( $M_B$ ), given by

$$V = \zeta(U, \Theta, \Phi) R - 2M_B(U, \Theta, \Phi) + \mathcal{O}\left(\frac{1}{R}\right) \quad (1.22)$$

and Bondi 4-momentum is

$$P^\mu(U) = \frac{1}{4\pi} \int_0^{2\pi} \int_0^\pi M_B(U, \Theta, \Phi) j^\mu \sin \Theta d\Theta d\Phi, \quad (1.23)$$

<sup>7</sup> The Poincaré group.

but now  $j^\mu$  components are written with respect to an asymptotic null asymptotic Bondi frame  $(U, \mathbf{R})$ .

Although the null surfaces do not tell us anything about GWs, we still have the spacelike constant  $U$  surfaces to evaluate their effects. Then we look at the following auxiliary tensor  $c_{ab}$ :

$$q_{ab} = f_{ab} + \frac{1}{R}c_{ab}(U, \Theta, \Phi) + \mathcal{O}\left(\frac{1}{R^2}\right), \quad (1.24)$$

which measures the constant  $U$  surface deviation from the sphere in the lowest order<sup>8</sup>. In fact, this tensor is the first order deviation of  $q_{ab}R$  from the metric of the sphere

$$c_{ab} = \lim_{R \rightarrow \infty} R(q_{ab} - f_{ab}) = \lim_{R \rightarrow \infty} \frac{(q_{ab} - f_{ab})}{1/R}. \quad (1.25)$$

Since constant  $U$  surfaces are approximated by spheres for large  $R$ , we define the complex dyad  $\{m^a, \bar{m}^a\}$  as

$$m^a = \frac{1}{\sqrt{2}} \left( \delta^a_\Theta + \frac{i}{\sin \Theta} \delta^a_\Phi \right), \quad (1.26)$$

and use (1.14) to compute the gravitational shear scalar near null infinite<sup>9</sup>, given by

$$\sigma_{(0)} = -m^a m^b c_{ab}. \quad (1.27)$$

Any change in this quantity can only come from GW contributions, then we get to the famous news function  $N = \partial_U \sigma_{(0)}$ . There is GW presence in the system if and only if the news is not zero. Vacuum Einstein's equations determines mass aspect time variation

$$\frac{\partial M_B}{\partial U} = -\|N\|^2 + \partial_U W(U, \Theta, \Phi), \quad (1.28)$$

where  $W$  is a large expression that we are not interested in. The integration of (1.28) on  $S^2$  leads to the Bondi conservation law<sup>10</sup>

$$\frac{dP^\mu}{dU} = -\frac{1}{4\pi} \oint_{S^2} \|N\|^2 j^\mu dS. \quad (1.29)$$

To simplify (1.29), we use  $R\Psi_4^{(0)} = -\partial_U \bar{N}$  from [35] and, since we compute Weyl scalars with the tetrad generated by the outgoing null vector  $\partial_R$ , (1.29) becomes

$$\frac{dP^\mu}{dU} = -\frac{R^2}{4\pi} \int_0^{2\pi} \int_0^\pi \left\| \int_{U_0}^U \Psi_4^{(0)}(U', \Theta, \Phi) dU' \right\|^2 j^\mu \sin \Theta d\Theta d\Phi. \quad (1.30)$$

Then, we conclude that an isolated compact source of gravitational waves (Petrov type  $II$  field) loses mass in the emission process, because it is always taken a positive amount of

<sup>8</sup> This is true because  $H^a$  is at least  $\mathcal{O}(r^{-3})$  due to condition (1.15).

<sup>9</sup> The general gravitational shear as defined in (1.14) is zero, but its lowest order approximation for large  $R$  might not be null.

<sup>10</sup> Indeed, all contributions from  $W$  vanish after the integration. See [34] for full calculations.

energy of the source during  $U$  evolution. We can also solve (1.30) and get to

$$P^\mu(U) = P^\mu(U_0) - \frac{R^2}{4\pi} \int_{U_0}^U \int_0^{2\pi} \int_0^\pi \left\| \int_{U_0}^{U'} \Psi_4^{(0)}(U'', \Theta, \Phi) dU'' \right\|^2 j^\mu \sin \Theta d\Theta d\Phi dU'. \quad (1.31)$$

The simplest non trivial example of a known Bondi frame is the Eddington-Finkelstein outgoing coordinates for Schwarzschild spacetime

$$ds^2 = - \left( 1 - \frac{2M}{r} \right) du^2 - 2dudr + r^2 d\Omega^2. \quad (1.32)$$

Also  $M_B$  coincides with  $M_{ADM}$  in this case, because (1.32) is static and the news function is null, *i. e.*, an inertial spherical BH does not emit GWs.

To use this formalism with a vacuum metric  $g_{\mu\nu}(u, r, \theta, \phi)$  that is not directly expressed as (1.20), one can try to find a coordinate change that leads  $g_{\mu\nu}$  into the form of (1.20). The most general transformation from spherical coordinates  $\{u, r, \theta, \phi\}$  to a Bondi frame that keeps physical interpretations unchanged in momentum calculation is

$$\begin{aligned} U &= U_0 + \frac{U_1}{r} + \frac{U_2}{r^2} + \mathcal{O}\left(\frac{1}{r^3}\right); \\ R &= \frac{r}{R_{-1}} + R_0 + \frac{R_1}{r} + \mathcal{O}\left(\frac{1}{r^2}\right); \\ \Theta &= T_0 + \frac{T_1}{r} + \frac{T_2}{r^2} + \mathcal{O}\left(\frac{1}{r^3}\right); \\ \Phi &= F_0 + \frac{F_1}{r} + \frac{F_2}{r^2} + \mathcal{O}\left(\frac{1}{r^3}\right), \end{aligned} \quad (1.33)$$

where all coefficients are functions of  $(u, \theta, \phi)$ . Also, the transformed metric must fulfill the conditions

$$\begin{aligned} G^{UU} = G^{U\Theta} = G^{U\Phi} = 0; \quad G^{\Theta\Theta} G^{\Phi\Phi} - \left(G^{\Theta\Phi}\right)^2 &= (R^2 \sin \Theta)^{-2}; \\ G^{UR} = 1 + \mathcal{O}(R^{-2}); \quad G^{RR} = -\zeta + \frac{M_B}{R} + \mathcal{O}(R^{-2}); \quad G^{R\Theta} = \mathcal{O}(R^{-2}) &= G^{R\Phi}. \end{aligned} \quad (1.34)$$

The only problem is to get the right expression for Bondi momentum conservation law in the original reference frame. It is possible to determine (1.30) in  $(u, r, \theta, \phi)$  coordinates, but the final expression is not so easy to handle. It is given by

$$\frac{dP^\mu}{du} = -\frac{r^2}{4\pi} \oint_{S^2} \left( \frac{\partial U}{\partial u} \right) \left\| \int_{u_0}^u \Psi_4^{(0)}(u', \theta, \phi) du' \right\|^2 j^\mu dS + \frac{1}{4\pi} \oint_{S^2} M_B(u, \theta, \phi) \frac{\partial j^\mu}{\partial u} dS. \quad (1.35)$$

The second term in (1.35) is connected with the fact that  $j^\mu$  is related to one specific Bondi observer and, as the metric changes with GW emission, the notion of asymptotic Bondi frame also changes in time<sup>11</sup>.

<sup>11</sup> In [36] the time dependence of this null vector is determined for the case of Vaidya solution.

## 1.4 The BMS group

Compact sources must behave like flat spacetime when we observe events too far from a fixed point. However, we need to understand how Minkowski itself looks like far from its own origin to comprehend what it means in fact. In this section we will analyze the set of future null infinite events ( $\mathcal{I}^+$ ) of Minkowski, but in the perspective of different observers, and then conclude how must be the symmetries of  $\mathcal{I}^+$  for generic asymptotically flat spacetimes.

Let us start with Minkowski in coordinates  $(u, r, \theta, \phi)$ <sup>12</sup> defined in [section 1.2](#). Then we perform the most general coordinate change that keeps the metric in the form of [\(1.15\)](#), given by [\(1.33\)](#) from the last section. Using the metric components transformations

$$G^{\mu\nu} = \frac{\partial X^\mu}{\partial x^\alpha} \frac{\partial X^\nu}{\partial x^\beta} g^{\alpha\beta}, \quad (1.36)$$

we get

$$\begin{aligned} G^{RR} &= 2r \frac{R_{-1,u}}{(R_{-1})^3} + \mathcal{O}(r^0); \\ G^{UR} &= \frac{\partial_u U_0}{R_{-1}} + \mathcal{O}\left(\frac{1}{r}\right); \\ G^{U\Theta} &= \frac{\partial_u T_0}{R_{-1}} + \mathcal{O}\left(\frac{1}{r}\right); \\ G^{U\Phi} &= \frac{\partial_u F_0}{R_{-1}} + \mathcal{O}\left(\frac{1}{r}\right). \end{aligned} \quad (1.37)$$

With restrictions [\(1.34\)](#), the only possibility is that the leading order coefficients can not depend on  $u$ , resulting in

$$\begin{aligned} R_{-1} &= R_{-1}(\theta, \phi); \\ U_0 &= R_{-1}(\theta, \phi)u + \alpha(\theta, \phi); \\ \Theta_0 &= \Theta_0(\theta, \phi); \\ \Phi_0 &= \Phi_0(\theta, \phi), \end{aligned} \quad (1.38)$$

where  $\alpha$  is an arbitrary function on the sphere. With this approach, we can understand which part of the general transformation really affects the behavior of events infinitely far from the origin. The limit  $r \rightarrow \infty$  leads to

$$\begin{aligned} U &= R_{-1}(\theta, \phi)u + \alpha(\theta, \phi); \\ R &= \frac{r}{R_{-1}(\theta, \phi)}; \\ \Theta &= \Theta_0(\theta, \phi); \\ \Phi &= \Phi_0(\theta, \phi). \end{aligned} \quad (1.39)$$

<sup>12</sup> These coordinates were chosen because the foliation generated by them is  $2+2$ , so large  $r$  is near  $\mathcal{I}^+$ .

Because GR is frame independent, we know  $\mathcal{I}^+$  must remain the same after a coordinate change, what indicates that (1.39) is the action of a symmetry group of  $\mathcal{I}^+$ . This group is called Bondi-Metzner-Sachs (BMS) group, composed by rotations, Lorentz boosts and the supertranslations, a generalization of ordinary translations given by

$$U = u + \alpha(\theta, \phi). \quad (1.40)$$

Time translations are easily recognized by the case of constant  $\alpha$ , but BMS group has infinite dimension and the interpretation of all  $\alpha$  possibilities is not simple. The idea is that all observers in any specific direction  $(\theta, \phi)$  at  $\mathcal{I}^+$  are very far from each other, they do not have any causal connection and one can think of (1.40) as a change in calibration of all their clocks. To give more intuition about it, we will find which of the  $\alpha$  cases represent spatial translations with help of Alice, Bob and a great amount of Charlies<sup>13</sup>. Suppose all of them are in flat space, Alice is at the origin, Bob is at  $\delta\mathbf{r}$  and all Charlies are infinitely far from them, one for each  $(\theta, \phi)$ . Then, both Alice and Bob emit a spherical pulse of light at the same time. To Alice, all Charlies will measure her pulse at  $u_\infty$  and Bob's pulse at  $u_\infty - \delta\mathbf{r} \cdot \hat{\mathbf{r}}$ . Bob disagrees and says that they will receive his own pulse at  $u_\infty$ , but Alice's pulse will get to them at  $u_\infty + \delta\mathbf{r} \cdot \hat{\mathbf{r}}$ . All the situation is pictured in Figure 2 below. At the end, the reader should be very glad that all Charlies are too far away, so

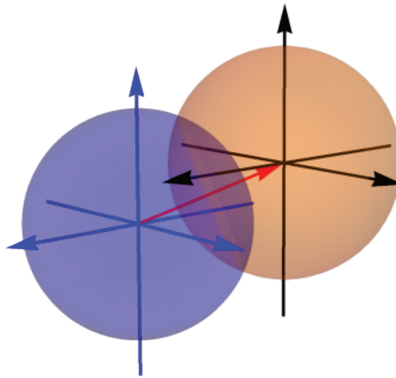


Figure 2 – Alice in the origin of the blue axis emitted the blue pulse and Bob in the origin of the black axis emitted the orange pulse. Here the red arrow represents  $\delta\mathbf{r}$ .

they will never tell Alice and Bob at which time they measured each pulse, and we can agree with both Alice and Bob despite of a new calibration of each Charlies' clock, which can be interpreted in two ways. The passive view states that Alice can move the origin of her reference frame by  $\delta\mathbf{r}$ , resulting in  $U = u + \delta\mathbf{r} \cdot \hat{\mathbf{r}}$ , but the same expression works for the active view, in the sense that all spacetime is rigidly translated by  $-\delta\mathbf{r}$ . Both interpretations are very similar and they always differ from each other by a change of sign.

About the Lorentz group, rotations are the usual unitary transformations over  $\mathbf{r}$  and the bigger problem lies on understanding the boosts. Then, we will count with the

<sup>13</sup> For the formal development of the following example with Penrose diagrams, see [37].

help of the same people used to comprehend translations in order to perform boosts. The procedure is to put Bob at the origin and Alice running with velocity  $v$  in the direction of  $\hat{\mathbf{n}}$ , over a straight line that passes through Bob. At the moment Alice reaches the origin, Bob emits a spherical pulse. Bob knows that every Charlie will receive his pulse at  $u_\infty$ , but he could swear Alice thinks they will see the pulse at  $u = u_\infty \gamma(1 + v\hat{\mathbf{n}} \cdot \hat{\mathbf{r}})$ . He is so confused about the situation that he also claims Alice would not even agree with which specific photon will be measured by each Charlie. “This can only be a light aberration”, he guesses. The same thoughts with changed sign for  $v$  are also disturbing Alice. Even so, for our luck, they are too stubborn and will never abandon their inertial frame to lose the discussion, so there will not be any argument<sup>14</sup>. Saying goodbye to our helpers we can write the boost of  $v\hat{\mathbf{n}}$  for all spacetime as

$$\begin{aligned} U &= u\gamma(1 - v\hat{\mathbf{n}} \cdot \hat{\mathbf{r}}); \\ R &= \frac{r}{\gamma(1 - v\hat{\mathbf{n}} \cdot \hat{\mathbf{r}})}; \\ \hat{\mathbf{R}} &= \frac{(\hat{\mathbf{n}} \cdot \hat{\mathbf{r}}) - v}{(1 - v\hat{\mathbf{n}} \cdot \hat{\mathbf{r}})}\hat{\mathbf{n}} + \frac{\hat{\mathbf{r}} - (\hat{\mathbf{n}} \cdot \hat{\mathbf{r}})\hat{\mathbf{n}}}{\gamma(1 - v\hat{\mathbf{n}} \cdot \hat{\mathbf{r}})}, \end{aligned} \quad (1.41)$$

where time and angle changes were derived in [Appendix A](#). The  $R$  expression comes from (1.39), since we need the final coordinates to represent a proper Bondi reference frame. It is important to be clear that (1.41) is the active view of Bob’s new calibration for Charlie’s clocks, *i. e.*, spacetime is being boosted to Alice’s velocity, so the minus sign in  $v$  needs to appear. To help with the visualization of the entire situation, [Figure 3](#) follows below.

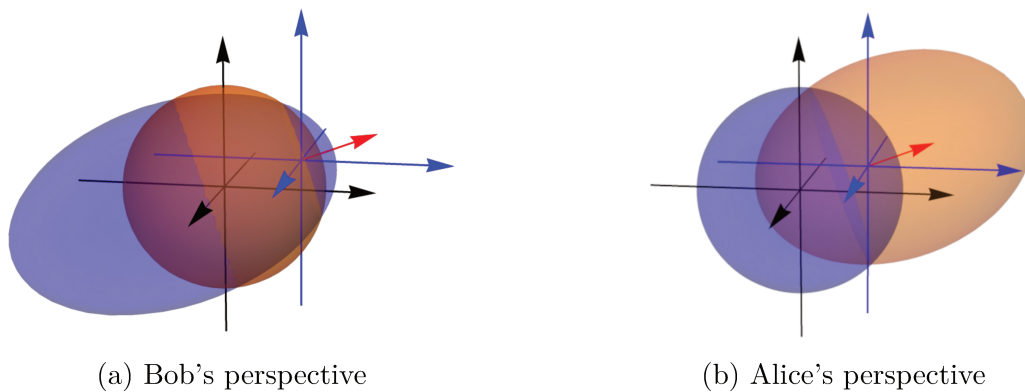


Figure 3 – Perspectives of the system for each observer. Bob sees the orange pulse and he is located at the origin of the black axis. Alice sees the blue pulse and she is located at the origin of the blue axis. Here the red vector represents Alice’s frame velocity.

As an example, we can perform a Lorentz boost in Schwarzschild spacetime. The procedure is to transform the angular part of the metric with the last expression in

<sup>14</sup> All physical results used in this derivation came directly from the twin paradox and aberration of light. See [Appendix A](#) for the time arrival formula for the pulse and [38] for the explanation of the disagreements between Alice and Bob.

(1.41) and calculate the respective Bondi mass aspect.

$$\begin{aligned}
 ds^2 &= - \left( 1 - \frac{2M}{r} \right) du^2 - 2dudr + \frac{r^2 d\Omega^2}{\gamma^2 (1 - v\hat{\mathbf{n}} \cdot \hat{\mathbf{r}})^2}; \\
 M_B &= \frac{M}{\gamma^3 (1 - v\hat{\mathbf{n}} \cdot \hat{\mathbf{r}})^3},
 \end{aligned}
 \tag{1.42}$$

Regarding the corrections of  $(u, r)$  to maintain the metric in Bondi coordinates (1.34), we get the expected momentum for a boosted spherical BH,  $P^\mu = \gamma M(1, v\hat{\mathbf{n}})$ .

As said in the beginning of this section, any region of an asymptotically flat spacetime that is sufficiently far from a fixed point must look like Minkowski. Now we know it means that  $\mathcal{I}^+$  must remain unchanged by the action of the BMS group. In this work we will only use simpler cases of this action, the ones connected to Poincaré group and always written in specific frames of reference. If the reader is interested in studying the BMS group and asymptotic flat spacetimes in a coordinate independent context, we recommend [39], that is a good and modern approach of the subject with interesting discussions about superrotations, which represent a natural extension of the Lorentz group in this scenario.

## 2 Robinson-Trautman Spacetimes

In this chapter we investigate the gravitational field content of Robinson-Trautman (RT) spacetimes, with the aid of the Goldberg-Sachs Theorem and Weyl scalars. Then, we also use Bondi-Sachs formalism to understand properties of the source of GWs. A solid definition of the source's instantaneous velocity is presented, in contrast with recent attempts with different approaches. The evolution equation is introduced, its stationary solution is given and the physical interpretation of the initial value problem is discussed.

### 2.1 General properties

RT spacetimes are the simplest vacuum solution of Einstein's equations that can represent compact sources surrounded by GWs. The standard form of the metric [25] is

$$ds^2 = g_{\mu\nu} dx^\mu dx^\nu = - \left( K(u, \theta, \phi) - \frac{2m_0}{r} - r \partial_u (\ln Q^2) \right) du^2 - 2du dr + \frac{r^2 d\Omega^2}{Q^2(u, \theta, \phi)}, \quad (2.1)$$

where  $m_0$  is a constant,  $Q$  and  $K$  are smooth functions,  $d\Omega^2$  is the unit sphere ( $S^2$ ) metric in the usual spherical coordinates angles  $(\theta, \phi)$ ,  $r$  is a radial distance and  $u$  is a retarded time.

Besides that,  $\partial_r$  generates a shear-free null geodesic congruence, with  $r$  as affine parameter, *i. e.*, (2.1) is algebraically special and the natural  $2 + 2$  foliation associated with it is based on constant  $u$  surfaces with Gaussian curvature given by  $\frac{K}{r^2}$ . The full expression for  $K(u, \theta, \phi)$  is

$$K = Q^2 \left( 1 + \frac{1}{2} \nabla_\Omega^2 (\ln Q^2) \right) = Q^2 + Q \nabla_\Omega^2 Q - (\nabla_\Omega Q)^2, \quad (2.2)$$

where  $\nabla_\Omega$  is the gradient operator on  $S^2$ . The null tetrad induced by the foliation reads

$$\begin{aligned} k^\mu &= \delta_r^\mu; \\ l^\mu &= \delta_u^\mu + \frac{g_{uu}}{2} \delta_r^\mu; \\ m^\mu &= \frac{Q}{\sqrt{2}r} \left( \delta_\theta^\mu + \frac{i}{\sin \theta} \delta_\phi^\mu \right). \end{aligned} \quad (2.3)$$

Computing the Riemann tensor in this basis we have

$$R_{ABCD} = \frac{N_{ABCD}}{r} + \frac{III_{ABCD}}{r^2} + \frac{D_{ABCD}}{r^3}, \quad (2.4)$$

with  $N$ ,  $III$  and  $D$  covariantly constant along  $\partial_r$ . This makes clear the interpretation of a compact body surrounded by GWs. Then, one can compute the Weyl scalars with (2.3)

like defined in (1.8):

$$\begin{aligned}
\Psi_0 &= \Psi_1 = 0; \\
\Psi_2 &= -\frac{m_0}{r^3}; \\
\Psi_3 &= -\frac{Q}{\sqrt{8}r^2} \mathcal{D}K; \\
\Psi_4 &= -\frac{\sin \theta}{4r^2} \mathcal{D} \left( \frac{Q^2 \mathcal{D}g_{uu}}{\sin \theta} \right),
\end{aligned} \tag{2.5}$$

where  $\mathcal{D} = \partial_\theta - \frac{i}{\sin \theta} \partial_\phi$ . As we already expected,  $\Psi_0 = \Psi_1 = 0$  and there are no ingoing GWs, then all GW content in spacetime was emitted by the compact source, which also generates the Coulomb type field represented by  $\Psi_2$ . The only case without GWs ( $\Psi_4 = 0$ ) occurs when  $K$  is constant, *i. e.*,  $\Psi_3 = \Psi_4 = 0$  and it is possible to recognize the Weyl scalars for Schwarzschild solution with mass  $m_0$ .

Using (1.33) and (1.34), we determine the transformation to Bondi coordinates as

$$\begin{aligned}
U &= \int_{u_0}^u Q(u', \theta, \phi) du' + \alpha(\theta, \phi) + \mathcal{O}\left(\frac{1}{r}\right); \\
R &= \frac{r}{Q(u, \theta, \phi)} + \mathcal{O}(r^0); \\
(\Theta, \Phi) &= (\theta, \phi) + \mathcal{O}\left(\frac{1}{r}\right),
\end{aligned} \tag{2.6}$$

where the leading order for angular coordinates was chosen to match the Lorentz frame of the original coordinates with the Bondi frame. However, there is still a huge gauge freedom to fix, since it is always possible to perform a supertranslation, parameterized by  $\alpha$ , which will determine all the higher order terms in (2.6). Then, we have

$$M_B(u, \theta, \phi) = \frac{m_0}{Q^3(u, \theta, \phi)} + \mathcal{P}(\partial_a U_0, \partial_a \partial_b U_0; u, \theta, \phi) \tag{2.7}$$

where  $\mathcal{P}$  is a homogeneous polynomial in  $x^a = (\theta, \phi)$  derivatives of  $U_0 = \int_{u_0}^u Q(u', \theta, \phi) du' + \alpha(\theta, \phi)$ . To determine  $\mathcal{P}$  at a generic instant of time  $u$  is a hard task<sup>1</sup>, so we choose  $\alpha(\theta, \phi) = u_0$ , which makes  $\mathcal{P} = 0$  at  $u_0$  and, consequently, all higher order terms besides the leading order disappear in (2.6). Then, Bondi momentum at  $u_0$  reads

$$P^\mu(u_0) = (P^0(u_0), \mathbf{P}(u_0)) = \frac{m_0}{4\pi} \oint_{S^2} \frac{(1, \hat{\mathbf{r}})}{Q^3(u_0, \theta, \phi)} dS, \tag{2.8}$$

in a reference frame with all BMS group degrees of freedom fixed.

<sup>1</sup> To know the explicit expression for  $\mathcal{P}$ , see [34].

Inspired by (1.42) - and as done previously in literature [25, 40]-, we define the center of mass velocity in the Bondi frame as

$$\mathbf{v}(u_0) = \frac{1}{P^0(u_0)} \mathbf{P}(u_0). \quad (2.9)$$

Since other recent works use different definitions<sup>2</sup>, we want to show that (2.9) is definitively right, and no other option is better to measure the velocity of the source. Then we perform the rotation that fix  $\mathbf{v}(u_0) = v\hat{\mathbf{z}}$  and do a Lorentz boost of  $-v\hat{\mathbf{z}}$ , as done in (1.42), which transformation is given by

$$\cos \theta' = \frac{\cos \theta + v}{1 + v \cos \theta}; \quad \phi' = \phi; \quad d\Omega'^2 = \frac{d\Omega^2}{\gamma^2(1 + v \cos \theta)^2}, \quad (2.10)$$

then we define<sup>3</sup>

$$Q_{\text{boost}}(u_0, \theta, \phi) = \gamma(1 + v \cos \theta) Q \left( u_0, \theta' = \arccos \left( \frac{\cos \theta + v}{1 + v \cos \theta} \right), \phi \right), \quad (2.11)$$

leading to the following spatial part of the Bondi momentum

$$P_{\text{boost}}^1(u_0) = P_{\text{boost}}^2(u_0) = 0, \quad P_{\text{boost}}^3(u_0) = \frac{m_0}{4\pi} \oint_{S^2} \frac{\cos \theta dS}{Q_{\text{boost}}^3 \left( u_0, \arccos \left( \frac{\cos \theta + v}{1 + v \cos \theta} \right), \phi \right)}. \quad (2.12)$$

Doing the coordinate change that matches the expression (2.10) in the last integral, we check that the momentum in  $z$  direction is also null

$$P_{\text{boost}}^3(u_0) = \gamma (P^3(u_0) - vP^0(u_0)) = 0. \quad (2.13)$$

This means that we were right, because  $-v\hat{\mathbf{n}}$  is the parameter of the Lorentz boost that stops the system, so (2.9) is indeed the instantaneous velocity of the source.

It must be clear to the reader that definition (2.9) works for any reference frame, but it is really hard to calculate it in a generic Bondi frame, where  $\mathcal{P}$  can be different from zero at  $u_0$  and the expression (2.8) does not work.

## 2.2 Time evolution

After all previous considerations about Bondi momentum, we are ready to investigate vacuum Einstein's equations for (2.1), that can be written as

$$6m_0 \frac{\partial}{\partial u} \left( \frac{1}{Q^2} \right) = \nabla_{\Omega}^2 K, \quad (2.14)$$

<sup>2</sup> In [26] the authors define the velocity of the source without taking  $P^0$  into account.

<sup>3</sup> The multiplicative factor in front of the following expression comes from  $d\Omega^2$  transformation, see (2.15) to be convinced that it is needed.

in which the  $r$  coordinate does not appear anywhere, and we can state an initial value problem just choosing a smooth  $Q(u = u_0, \theta, \phi)$ , *i. e.*, the time evolution is well defined with the metric of a given surface that is a continuous deformation of the sphere

$$ds^2|_{u=u_0, r=1} = \frac{d\Omega^2}{Q^2(u_0, \theta, \phi)}, \quad (2.15)$$

where the only restriction over  $Q(u_0, \theta, \phi)$  is that (2.8) converges in order to generate a valid physical example. The integration of (2.14) over  $S^2$  gives a conserved quantity along  $u$  evolution

$$q_0 = \oint_{S^2} \frac{dS}{Q^2(u_0, \theta, \phi)}, \quad (2.16)$$

that represents the area of (2.15), and we will fix  $q_0 = 4\pi$ , so the area of the  $r$  constant surfaces is  $4\pi r^2$  at any instant of time. Now one can recognize (2.14) as a two dimensional version of the Calabi flow associated to (2.15) [41], a known geometric flow that tends to dissipate non-uniformities in curvature. Regarding the fact that (2.14) is not linear, an interesting analogy can be done with the heat equation on  $S^2$ , leading an initial temperature distribution into a homogeneous one.

The stationary solution ( $u \rightarrow \infty$ ) must lead to a compact surface of positive curvature such that  $\nabla_\Omega^2 K = 0$ , then the only possibility is  $K = 1$  for  $S^2$  itself. The simplest case is when the sphere is centered at the origin and we have  $Q(u \rightarrow \infty, \theta, \phi) = 1$ . The general solution is when the center of  $S^2$  is at  $\mathbf{p} = v\hat{\mathbf{n}}$  with  $0 \leq v < 1$ , resulting in

$$Q(u \rightarrow \infty, \theta, \phi) = \gamma (1 - v\hat{\mathbf{n}} \cdot \hat{\mathbf{r}}), \quad (2.17)$$

with  $\gamma = (1 - v^2)^{-1/2}$  and  $\hat{\mathbf{r}} = (\cos \phi \sin \theta, \sin \phi \sin \theta, \cos \theta)$ . Substituting (2.17) in (2.1) we get a spherical BH with constant velocity  $v$ , as argued in (1.42). Then, when  $Q(u, \theta, \phi)$  is smooth, we can interpret (2.1) as the metric of a deformation of Schwarzschild spacetime for all  $u \geq u_0$ , *i. e.*, a non-spherical BH which radiates GWs until all its curvature inhomogeneities disappear<sup>4</sup>.

Since (2.14) is solved for a valid initial condition  $Q(u_0, \theta, \phi)$ , one can compute Bondi 4-momentum to quantify physical changes in the properties of the source and understand the emission process of GWs. Because spacetime is dynamical and  $U$  coordinate changes during the evolution, we emphasize that (2.8) is valid just for  $u_0$ , and it is necessary to use the conservation law (1.35) to compare energy or momentum between different instants of time. For this, we determine the lowest order approximation for  $\Psi_4$ , given by (1.9):

$$\Psi_4^{(0)} = -\frac{\sin \theta}{2r} \mathcal{D} \left( \frac{Q^2}{\sin \theta} \mathcal{D}(\partial_u \ln Q) \right). \quad (2.18)$$

<sup>4</sup> Here is where the analogy with the heat equation must be clear to the reader.

Regarding that  $\partial_u = Q\partial_U$  for large  $r$ , we write<sup>5</sup>

$$\frac{1}{R}\partial_U\bar{N} = \frac{1}{r}\partial_u\bar{N} = -\frac{\Psi_4^{(0)}(u, \theta, \phi)}{Q^2}. \quad (2.19)$$

Changing the order between the operators  $\mathcal{D}$  and  $\partial_u$  in (2.18) and then integrating (2.19) over  $u$ <sup>6</sup>, we get

$$N(u, \theta, \phi) = \frac{1}{Q} \left[ \frac{1}{2} \left( Q_{\theta\theta} - \frac{Q_\theta}{\tan\theta} - \frac{Q_{\phi\phi}}{\sin^2\theta} \right) + \frac{i}{\sin\theta} \left( Q_{\theta\phi} - \frac{Q_\phi}{\tan\theta} \right) \right], \quad (2.20)$$

with subscript coordinates representing partial derivatives. Finally, the conservation equation (1.35) reads

$$\begin{aligned} \frac{dP^\mu}{du} = & -\frac{1}{4\pi} \oint_{S^2} \frac{j^\mu}{Q} \left[ \frac{1}{4} \left( Q_{\theta\theta} - \frac{Q_\theta}{\tan\theta} - \frac{Q_{\phi\phi}}{\sin^2\theta} \right)^2 + \frac{1}{\sin^2\theta} \left( Q_{\theta\phi} - \frac{Q_\phi}{\tan\theta} \right)^2 \right] dS \\ & + \frac{1}{4\pi} \oint_{S^2} M_B(u, \theta, \phi) \frac{\partial j^\mu}{\partial u} dS. \end{aligned} \quad (2.21)$$

The second term has already been ignored in other references, as in [34], but we will show that its contribution is not negligible in section 5.2, at least for one example of initial data. If the second term was indeed zero, (2.21) would become a simple uncoupled ordinary differential equation (ODE) system with direct solution.

To end all the problems to compute Bondi momentum changes, we use the fact that the  $\mathcal{P}$  expression in (2.7) is null for Schwarzschild, so we can always choose the specific Bondi frame in which (2.8) is valid at the beginning of the evolution (at  $u = u_0$ ), and at the stationary solution (at  $u \rightarrow \infty$ ). Given all these considerations, we define the fraction of energy emitted  $\Delta$  and kick velocity  $\mathbf{v}_k$  as

$$\begin{aligned} \Delta &= \frac{P^0(u_0) - P^0(\infty)}{P^0(u_0)}; \\ \mathbf{v}_k &= \frac{1}{P^0(\infty)} \mathbf{P}(\infty) - \frac{1}{P^0(u_0)} \mathbf{P}(u_0). \end{aligned} \quad (2.22)$$

It is really important to understand that our goal is to compute (2.22) for different systems and compare them, but we can not get  $P^\mu(u \geq u_0)$  without fully solving (2.21), and we will not do it in this work.

## 2.3 Physical systems

As stated before, a proper initial condition  $Q(u_0, \theta, \phi)$  can be interpreted as a deformation of a spherical BH, since RT spacetimes always evolves into Schwarzschild case

<sup>5</sup> The extra  $Q^{-2}$  factor in (2.19) comes from the fact that we have calculated  $\Psi_4^{(0)}$  with the tetrad generated by  $\partial_r$ , and not  $\partial_R$ .

<sup>6</sup> It is important to state that (2.20) admits an arbitrary additional constant term, but this would represent a linear increase in  $\sigma_{(0)}$  for the stationary solution, which has no physical meaning.

and, if (2.8) converges, we can assign a 4-momentum for this source that does not measure any contribution from the GW content. However, there are three important restrictions for the possible Schwarzschild perturbations which limit the real physical systems that can be described by RT metrics.

The first one is that any kind of angular momentum in spacetime is forbidden, because we can understand the metric as a covariantly extended version of (2.15) in the null  $\partial_r$  direction, *i. e.*, photons always travel perpendicularly to  $u$  and  $r$  constant surfaces. Since  $\partial_r$  is torsion free, in the sense introduced in section 1.2, no rotations can appear. This is illustrated by the fact that (2.14) does not depend on  $r$ .

The second - and strongest - restriction comes from the fact that  $Q(u, \theta, \phi)$  must be at least four times differentiable with respect to  $\theta$  and  $\phi$  for the  $u$  evolution to make sense, so no discontinuities are allowed and (2.15) is indeed just a smooth deformation of the sphere. Since outgoing photons travel in  $\partial_r$  direction, any region that traps photons will be connected, there can only be one event horizon and, consequently, it is only possible to have just one BH on spacetime.

The third restriction says that the only way to start the evolution without any GW content is with the stationary solution itself. This happens because whenever  $K$  is not constant,  $\Psi_4$  is not zero and there must be GW presence in the system. This prohibits any static initial configuration that is not Schwarzschild spacetime.

Then, we need to find an one body non rotating problem that represents a compact source of GW emission in order to use all these tools developed until now. The simplest example of such phenomenon is a frontal collision of spherical BHs, where all the initial bodies merge with each other in a single BH. After this merging, since no angular momentum appears and there were some previous GW emission, we must be able to describe the system with RT metric. The hard task is to find an appropriate initial condition that describes a post-merger phase of a collision, since there are too many possibilities for  $Q(u_0, \theta, \phi)$ , but this will be discussed in chapter 4.

For now, let us think of a binary head-on (frontal) collision in a reference frame such that the system is symmetric with respect to rotations around an axis, as represented in Figure 4 below. This example makes clear the difference between the phases of a BH merger because of the “antikick” property, that separates each of them [40]. Before they merge, while both BHs fall into each other, the smaller BH develops more velocity, then it emits more GWs in comparison with the bigger one and the center of mass frame feels a recoil in the direction of the smaller BH. After the merging, the resulting non-spherical BH can be described as a RT spacetime and it certainly presents more curvature inhomogeneity in the side that the smaller BH was before the collision, the preferred direction of emission inverts itself and the system feels a decrease in the source velocity, as illustrated in Figure 4.

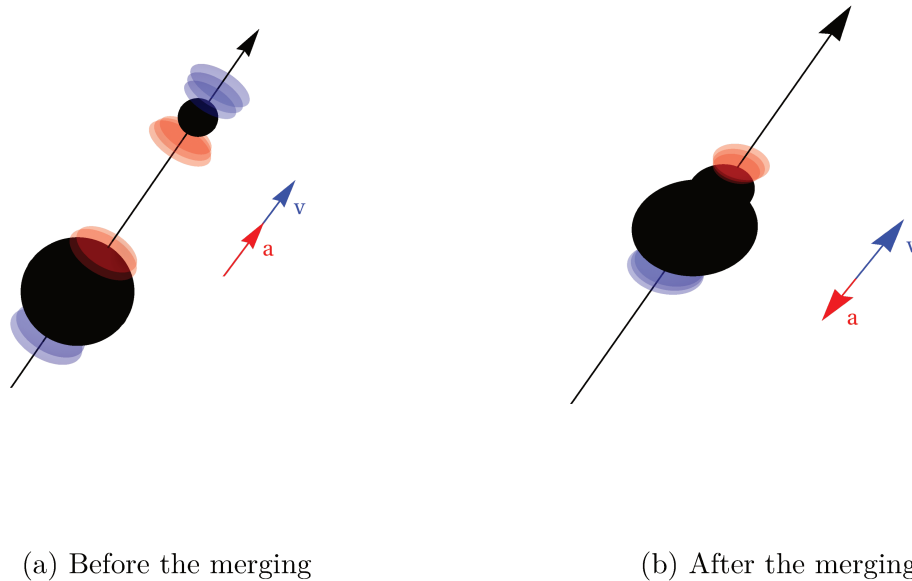


Figure 4 – Two stages of a head-on binary collision of spherical black holes. Here red wave regions represent higher front wave densities compared to blue regions for each source. The velocity and acceleration of the center of mass frame are represented with blue and red arrows respectively.

This deceleration, called the “antikick”, can be found in more complex situations, as in the case of collisions of spinning BHs [42], but the descriptions of such systems are done by full numerical (3 + 1) integration of Einstein’s equations, without any simplification as (2.14). Then, it is interesting to know that the post-merger phase can show this kind of effect even in simpler cases, including the ones that RT spacetimes describe and give intuition. A quantitative discussion about the relation between the “antikick” and the curvature of the resulting apparent horizon<sup>7</sup> after the merger can be found in [40].

## 2.4 About the causal structure

Here we briefly discuss the difficulties on understanding RT global causal structure, and how they can lead to the misinterpretation that RT is just a white hole spacetime without any promise to describe real systems. This section is independent from the rest of the work, but it gives a natural argument for the necessity of using Bondi 4-momentum to guide any physical interpretation around the properties of the source. The main point is that the Calabi flow given by (2.14) is not well defined backward in time. We will not prove this statement, but we know that any regular initial data will evolve into a stationary Schwarzschild BH, then the system will not have any dynamics

<sup>7</sup> Because we are dealing with dynamical BH spacetimes, it is easier to define the local analogue of event horizon, the apparent horizon.

for forward or backward  $u$  evolution, and it is not possible to recover initial data. The situation is analogous to the heat equation again: in the same way that one can not decide from which initial condition an object started in order to get to a specific temperature distribution, we can not compute which  $Q(u < u_1, \theta, \phi)$  led the system into  $Q(u_1, \theta, \phi)$ .

This problem introduces two restrictions. Directly, it is not possible to access the past null infinite ( $\mathcal{I}^-$ ) of any given initial data. Indirectly, since (2.1) is written with a retarded time, the range of our coordinates run only through the white hole and the asymptotically flat regions of the solution, without access to the future event horizon. This is an indirect implication because if we try to change variables to an advanced time  $u \rightarrow -u$ , the  $u$  partial derivative in (2.14) changes sign, the evolution turns to be defined only backward in time and we will only be able to get the apparent horizon of a BH that has started as Schwarzschild and has been absorbing GWs from  $u \rightarrow -\infty$  until  $u = u_0$ , which is really different from the system we are studying.

To illustrate these facts we can build a sketch of the Penrose diagram for a RT spacetime, which follows in Figure 5. Just by looking at Figure 5, one could argue that

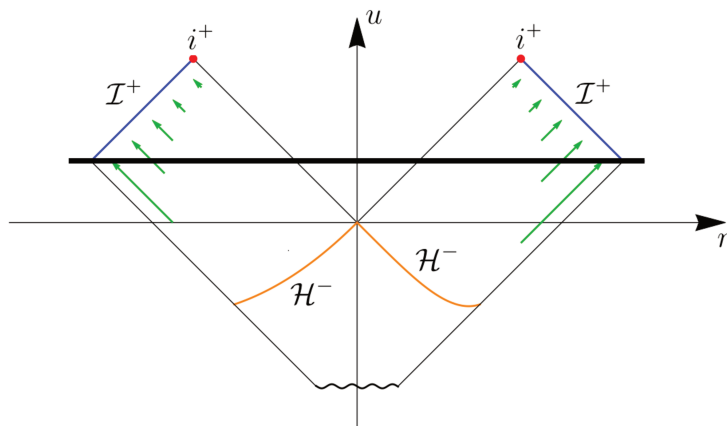


Figure 5 – Sketch of the Penrose diagram for a RT spacetime. Here  $\mathcal{I}^+$  is the future null infinity (in blue),  $\mathcal{H}^-$  is the past horizon (in orange),  $i^+$  is the future timelike infinity (red dot), GWs are represented by green arrows and negative  $r$  denotes an antipodal point on  $(\theta, \phi)$  for the same  $r$  value.

(2.1) is not a good metric candidate to describe the post-merger phase of a BH collision, since only a past apparent horizon<sup>8</sup> ( $\mathcal{H}^-$ ) can be computed from it [40]. However, the solution evolves into Schwarzschild for  $u \rightarrow \infty$  and no collapse took place, so there must have been a BH region from somewhere in time during the evolution, even though we can not determine its shape with our restricted range solution.

Then, we may look at a sketch of a collapse of two BHs, followed by their collision, represented in Figure 6. Comparing both diagrams, we see that an observer out of the horizons and above the thick black line may not tell the difference between a

<sup>8</sup> The apparent horizon of a white hole region of spacetime.

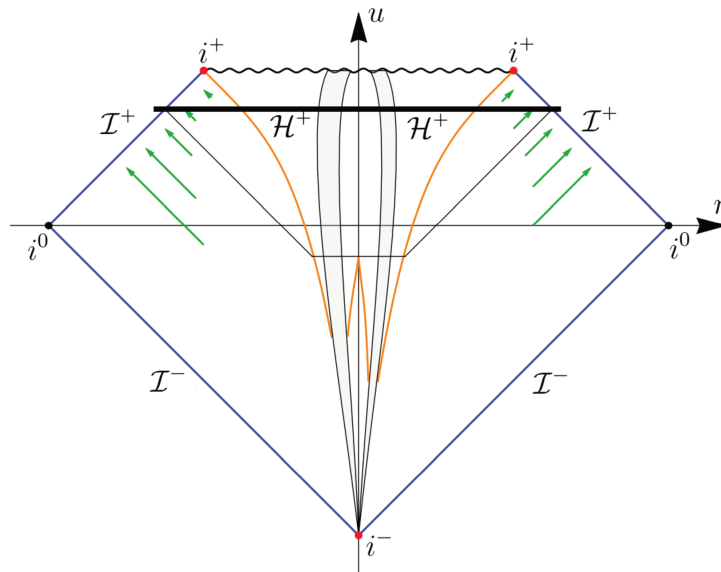


Figure 6 – Sketch of the Penrose diagram for a binary collision of BHs, each one generated by its own gravitational collapse. Here  $\mathcal{I}^+$  and  $\mathcal{I}^-$  are future and past null infinities (in blue),  $\mathcal{H}^+$  is the future horizon (in orange),  $i^+$  and  $i^-$  are the future and past timelike infinities (red dots),  $i^0$  is the spacelike infinity (black dots), GWs are represented by green arrows, the worldtubes of matter content are drawn in gray and negative  $r$  denotes an antipodal point on  $(\theta, \phi)$  for the same  $r$  value.

full collapse/collision spacetime and a RT solution just by measuring the gravitational interaction in it. With the right initial condition  $Q(u_0, \theta, \phi)$ , even their GW content can be identical, and the observer would need to interact with light rays or test particles coming from his past light cone in order to decide in which spacetime is him. Since we use Bondi 4-momentum to infer physical properties of the source in the whole work, only the curvature near  $\mathcal{I}^+$  is used in the computations and we do not need to concern with the non physical white hole region in Figure 5.

It is important to state that this argument is not new, since we are used to describe the exterior region of a single spherical BH that came from a gravitational collapse using Schwarzschild metric, which maximal extension has a white hole region, as we can see in Figure 7 below. The main difference from our case is that the right initial data must be chosen for RT to represent the post-merger phase of a BH collision, and we will discuss about this choice in chapter 4.

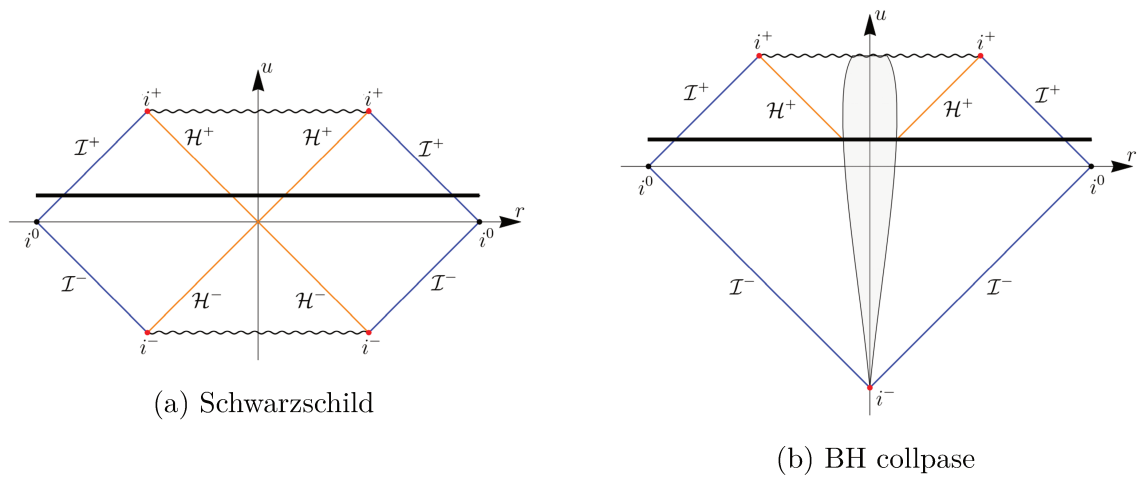


Figure 7 – Penrose diagrams of Schwarzschild and a single spherical BH collapse. Here  $\mathcal{I}^+$  and  $\mathcal{I}^-$  are future and past null infinities (in blue),  $\mathcal{H}^+$  and  $\mathcal{H}^-$  are the future and past horizons (in orange),  $i^+$  and  $i^-$  are the future and past timelike infinities (red dots),  $i^0$  is the spacelike infinity (black dots), the worldtube of matter content is drawn in gray and negative  $r$  denotes an antipodal point on  $(\theta, \phi)$  for the same  $r$  value.

## 3 Galerkin Method

In this chapter we describe how a Galerkin spectral method is used to solve (2.14) numerically, with a standard spherical harmonics expansion of  $Q(u, \theta, \phi)$ . We argue why our strategy is more efficient than the previous attempts in the literature for the general case of  $u$  evolution. Based on this strategy, we find some properties of initial conditions with planar reflection and axis rotation symmetries. Also, all important features about the structure of the codes used to present numerical examples of time evolution are considered.

### 3.1 General case

Time evolution of RT spacetimes is described by (2.14), a nonlinear fourth order partial differential equation (PDE), then there is no standard analytical method to solve it. Interested in the  $u$  evolution generated from arbitrary  $Q(u_0, \theta, \phi)$ , one can use a Galerkin spectral method [43] and change this PDE by an ODE system, with aid of projections of the PDE on a basis of the space generated by some chosen functions. This strategy introduces a new way to look at the problem, determining the evolution of each term of a modal expansion for the quantity to be evolved.

The best way to understand the procedure is with an example and, in our case, we can perform a spherical harmonics decomposition as follows

$$Q_N(u, \theta, \phi) = \sum_{l=0}^N \sum_{m=-l}^l b_m^l(u) Y_l^m(\theta, \phi), \quad (3.1)$$

where all  $u$  dependency is carried by the modal coefficients  $b_m^l(u)$ . This is possible because the spherical harmonics form an orthogonal basis for the space of functions on  $S^2$ , so any analytic function can be arbitrarily approximated by (3.1) for large  $N$ . The expression of  $Y_l^m$  adopted in this work is<sup>1</sup>

$$Y_l^m(\theta, \phi) = \sqrt{\frac{(l-m)!}{(l+m)!}} P_l^m(\cos \theta) e^{im\phi}, \quad (3.2)$$

where  $P_l^m(x)$  are the associated Legendre functions and the orthogonality relation reads

$$\langle Y_l^m, Y_{l'}^{m'} \rangle = \oint_{S^2} \bar{Y}_l^m Y_{l'}^{m'} dS = \frac{4\pi}{2l+1} \delta_{ll'} \delta_{mm'}. \quad (3.3)$$

<sup>1</sup> This definition is known as Schmidt semi-normalization for spherical harmonics.

Then, it is possible to write (2.14) as

$$\frac{\partial Q(u, \theta, \phi)}{\partial u} = \sum_{l=0}^N \sum_{m=-l}^l \dot{b}_m^l(u) Y_l^m(\theta, \phi) = -\frac{1}{12m_0} Q^3 \nabla_{\Omega}^2 K, \quad (3.4)$$

with dots representing  $u$  derivatives. Applying  $\langle Y_l^m, \cdot \rangle$  to both sides of (3.4), we get the following  $(N+1)^2$  ODE system

$$\dot{b}_m^l = -\frac{2l+1}{48\pi m_0} \langle Y_l^m, Q^3 \nabla_{\Omega}^2 K \rangle, \quad (3.5)$$

with  $l = 0, 1, \dots, N$  and  $-l < m < l$ .

Essentially, this is the last step that Galerkin method leads us and a numerical integration of (3.5) is enough to find the  $u$  evolution. Then, an important obstacle appears during the implementation of this strategy: the projections in (3.5) are given by integrals of expressions depending on many  $P_l^m$  functions, which oscillates a lot for high  $m$  modes, so the numerical approach to determine the ODE system is not precise. To overcome this, one can simplify the projections introducing a Galerkin decomposition<sup>2</sup> for the Gaussian curvature

$$K_N(u, \theta, \phi) = \sum_{l=0}^{2N} \sum_{m=-l}^l a_m^l(u) Y_l^m(\theta, \phi) \quad (3.6)$$

and for  $G(u, \theta, \phi) = Q^3(u, \theta, \phi)$

$$G_N(u, \theta, \phi) = \sum_{l=0}^{3N} \sum_{m=-l}^l c_m^l(u) Y_l^m(\theta, \phi), \quad (3.7)$$

as done in [27]. Joining (3.5) with all Galerkin expansions and the identity

$$\nabla_{\Omega}^2 Y_l^m(\theta, \phi) = -l(l+1) Y_l^m(\theta, \phi), \quad (3.8)$$

we have

$$\dot{b}_m^l = \frac{2l+1}{24m_0} \sum_{\substack{l_1, l_2 \\ m_1, m_2}} l_1(l_1+1) a_{m_1}^{l_1} c_{m_2}^{l_2} C_m^l(l_1, m_1; l_2, m_2), \quad (3.9)$$

where the summation is carried over the values  $0 \leq l_1 \leq 2N, 0 \leq l_2 \leq 3N, -l_i \leq m_i \leq l_i$ , and the coefficients  $C_m^l$  are given by

$$\begin{aligned} C_m^l(l_1, m_1; l_2, m_2) &= \frac{1}{2\pi} \oint_{S^2} Y_{l_1}^{m_1} Y_{l_2}^{m_2} \bar{Y}_l^m dS \\ &= \delta_{Mm} \sqrt{\frac{(l-m)!}{(l+m)!}} \int_{-1}^1 P_l^m(x) \prod_{i=1}^2 \sqrt{\frac{(l_i - m_i)!}{(l_i + m_i)!}} P_{l_i}^{m_i}(x) dx, \end{aligned} \quad (3.10)$$

where  $M = m_1 + m_2$  and the resulting integrals are much easier to determine.

<sup>2</sup> The following expansions run throughout higher order modes compared with the  $Q$  decomposition and the reason will be clarified later.

To proceed, we use (3.6) and (2.2) to write  $a_m^l$  as a function of  $b_m^l$ . Using identity (3.8) again, one has

$$a_m^l = \frac{2l+1}{2} \sum_{\substack{l_1, l_2 \\ m_1, m_2}} b_{m_1}^{l_1} b_{m_2}^{l_2} \left[ (1 - l_2(l_2 - 1)) C_m^l(l_1, m_1; l_2, m_2) + \right. \\ \left. - D_m^l(l_1, m_1; l_2, m_2) + m_1 m_2 E_m^l(l_1, m_1; l_2, m_2) \right], \quad (3.11)$$

where the coefficients  $D_m^l$  and  $E_m^l$  are given by

$$D_m^l(l_1, m_1; l_2, m_2) = \delta_{Mm} \sqrt{\frac{(l-m)!}{(l+m)!}} \int_{-1}^1 (1-x^2) P_l^m(x) \prod_{i=1}^2 \sqrt{\frac{(l_i - m_i)!}{(l_i + m_i)!}} \frac{dP_{l_i}^{m_i}(x)}{dx} dx, \quad (3.12)$$

$$E_m^l(l_1, m_1; l_2, m_2) = \delta_{Mm} \sqrt{\frac{(l-m)!}{(l+m)!}} \int_{-1}^1 \frac{P_l^m(x)}{(1-x^2)} \prod_{i=1}^2 \sqrt{\frac{(l_i - m_i)!}{(l_i + m_i)!}} P_{l_i}^{m_i}(x) dx. \quad (3.13)$$

In the same way, but now for  $c_m^l$ , we write

$$c_m^l = \frac{2l+1}{2} \sum_{\substack{l_1, l_2, l_3 \\ m_1, m_2, m_3}} b_{m_1}^{l_1} b_{m_2}^{l_2} b_{m_3}^{l_3} F_m^l(l_1, m_1; l_2, m_2; l_3, m_3), \quad (3.14)$$

with  $0 \leq l_i \leq N$ ,  $-l_i \leq m_i \leq l_i$  and

$$F_m^l(l_1, m_1; l_2, m_2; l_3, m_3) = \delta_{\tilde{M}m} \sqrt{\frac{(l-m)!}{(l+m)!}} \int_{-1}^1 P_l^m(x) \prod_{i=1}^3 \sqrt{\frac{(l_i - m_i)!}{(l_i + m_i)!}} P_{l_i}^{m_i}(x) dx, \quad (3.15)$$

where  $\tilde{M} = m_1 + m_2 + m_3$ . Then, to reach each new numerical integration step for the  $(N+1)^2$  EDO's (3.9), the evaluation of (3.11) and (3.14) is necessary. The good news is that all the integrals required to compute (3.10), (3.12), (3.13) and (3.15) are easily determined by an algebraic manipulation software. Even so, there are too many of them (mainly the  $F$  ones) and the selection rules for null coefficients (B.2-B.4) of Appendix B help a lot. Also, the rule (B.4) together with the expressions (3.11) and (3.14), determine the order to stop the expansions (3.6) and (3.7), in order to discard all unused  $a_m^l$  and  $c_m^l$  in (3.5) for a given  $N$ , but without losing any information.

After handling all those wild integrals, the last simplification for a generic case evolution comes from the fact that  $Q(u_0, \theta, \phi)$  is real ( $Q = \bar{Q}$ ) and, because spherical harmonics are orthogonal, the modal coefficients must obey

$$b_{-m}^l = (-1)^m \bar{b}_m^l, \quad (3.16)$$

so the evolution (3.9) can be expressed in terms of non negative  $m$  modes only, leading to a  $N(N+1)/2$  EDO system, reducing the computational time for  $u$  evolution. The same is valid for (3.11) and (3.14), since  $K$  and  $G$  are also real. United with the selection rules of Appendix B, this procedure is certainly faster than the previous strategy presented in

the literature [27], that is based on the real spherical harmonics decomposition of  $Q$  to perform the  $u$  integration.

For the stationary condition (2.17), we see that the only non vanishing final modal coefficients must be  $b_0^0$  and  $b_m^1$ . Then, in any Bondi frame, one has

$$\gamma(\infty) = b_0^0; \quad v_x(\infty) = \frac{b_1^1 + \bar{b}_1^1}{\sqrt{2}b_0^0}; \quad v_y(\infty) = i\frac{b_1^1 - \bar{b}_1^1}{\sqrt{2}b_0^0}; \quad v_z(\infty) = -\frac{b_0^1}{b_0^0}. \quad (3.17)$$

## 3.2 Planesymmetric case

If  $Q(u_0, \theta, \phi)$  has symmetry of reflection with respect to a plane, a useful simplification in its expansion is possible and, in some sense, the motion stays in this plane. In terms of spherical coordinates, we write the reflection with respect to  $y = 0$  as  $(\theta, \phi) \rightarrow (\theta, -\phi)$ , which leads to  $Y_l^m(\theta, \phi) \rightarrow (-1)^m Y_l^{-m}(\theta, \phi)$ . If we impose symmetry with respect to this transformation over the initial condition, the modal coefficients obey

$$b_{-m}^l(u_0) = (-1)^m b_m^l(u_0), \quad (3.18)$$

which, together with (3.16), demands  $b_m^l(u_0)$  to be real. Then, combining (2.8) with  $Q(u_0, \theta, \phi) = Q(u_0, \theta, -\phi)$ , we conclude that there is no initial Bondi momentum in the  $\hat{y}$  direction. Since the coefficients of the ODE system (3.5) are also real, implying that  $b_m^l(u)$  must be real for  $u > u_0$  too. This means that there is no Bondi momentum in the  $y$  axis at any time, there is no velocity out of the plane  $y = 0$  and we will refer to this kind of system just by planesymmetric ones from now on.

It is important to notice that we just showed that motion is stuck in  $y = 0$  for  $Q_N$  defined in (3.1), but this also holds for any solution that is generated by an analytic initial condition, since all spherical harmonics expansions can be done for arbitrarily high  $N$ . As well, a planesymmetric  $Q(u_0, \theta, \phi)$  with respect to any plane must carry this property, since it is always possible to change coordinates and put this specific plane at  $y = 0$ . Also, the stationary velocity given by (3.17) becomes

$$\gamma(\infty) = b_0^0; \quad v_x(\infty) = \frac{\sqrt{2}b_1^1}{b_0^0}; \quad v_y(\infty) = 0; \quad v_z(\infty) = -\frac{b_0^1}{b_0^0}. \quad (3.19)$$

Examples to illustrate the plane reflection symmetry condition can be found in the end of [section 4.3](#).

## 3.3 Axisymmetric case

Another special case is when the system has symmetry of rotation with respect to the  $z$  axis ( $\phi \rightarrow \phi + \epsilon$ ,  $\epsilon \in [0, 2\pi]$ ), then only  $m = 0$  modes are not zero, the ones that

do not depend on  $\phi$ . This condition demands reflection symmetry with respect to both  $x = 0$  and  $y = 0$  planes, so Bondi momentum of the source must remain in the intersection of these planes, the  $z$  axis. Besides that, the spherical harmonics in (3.1) become ordinary Legendre polynomials

$$Q_N(u, \theta) = \sum_{l=0}^N b^l(u) P_l(\cos \theta), \quad (3.20)$$

all  $\phi$  integrals are trivial and the normalization condition simplifies to

$$\frac{q_0}{2\pi} = \int_0^\pi \frac{\sin \theta}{Q^2(u_0, \theta)} d\theta = 2. \quad (3.21)$$

In this case, (3.5) can be determined by an algebraic manipulation software without too many effort and, depending on the computational power available, there is no need to introduce the expansions (3.6) and (3.7). Also, the stationary velocity given by (3.17) becomes

$$\gamma(\infty) = b^0; \quad v_x(\infty) = 0; \quad v_y(\infty) = 0; \quad v_z(\infty) = -\frac{b^1}{b^0}. \quad (3.22)$$

At last, it is possible to have any combination of planar reflection conditions, resulting in other cases with even more simplifications compared to the axisymmetric case. Any initial condition that is planesymmetric with respect to two intersecting planes will also have linear momentum in just one direction, but it is also possible to end with no velocity change at all. If we add one more plane of reflection that crosses the intersection of the others at only one point, the system will not have a preferred direction of GW emission and it can not present gravitational recoil. In this case, the spatial part of Bondi momentum will always be null in the center of mass frame, there will be no kick velocity, final energy is just  $m_0$  and the fraction of energy emitted becomes

$$\Delta = \frac{P^0(u_0) - m_0}{P^0(u_0)} = 1 - 4\pi \left( \oint_{S^2} \frac{dS}{Q^3(u_0, \theta, \phi)} \right)^{-1}, \quad (3.23)$$

or even simpler when the system is also axisymmetric

$$\Delta = 1 - 2 \left( \int_0^\pi \frac{\sin \theta d\theta}{Q^3(u_0, \theta)} \right)^{-1}. \quad (3.24)$$

## 4 Initial Conditions and Analytic Cases

In this chapter we present the standard derivation of Brill-Lindquist (BL) initial data for axisymmetric RT spacetimes. Our derivation includes the case of a post-merger phase of a binary BH collision with different velocities for each BH, not just equal velocities as in previous literature. With the aid of the BMS group, we perform Lorentz boosts in the system to better understand properties of BL initial data. Then, inspired by the boosted binary case, we claim a general initial condition for the post-merger phase of a head-on collision involving any number of BHs. Also, all Bondi mass plots in green represent initial data in its center of mass frame at  $u_0$ .

### 4.1 Axisymmetric binary collision

The example of the post-merger phase given in [section 2.3](#) can be represented by an axisymmetric  $Q(u_0, \theta, \phi)$ , given by a specific procedure that borrows the geometry of a flat three dimensional space, and uses it to build a metric that approaches Schwarzschild at large distances from the origin, the BL initial data. The derivation that follows is based on the one in [\[27\]](#). We use the bispherical coordinates of the three dimensional flat space

$$\begin{aligned} x &= \frac{a \sin \theta \sinh \eta}{\cosh \eta + \cos \theta \sinh \eta} \cos \phi, \\ y &= \frac{a \sin \theta \sinh \eta}{\cosh \eta + \cos \theta \sinh \eta} \sin \phi, \\ z &= \pm \frac{a}{\cosh \eta + \cos \theta \sinh \eta}, \end{aligned} \tag{4.1}$$

where  $0 \leq \eta < \infty$ ,  $\theta \in [0, \pi]$ ,  $\phi \in [0, 2\pi)$  and  $a > 0$ . In these coordinates, the position vector has length

$$\rho(\eta, \theta) = a \sqrt{\frac{\cosh \eta - \cos \theta \sinh \eta}{\cosh \eta + \cos \theta \sinh \eta}} \tag{4.2}$$

and the line element for a flat space is given by

$$ds_{\text{flat}}^2 = \frac{c_0^2}{\Phi^4} \left( d\eta^2 + (\sinh^2 \eta) d\Omega^2 \right), \tag{4.3}$$

where  $c_0$  is constant and

$$\Phi = S(\eta, \theta, \phi, \hat{\mathbf{n}}) = \sqrt{\cosh \eta + (\hat{\mathbf{n}} \cdot \hat{\mathbf{r}}) \sinh \eta}. \tag{4.4}$$

Based on the [\(4.4\)](#), we choose a different expression for  $\Phi$  to substitute in [\(4.3\)](#), given by

$$\Phi^{-1} = \frac{\alpha_1}{S(\eta + \eta_1, \theta, \phi, \hat{\mathbf{z}})} + \frac{\alpha_2}{S(\eta + \eta_2, \theta, \phi, -\hat{\mathbf{z}})}, \tag{4.5}$$

with  $\alpha_i > 0$ , getting to a non-flat space that approaches a conformally flat geometry at large distances, *i. e.*,

$$ds^2 \approx \left( 1 + \frac{\alpha_2}{\alpha_1} e^{\frac{\eta_1 - \eta_2}{2}} \sqrt{\frac{\cosh \eta + \cos \theta \sinh \eta}{\cosh \eta - \cos \theta \sinh \eta}} \right)^4 ds_{\text{flat}}^2 \quad (4.6)$$

for  $\eta \gg \eta_i$ . Also, when  $\eta \gg 1$  too, the geometry approaches the spatial part of Schwarzschild far from the origin, and the metric reads

$$g_{ij} \approx \left\{ 1 + \frac{2M_0}{\rho} \right\} \delta_{ij}, \quad (4.7)$$

where the scales have been fixed in the way that

$$a = \frac{M_0 \alpha_1 e^{\frac{\eta_2 - \eta_1}{2}}}{2\alpha_2}. \quad (4.8)$$

Then, a surface of constant  $\eta = \eta_0 > 0$  can be used to generate an initial condition for (2.14) as follows

$$\begin{aligned} Q(u_0, \theta, \phi) &= \left( \frac{\alpha_1}{S(w_1, \theta, \phi, \hat{\mathbf{z}})} + \frac{\alpha_2}{S(w_2, \theta, \phi, -\hat{\mathbf{z}})} \right)^{-2} \\ &= \left( \frac{\alpha_1}{\sqrt{\gamma_1(1 + w_1 \cos \theta)}} + \frac{\alpha_2}{\sqrt{\gamma_2(1 - w_2 \cos \theta)}} \right)^{-2} = Q(u_0, \theta) \end{aligned} \quad (4.9)$$

where  $0 \leq w_i = \tanh(\eta_0 + \eta_i) < 1$  and  $\gamma_i = (1 - w_i^2)^{-1/2}$ . This is the BL initial data and it represents the post-merger phase of a head-on binary collision of black holes.

The physical interpretation of the control parameters in (4.9) is far from being direct. If we take  $\alpha_1 = 1$  and  $\alpha_2 = 0$ , the solution becomes a Schwarzschild black hole with mass  $m_0$  and constant velocity  $w_1$ . This induces us to associate the  $w_i$  parameters with some kind of velocities. In order to better understand the BL initial condition, we will use a Bondi frame with fixed degrees of freedom for supertranslations, and perform a Lorentz boost to go to the instantaneous rest frame of the system. First we determine the velocity of the source  $v$  in the Bondi frame which (2.8) is valid, then we apply the transformation given by (2.10) to stop the system at the initial time  $u_0$ . The result reads

$$\begin{aligned} Q'(u_0, \theta) &= \left( \frac{\alpha_1}{\sqrt{\gamma_1(1 + w_1 \cos \theta')}} + \frac{\alpha_2}{\sqrt{\gamma_2(1 - w_2 \cos \theta')}} \right)^{-2} \gamma(1 + v \cos \theta) \\ &= \left( \frac{\alpha_1}{\sqrt{\gamma'_1(1 + w'_1 \cos \theta)}} + \frac{\alpha_2}{\sqrt{\gamma'_2(1 - w'_2 \cos \theta)}} \right)^{-2} \\ &= \left( \frac{\alpha_1}{S(w'_1, \theta, \phi, \hat{\mathbf{z}})} + \frac{\alpha_2}{S(w'_2, \theta, \phi, -\hat{\mathbf{z}})} \right)^{-2}. \end{aligned} \quad (4.10)$$

The parameters  $w_i$  have been changed into  $w'_i = \frac{w_i \pm v}{1 \pm v w_i}$ , exactly as ordinary velocities should do, so they may represent the kinematic properties of some entity of the system.

Before trying to understand which entity the  $w_i$  parameters represent, it is important to notice that the special case  $\alpha_1 = \alpha_2$  always demands  $w'_1 = w'_2$  in (4.10), since it is the only way to set (2.8) to zero. Because there is symmetry of reflection with respect to the plane  $z = 0$  in the center of mass frame, an initial condition with  $\alpha_1 = \alpha_2$  can only represent a binary collision of two equal mass BHs. As seen in section 3.3, there is no kick velocity in this case and we use (3.24) to determine the fraction of energy emitted ( $\Delta$ ). All  $\Delta$  values for  $\alpha_1 = \alpha_2$  follow in Figure 8. From the graph we see that emission is symmetric

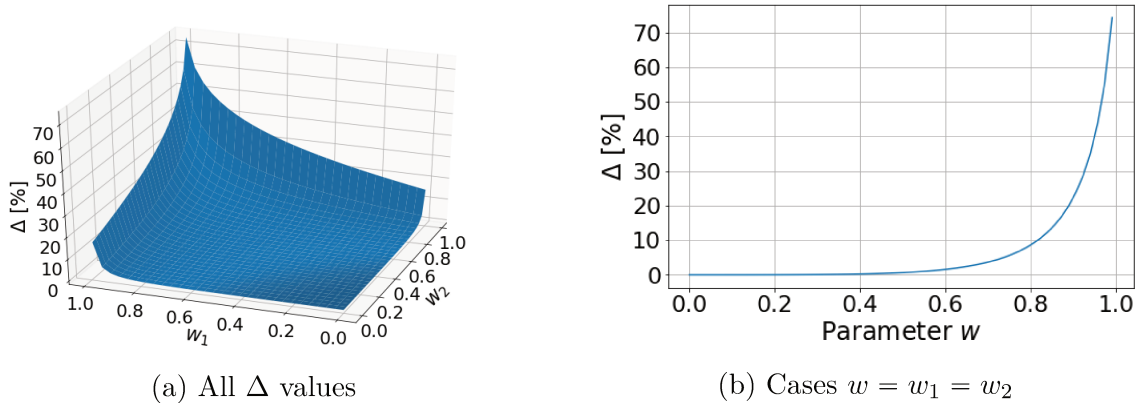


Figure 8 – Fraction of energy emitted  $\Delta$  for each case of (4.9) with  $\alpha_1 = \alpha_2$ .

by interchanging  $w_1$  and  $w_2$ . Also  $\Delta$  always get higher when  $w_1$  or  $w_2$  grows. Since the system does not have recoil in any Lorentz frame, the energy loss can only mean that GWs indeed consume mass from the source of GW emission, as discussed in Introduction and proved with (1.29).

To illustrate the stopping procedure done in all calculations when  $w_1 \neq w_2$ , Figure 9 follows with the plot of Bondi mass aspect before and after the performed boost for the example of  $w_1 = 0.7$  and  $w_2 = 0.5$ .

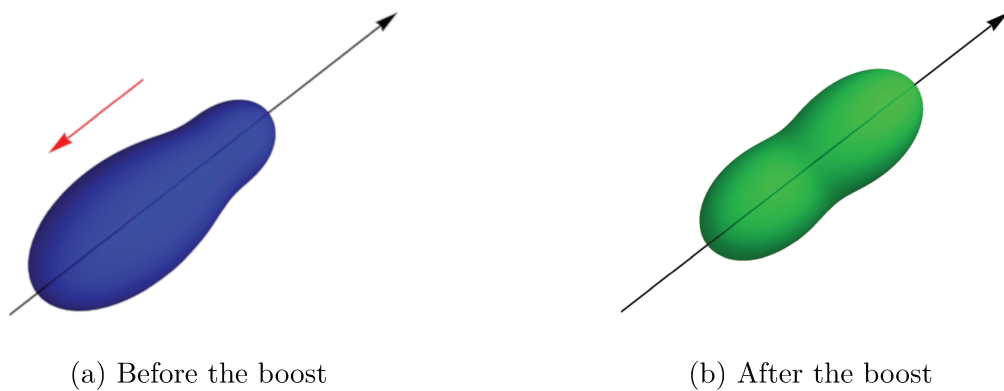


Figure 9 – Bondi mass aspect of a BL initial condition with  $\alpha_1 = \alpha_2$  and velocities  $w_1 = 0.7$ ,  $w_2 = 0.5$ . The velocity of the system before the stopping boost is represented by the red arrow.

When  $\alpha_1 \neq \alpha_2$ , the system has asymmetries in the instantaneous rest frame



the shape of the event horizon after merging, *i. e.*, [Figure 4b](#) is intrinsically different from [Figure 10](#), and the procedure to determine the exact shape of the apparent horizon<sup>1</sup> can be found in [44]. Even so,  $M_B(u, \theta, \phi)$  must have the same overall symmetries as the horizons and it also has its geometry very close to (2.15), so we will use its shape in the center of mass frame in order to guide our intuition around GW emission from now on.

## 4.2 Non axisymmetric binary collision

The choice of antipodal  $\hat{\mathbf{n}}_i$  in (4.4) to generate (4.9) is not arbitrary, any other possibility would have a different kind of big  $\eta$  behavior apart from (4.7). In other words, it is not easy to get a non-axisymmetric BL case by the same way done before. Even so, it is possible to analyze (4.9) in different reference frames, we just need to perform a Lorentz boost (1.41) in any direction orthogonal to  $\hat{\mathbf{z}}$ . The transformation for a boost of  $v\hat{\mathbf{x}}$  is given by

$$\begin{aligned}\cos \theta' &= \frac{\cos \theta}{\gamma(1 - v \cos \phi \sin \theta)}; \\ \cos \phi' \sin \theta' &= \frac{\cos \phi \sin \theta - v}{(1 - v \cos \phi \sin \theta)}; \\ d\Omega'^2 &= \frac{d\Omega^2}{\gamma^2(1 - v \cos \phi \sin \theta)^2},\end{aligned}\tag{4.11}$$

resulting in

$$\begin{aligned}Q'(u_0, \theta, \phi) &= \left( \frac{\alpha_1}{\sqrt{\gamma_1(1 + w_1 \cos \theta')}} + \frac{\alpha_2}{\sqrt{\gamma_2(1 - w_2 \cos \theta')}} \right)^{-2} \gamma(1 - v \cos \phi \sin \theta) \\ &= \left( \frac{\alpha_1}{S(w'_1, \theta, \phi, \hat{\mathbf{n}}'_1)} + \frac{\alpha_2}{S(w'_2, \theta, \phi, \hat{\mathbf{n}}'_2)} \right)^{-2},\end{aligned}\tag{4.12}$$

which we call the general BL-2 initial data. In (4.12), the vectors  $w_i(\pm\hat{\mathbf{z}})$  were transformed into  $w'_i\hat{\mathbf{n}}'_i = (v, 0, \pm w_i/\gamma)$ , as ordinary velocities should do. Then, the association of  $-w\hat{\mathbf{n}}_i$  with blob velocities is still valid. An example of the case  $\alpha_1 = \alpha_2$ ,  $w_1 = 0.7$ ,  $w_2 = 0.5$  with a boost of  $0.25\hat{\mathbf{x}}$  follows in [Figure 11](#). In this case both blobs earned kinetic energy with the boost, and the system clearly lost its axial symmetry.

Here we can also solve all  $q = 1$  cases analytically with the same strategy used in [section 4.1](#). To do this, we define an initial condition with  $\alpha_1 = \alpha_2$ , but with an angle  $\beta$  between the vectors  $\hat{\mathbf{n}}_1$  and  $-\hat{\mathbf{n}}_2$ <sup>2</sup>, then we perform a stopping boost and use (3.24) to determine the fraction of energy emitted, since the system is axisymmetric in this reference frame. [Figure 12](#) below exhibits the values of  $\Delta$  in the case of equal intensity blob velocities  $w$  for this case of BL-2 initial data. As  $\beta$  gets higher, the components of

<sup>1</sup> Again, we are dealing with dynamical BH spacetimes, so it is easier to work with apparent horizons, which definition can be also found in [44].

<sup>2</sup> This means that blob velocities are antiparallel for  $\beta = 0$ , orthogonal for  $\beta = \frac{\pi}{2}$  and parallel for  $\beta = \pi$ .

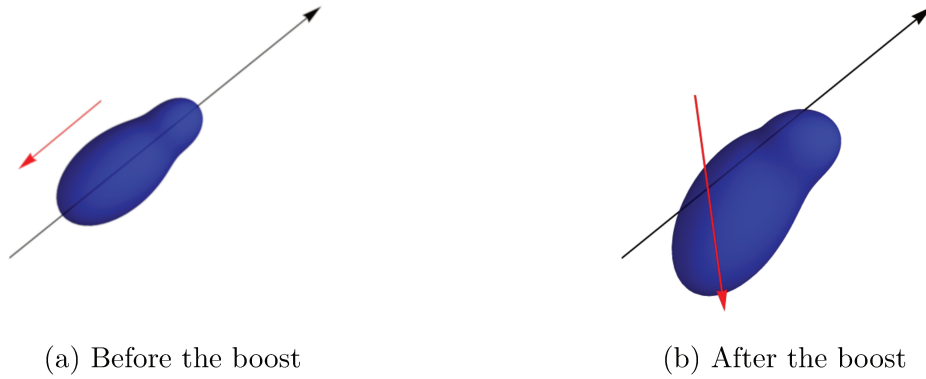


Figure 11 – Bondi mass aspect of a BL-2 initial condition with  $\alpha_2/\alpha_1 = 1$  and blob velocities  $w_1 = 0.7$  and  $w_2 = 0.7$ . The center of mass velocity of the system is represented by the red arrow. The boost done was  $0.25\hat{x}$ .

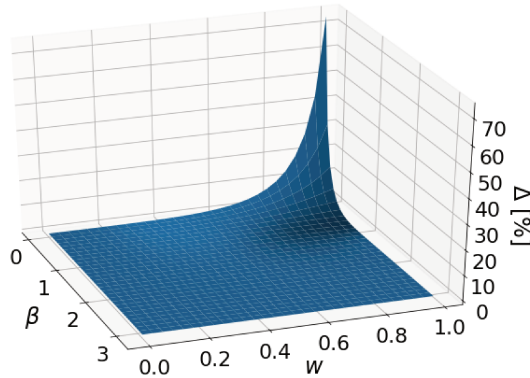


Figure 12 – Fraction of energy emitted  $\Delta$  for each case of (4.12) with  $\alpha_1 = \alpha_2$ ,  $w = w_1 = w_2$  and  $\beta$  the angle between  $\hat{n}_1$  and  $-\hat{n}_2$ .

the blob velocities in the direction of the collision are smaller and energy emission is less efficient.  $\Delta$  approaches zero as  $\beta$  approaches  $\pi$ , the parallel case with no collision, and the maximum of  $\Delta$  is for the axisymmetric case, when  $\beta = 0$ .

The conclusion about the equal mass case of generic BL-2 is that only the intensity of the blob velocities in the center of mass frame contributes to determine GW emission efficiency, what reinforces the idea that  $w_i$  controls the kinetic energy of the colliding BHs right before the merger in some sense. When  $q \neq 1$ , we will have a preferred direction of GW emission, this reference frame will be dynamical and other contributions may appear. A last important comment is that we can not assume  $\beta$  values different from  $\beta = 0$  or  $\beta = \pi$  to be the angle between BH velocities before the collision, since during the merging process the geometry of the system may change and, consequently, velocities of the blobs and initial BHs might not match their direction.

The general BL-2 initial condition (4.12) was already studied in previous works, but some of them have interpreted it as a non-head-on collision [26, 27, 28]. This

interpretation can only be wrong, since RT spacetimes can not describe any system with angular momentum in it. Our way of deriving (4.12) makes clear that it is just an ordinary axisymmetric case, but in a reference frame where the symmetry is not trivially recognized.

### 4.3 Collisions involving more BHs

Inspired by (4.12), we propose a new initial condition for the post-merger phase of a frontal collision involving more BHs. We do this just by adding new blobs to BL-2 and name it the BL- $n$  initial condition. The expression reads

$$Q(0, \theta, \phi) = \left( \sum_{i=1}^n \frac{\alpha_i}{S(w_i, \theta, \phi, \hat{\mathbf{n}}_i)} \right)^{-2}. \quad (4.13)$$

All  $-w_i \hat{\mathbf{n}}_i$  vectors also transform as ordinary velocities, and the asymmetry parameters between blobs are given by the fractions  $q_{ij} = \alpha_i / \alpha_j$ . It is important to state that (4.13) is constructed based on gluing  $n$  boosted Schwarzschild spacetimes, but this is done in a very specific way, in order to have some initial GW content and maintain the interpretation of blob velocities from BL-2. Because of that, we can only see this initial data as the post-merger phase of a collision of  $n$  BHs at the same instant of time, and no sequence of non-simultaneous collisions can be described by BL- $n$ .

Our first example is the equal masses BL-3 case ( $\alpha_1 = \alpha_2 = \alpha_3$ ), with Bondi mass aspect is illustrated in Figure 13 below. In the same way that generic BL-2 cases are



Figure 13 – Bondi mass aspect of a BL-3 initial condition with equal  $\alpha_i$  parameters and final velocities  $w'_1 = w'_2 = w'_3 = 0.7$ . The center of mass velocity in (a) is represented by the red arrow, with value of  $-0.35\hat{\mathbf{y}}$ .

just axisymmetric systems analyzed by different observers, the BL-3 initial condition will always be planesymmetric in its center of mass frame. This statement is true because it is always possible to find a Lorentz boost that sets three velocity vectors in the plane, *i. e.*, all head-on collisions which are not planesymmetric in any reference frame must have at least four BHs.

The condition for the general BL- $n$  initial data to do not present recoil is not so simple as in the binary case, since we can still have a preferred direction of GW emission even in the center of mass frame of a collision with only equal  $\alpha_i$  parameters. As stated in [section 3.3](#), we need planar reflection symmetry with respect to at least three planes, which intersection is given by just one point. It will happen if  $q_{ij} = 1$ ,  $w_i = w_j \forall i, j$  and the vectors  $\hat{\mathbf{n}}_i$  are disposed at the vertices of a regular polygon or polyhedron in the center of mass frame. Using [\(3.23\)](#), we can compute  $\Delta$  for all these analytically solvable cases, and the plot of  $\Delta$  calculations from two until twenty blobs follows in [Figure 14](#). The

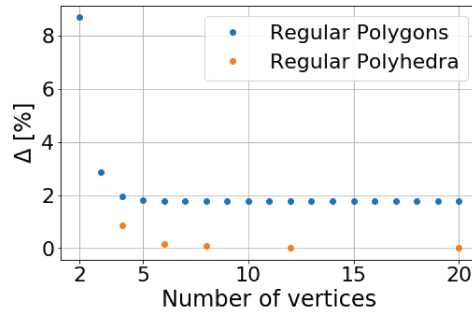
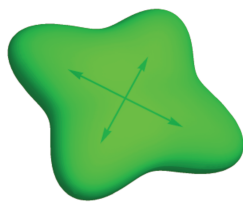


Figure 14 – Values of  $\Delta$  for some cases without recoil up to twenty blobs with all  $w_i = 0.8$  and equal  $\alpha_i$  parameters. The vectors  $\hat{\mathbf{n}}_i$  are disposed at the vertices of regular polygons or polyhedra.

degenerated case with two vertices is just the ordinary BL initial data seen in [section 4.1](#) and the polyhedra are the platonic solids: tetrahedron, octahedron, cube, icosahedron and dodecahedron respectively. To picture the situation, [Figure 15](#) follows with the Bondi mass aspect plots of the two BL-4 initial data present in [Figure 14](#). As the number of vertices



(a) BL-4 square



(b) BL-4 tetrahedron

Figure 15 – Bondi mass aspect of two BL-4 initial conditions with equal  $\alpha_i$  parameters and blob velocities  $w_1 = w_2 = w_3 = w_4 = 0.8$ . Black arrows represent the  $\hat{\mathbf{n}}_i$  vectors out of scale. In (a) the  $\hat{\mathbf{n}}_i$  vectors are disposed on the vertices of square, while in (b) they are aligned with the vertices of a tetrahedron.

of the polygons grows, the system gets rounder and curvature inhomogeneities diminishes, making the emission of GWs to be less efficient, and  $\Delta$  converges to the emission rate of some kind of “thick disk” BH collapsing into its own gravitational field. For the polyhedra, initial data is even closer to a sphere and  $\Delta$  is always smaller compared to the case of a

polygon with the same number of vertices. This fact is expected since  $\nabla_{\Omega}^2 K$  is the term that dictates the evolution of (2.15).

Another interesting family of  $Q(u_0, \theta, \phi)$  is the generalization of the octahedron, double pyramids with regular polygon basis. The simpler examples of these initial data are represented in Figure 16 below. Looking at the planes of symmetry in orange, we conclude

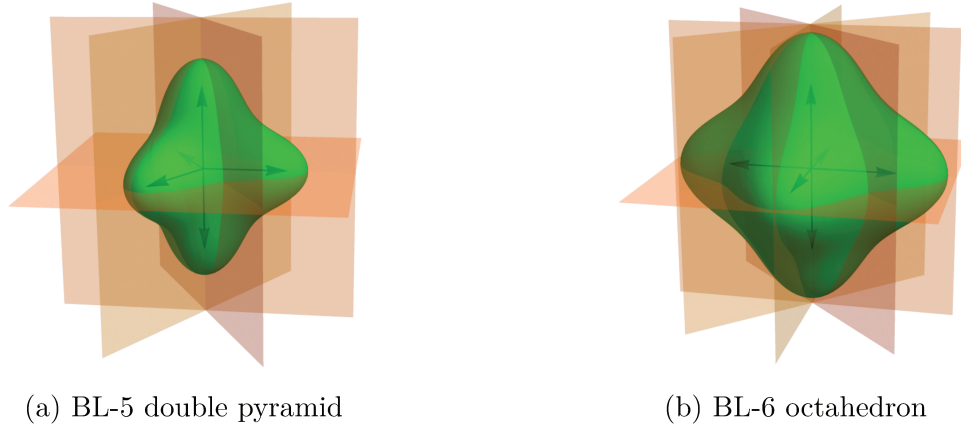


Figure 16 – Bondi mass aspect of two BL- $n$  double pyramid initial conditions with  $w_i = 0.8$  and equal  $\alpha_i$  parameters. Black arrows represent the  $\hat{\mathbf{n}}_i$  vectors out of scale. The planes of reflection associated with these initial conditions are represented in orange.

they do not present recoil when all  $q_{ij} = 1$  and blob velocities have the same module. Then, we compute (3.23) for all BL- $n$  double pyramids until thirty vertices and plot the results in Figure 17. The square is also a degenerated case of double pyramid, then it is represented

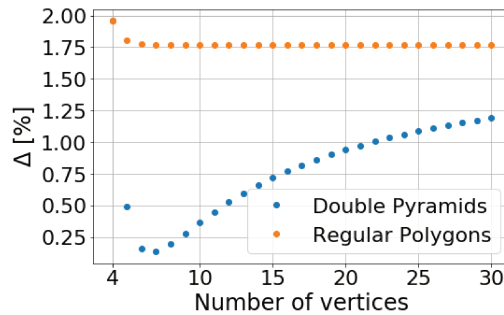


Figure 17 – Values of  $\Delta$  for all cases without recoil up to thirty blobs with all  $w_i = 0.8$  and equal  $\alpha_i$  parameters. The vectors  $\hat{\mathbf{n}}_i$  are disposed at the vertices of regular polygons or double pyramids.

in Figure 17 too. In comparison with regular polygons, double pyramids always have lower  $\Delta$ , since the two added BHs in the system help to get  $Q(u_0, \theta, \phi)$  rounder<sup>3</sup>. Also  $\Delta$  seems to be approaching some value, since there is an upper bound and it is increasing with  $n$ .

Again, all cases of (4.13) with any  $q_{ij} \neq 1$  can have non zero kick velocity, but some systems may not have enough symmetry even if all  $q_{ij} = 1$ , then they will present

<sup>3</sup> Notice the difference between  $M_B$  plots of Figure 15a and Figure 16b.

recoil as well. Examples follow in Figure 18. In Figure 18a the sum of the blob velocities

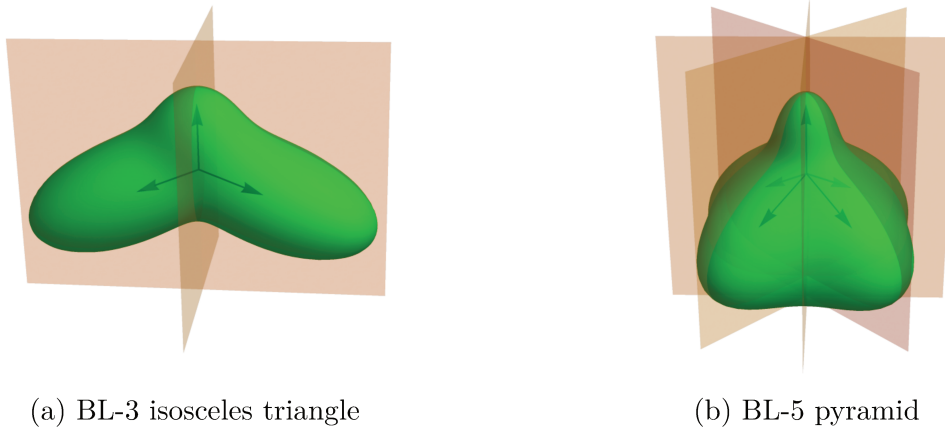


Figure 18 – Bondi mass aspect of two BL- $n$  initial conditions with equal  $\alpha_i$  parameters in the rest frame at  $u_0$ . Black arrows represent the  $\hat{\mathbf{n}}_i$  vectors out of scale. In (a) we have  $w_1 = 0.6$  and  $w_2 = w_3 = 0.8$ , while in (b)  $w_i = 0.8$  for all  $i$ . The planes of reflection associated with these initial conditions are represented in orange.

$-w_i \hat{\mathbf{n}}_i$  is zero, but the  $w_i$  parameters are different. In Figure 18b, even though the  $\hat{\mathbf{n}}_i$  vectors cancel out and all  $w_i$  parameter are equal, the source still presents recoil, as seen in section 5.4. These systems are not axisymmetric, but their momentum is restricted to only an axis, the one given by the intersection of the planes of reflection in orange. Also, Figure 18 let it explicit the reason why  $q_{ij}$  can not represent mass ratio of the isolated BHs before the collision, since these examples of initial data do not present enough symmetry to have the same GW emission rate for each blob, even when all  $q_{ij} = 1$ .

## 5 Numerical Results and Kick Velocity

In this chapter we solve the  $u$  evolution equations and extract quantitative physical information about the source during the emission process. To integrate equation (2.14), we use the spherical harmonics Galerkin decomposition developed in chapter 3 and the specific initial conditions derived in chapter 4. To determine properties of the source, we use  $Q(u \geq u_0, \theta, \phi)$  found in the evolution to calculate (2.22). A specific example is used to illustrate the problems around computing Bondi momentum  $u$  evolution. The programs developed were divided in three different categories, one to solve the axisymmetric case, other for planesymmetric initial data and another for a generic  $Q(u \geq u_0, \theta, \phi)$ . All programs were developed in python 3 and the source codes can be found at <https://github.com/pivaps/Robinson-Trautman>.

### 5.1 Strategies and uncertainties

There are two main algorithms for each one of the three categories of initial conditions. Since all programs are extensive, it would be difficult to explain all their details in this work, then we will briefly discuss the main ideas used to develop them and their contributions for numerical errors.

The first goal is to determine the ODE system (3.5). To do this, we write the expansion (3.1) with an algebraic manipulation software<sup>1</sup>, compute all integrals involved and store the final results on a text file. This is direct for the axisymmetric case, in which we actually use the simpler expression (3.20), but for the other cases it is important to remember all considerations pointed in chapter 3, mainly the ones about the expansions (3.6), (3.7) and selection rules in Appendix B. The choice of  $N$  (order of spherical harmonics expansion) will dictate how good is the approximation of  $Q(u_0, \theta, \phi)$  by (3.1), and this will set the main contribution to uncertainties in all calculations. Then, the best way to estimate the error is with direct comparison between computations done with an initial data evolved using order  $N$  and lower order expansions.

To get the  $u$  evolution, we need to compute the initial modal coefficients, given by

$$b_m^l(u_0) = \frac{2l+1}{4\pi} \langle Y_l^m, Q(u_0) \rangle = \frac{2l+1}{4\pi} \oint_{S^2} \bar{Y}_l^m(\theta, \phi) Q(u_0, \theta, \phi) dS \quad (5.1)$$

and evolve them with the ODE system determined in the previous stage. In the axisymmetric case, all  $\phi$  integrals will be trivial and both tasks can be done with precise standard

<sup>1</sup> We used sympy python library for this task.

integration methods<sup>2</sup>. The planesymmetric and generic cases demand to perform two dimensional integrals to compute (5.1), so we need to be careful with the choice of sampling points on the sphere in order to get enough precision. We will always use a method based on the Fibonacci sequence to generate a good sample. This strategy was developed in [45] and the final integration formula reads

$$\oint_{S^2} f(\theta, \phi) dS = \int_{-1}^1 \int_0^{2\pi} f(s = \cos \theta, \phi) d\phi ds \approx \pi \Delta s \sum_{j=0}^F [1 + \cos(\pi s_j)] \times \left[ f\left(\frac{\pi j F'}{F}, s_j + \frac{\sin(\pi s_j)}{\pi}\right) + f\left(\pi + \frac{\pi j F'}{F}, s_j + \frac{\sin(\pi s_j)}{\pi}\right) \right], \quad (5.2)$$

where  $F'$  and  $F$  are consecutive Fibonacci numbers,  $\Delta s = 2/F$  and  $s_j = -1 + j\Delta s$ . With a high value of  $F$ <sup>3</sup>, all errors will be too small compared to the ones involved on the choice of the expansion order  $N$  for (3.1). Actually, we have already used (5.2) in order to compute all integrals involved in (2.22) calculations to plot Figure 14 and Figure 17 in section 4.3.

Determined  $Q(u \geq u_0, \theta, \phi)$ , there are two main ways to control numerical uncertainty: to use the known constant of motion (2.16), or the expression for the stationary solution. With (2.17) and the expansion (3.1), it is easy to show that

$$\begin{aligned} [b_0^0(\infty)]^2 - [b_0^1(\infty)]^2 - 2|b_1^1(\infty)|^2 &= 1; \\ b_m^l(\infty) &= 0, \text{ if } l \geq 2 \end{aligned} \quad (5.3)$$

and the deviations from the expressions in (5.3) can also be used as numerical error control. For actual calculations we will only present the uncertainty associated with the first expression in (5.3), since the absolute value of the  $l \geq 2$  coefficients is typically way smaller than other deviations at  $u \rightarrow \infty$ .

As a first attempt to probe precision of the algorithms, we compute the  $u$  evolution of a BL-2 axisymmetric initial data given by

$$Q(0, \theta) = \left( \frac{q}{\sqrt{\gamma(1 + w \cos \theta)}} + \frac{1}{\sqrt{\gamma(1 - w \cos \theta)}} \right)^{-2} \quad (5.4)$$

with  $q = 1$  and  $w = 0.5$ , which represents the post merger phase of a binary collision of BHs. All results are presented in Table 2. Here, we solved the evolution ODE system with the axisymmetric program and determined all the uncertainty control parameters. We also used (3.24) to compute  $\Delta$  analytically, since the system has symmetry of reflection with respect to  $z = 0$ , finding  $\Delta = 0.006482436(44 \pm 5)$ <sup>4</sup>, which makes possible to calculate

<sup>2</sup> We used numpy and scipy python library integration routines to calculate all one dimensional integrals and also to solve all ODE systems.

<sup>3</sup> We used  $F = 23$  for any integration on the sphere in this work, which means 28657 evaluation points.

<sup>4</sup> This notation shows in a compact way the error bar in the last decimal places written. We will adopt this notation from now on.

Table 2 – Determination of  $\Delta$  and error estimations for the  $u$  evolution from  $u_0 = 0$  to  $u = (24m_0)^{-1}$  of (5.4) initial data with  $q = 1$ ,  $w = 0.5$  and 2000 integration steps with the axisymmetric algorithms.

$N$	$ (q_0/2\pi) - 2 $	$(b^0)^2 - (b^1)^2 - 1$	$\Delta$	$v_k$
2	$4 \times 10^{-4}$	$2 \times 10^{-4}$	$0.006(40 \pm 9)$	0
3	$4 \times 10^{-4}$	$2 \times 10^{-4}$	$0.006(40 \pm 9)$	$7 \times 10^{-17}$
5	$4 \times 10^{-6}$	$2 \times 10^{-6}$	$0.00648(1 \pm 1)$	$2 \times 10^{-15}$
7	$2 \times 10^{-7}$	$1 \times 10^{-7}$	$0.0064824(9 \pm 6)$	$3 \times 10^{-13}$
9	$8 \times 10^{-8}$	$4 \times 10^{-8}$	$0.0064824(2 \pm 2)$	$9 \times 10^{-14}$
10	$2 \times 10^{-8}$	$1 \times 10^{-8}$	$0.0064824(30 \pm 6)$	$2 \times 10^{-19}$

the full numerical error associated with  $\Delta$  in Table 2 as the absolute difference with the analytical value. We know that kick velocity is zero for this case with  $q = 1$ , then the calculated values of  $v_k = |\mathbf{v}_k|$  from the codes can also be used as a last uncertainty parameter.

We can not directly compute error contributions associated with the choice of  $N$  in  $Q_N(u, \theta, \phi)$ , but it is possible to illustrate the convergence of the expansion in this example with Figure 20, a plot of  $b^l(u \geq u_0)$  for (5.4) with  $N = 10$ . In Figure 20 we

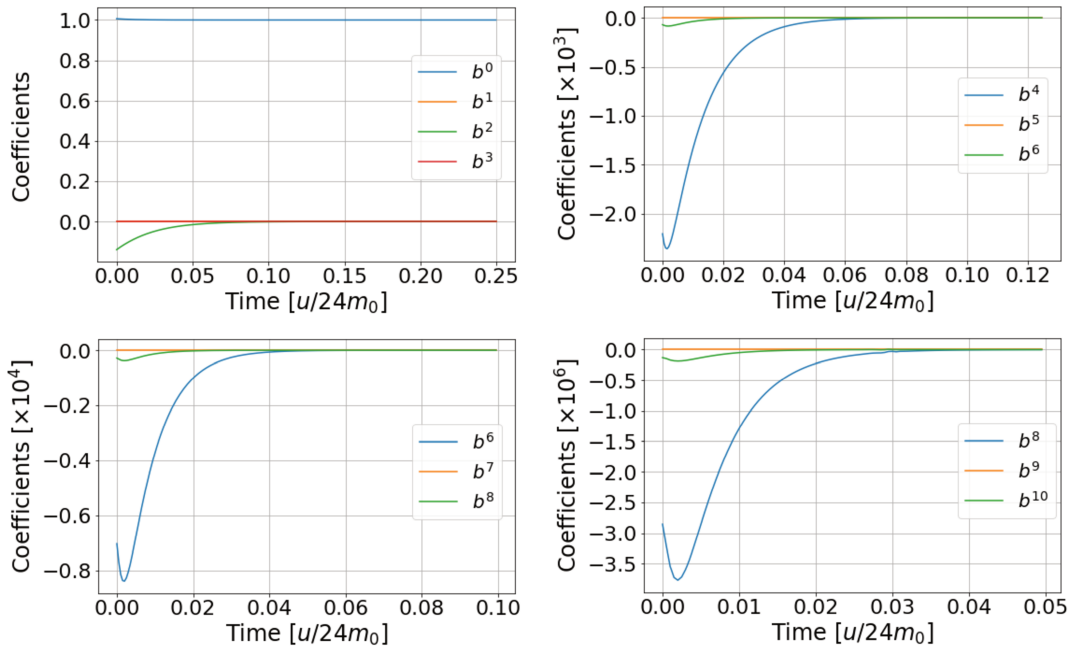


Figure 19 – Modal coefficients of the  $u$  evolution for (5.4) initial data with  $q = 1$ ,  $w = 0.5$ . The axisymmetric algorithm with  $N = 10$  was used with 2000 integration steps.

can see that  $Q_N(u \geq u_0, \theta)$  has symmetry of reflection with respect to  $z = 0$ , as expected, since all odd  $b^l$  are null throughout the evolution and, because of that, computing an odd  $N$  order is almost the same as computing  $N - 1$ . This is the explanation for lines  $N = 2$

and  $N = 3$  to be almost equal in Table 2. Since we are satisfied with precision acquired with  $N = 10$ , we will only use this order to evolve axisymmetric initial data from now on.

Using now  $q = w = 0.5$ , we solve (5.4) as the first non analytical case in this work. The uncertainty control parameters take values in the same order of magnitude as in Table 2 and the fraction of energy emitted and kick velocity for  $N = 10$  are  $\Delta = 0.004788(308 \pm 9)$  and  $v_k = 0.000464557(11 \pm 3)$ , with error estimation based on absolute deviations from  $N = 9$  calculations, since we do not have an analytical value to compare when  $q \neq 1$ . Here  $\Delta$  is lower than in the case of  $q = 1$  because mass asymmetry indicates that one of the blobs may have less energy to contribute to the process. Also,  $\mathbf{v}_k = -v_k \hat{\mathbf{z}}$  points to the direction where  $M_B$  is rounder in the center of mass frame<sup>5</sup>, opposite to the side of higher intensity of GW emission. The modal coefficients evolution plot follows in Figure 20. In this case all  $b^l$  are non-zero since there is no additional

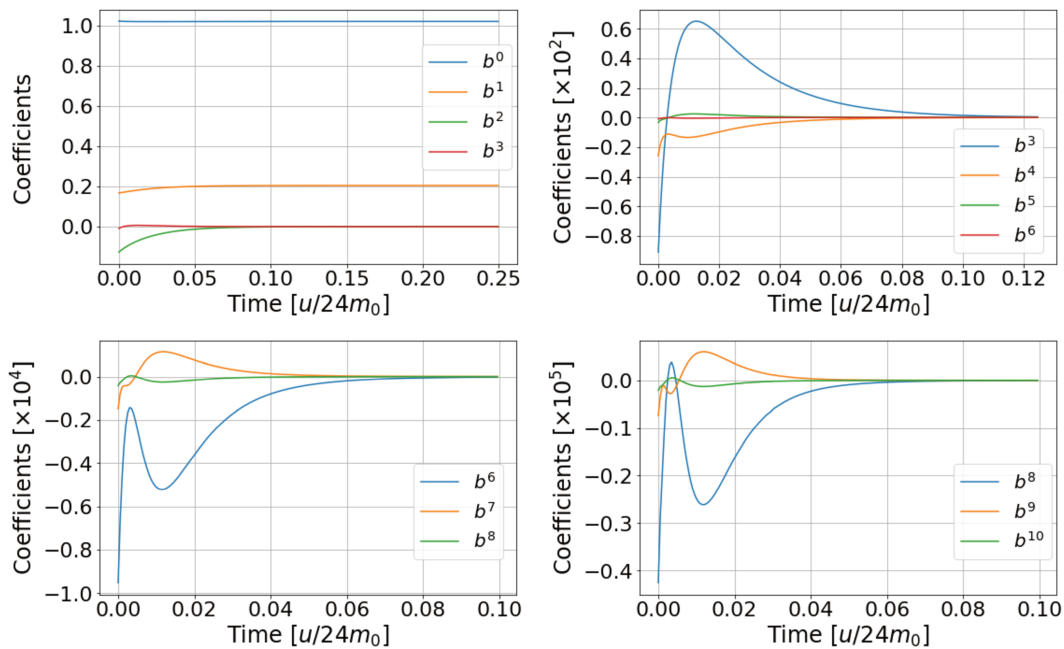


Figure 20 – Modal coefficients of the  $u$  evolution for (5.4) initial data with  $q = w = 0.5$ . The axisymmetric algorithm with  $N = 10$  was used with 2000 integration steps.

symmetry in the system.

To quantify uncertainty for the planesymmetric programs, we could also compute comparisons with an analytical solution, but we will use the previous calculations for (5.4) as reference. The most interesting way of doing it is to solve an axisymmetric initial data rotated by some angle with respect to the  $y$  axis. Initial data (5.4) rotated by  $\pi/2$  is

<sup>5</sup> See Figure 10b to get better geometric intuition about curvature inhomogeneities involved.

given by

$$Q(0, \theta) = \left( \frac{q}{\sqrt{\gamma(1 + w \cos \phi \sin \theta)}} + \frac{1}{\sqrt{1 - w \cos \phi \sin \theta}} \right)^{-2}. \quad (5.5)$$

Now we use (5.5) to compute values of  $\Delta$  and  $v_k$  for  $q = w = 0.5$  with the planesymmetric algorithms and compare them with previous results of axisymmetric programs with  $N = 10$ . Table 3 follows with all information and uncertainty parameters. Calculations for orders

Table 3 – Determination of  $\Delta$ ,  $v_k$  and error estimation for the  $u$  evolution from  $u_0 = 0$  to  $u = (24m_0)^{-1}$  of (5.5) initial data with  $q = 1$ ,  $w = 0.5$  and 2000 integration steps with the planesymmetric algorithms.

$N$	$ (q_0/\pi) - 4 $	$(b_0^0)^2 - (b_1^0)^2 - 2(b_1^1)^2 - 1$	$\Delta$	$v_k$
2	$5 \times 10^{-3}$	$1 \times 10^{-3}$	0.00(51 $\pm$ 3)	0.00(42 $\pm$ 4)
3	$1 \times 10^{-3}$	$3 \times 10^{-4}$	0.004(84 $\pm$ 6)	0.000(5 $\pm$ 1)
4	$8 \times 10^{-5}$	$2 \times 10^{-5}$	0.0047(95 $\pm$ 7)	0.000(3 $\pm$ 1)
5	$3 \times 10^{-5}$	$9 \times 10^{-6}$	0.00478(6 $\pm$ 2)	0.0004(5 $\pm$ 1)
6	$6 \times 10^{-6}$	$2 \times 10^{-6}$	0.00478(7 $\pm$ 1)	0.00046(5 $\pm$ 1)
7	$1 \times 10^{-6}$	$3 \times 10^{-6}$	0.00478(7 $\pm$ 1)	0.000464(6 $\pm$ 1)

higher than seven take too much computational time and we are also satisfied with precision achieved in Table 3, then we will set  $N = 7$  for all numerical computations with planesymmetric programs. A plot of modal coefficients evolution for the first four orders is presented in Figure 21 below. Since initial data (5.5) has reflection symmetry with respect

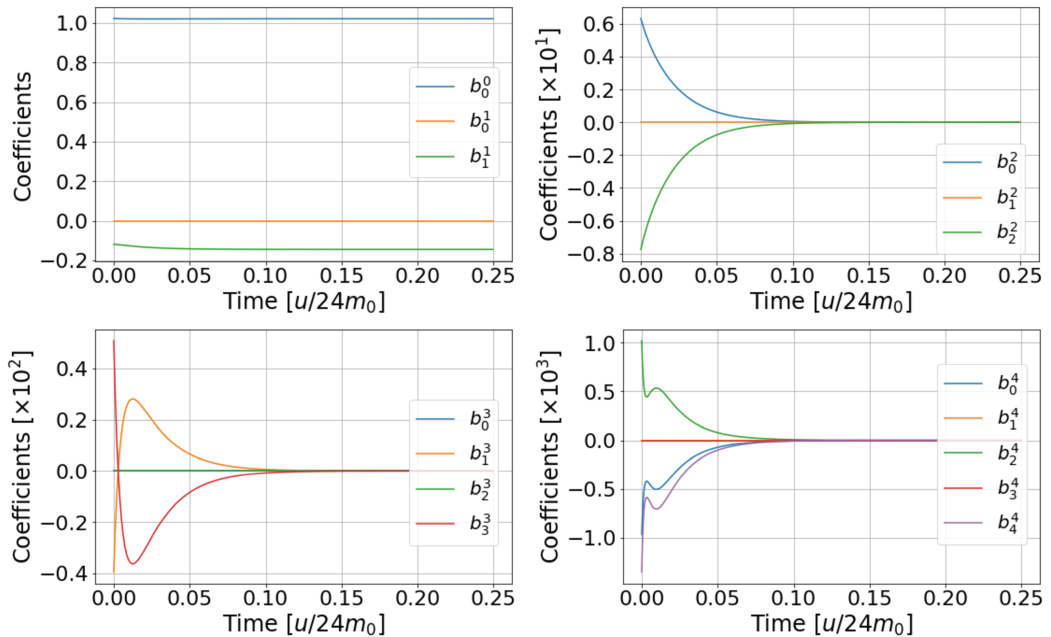


Figure 21 – First modal coefficients of the  $u$  evolution for (5.5) initial data with  $q = 1$ ,  $w = 0.5$ . The planesymmetric algorithm with  $N = 7$  was used with 2000 integration steps.

to  $z = 0$ , only  $b_m^l(u)$  with even  $l + m$  are not null.

Algorithms for generic  $Q(u_0, \theta, \phi)$  evolution were built with the same structure used in planesymmetric ones, but all modal coefficients may be complex and it demands approximately twice computational time in comparison with planesymmetric codes. Because we will only investigate systems with at least one plane of reflection for initial data, we will not use them in this work and computations will always be done with the simplest program available. Also, uncertainties about physical computations will not be discussed from now on, since all programs are considerably precise for high order in the modal expansion.

Just for the sake of completeness we choose an initial condition to compare the planesymmetric and generic algorithms. We solve the BL-4 regular tetrahedron<sup>6</sup> with  $\alpha_2 = \alpha_3 = \alpha_4 = 2\alpha_1$ ,  $\hat{\mathbf{n}}_1 = \hat{\mathbf{z}}$  and  $w_i = 0.5$  using both programs for order  $N = 7$ . Then we get  $\Delta = 0.000361(7 \pm 4)$  and  $\mathbf{v}_k = -0.000053(2 \pm 2)\hat{\mathbf{z}}$ . The uncertainty was estimated with the absolute difference between results, and a rotation of  $\pi/2$  with respect to the  $z$  axis was performed in the planesymmetric initial data to be evolved by the generic algorithm.

## 5.2 About Bondi momentum evolution

Our goal in this section is to use the axisymmetric algorithms developed in this work, in order to help us to understand the difficulties involved in the process of computing momentum evolution for RT spacetimes. Momentum rate of change is given by (2.21) and, because we do not know how to solve the second term of it, we will assume it is zero and see the consequences of our act. This simplification turns (2.21) into an uncoupled ODE system with direct solution, which reads

$$P^\mu(u) = P^\mu(u_0) + \int_{u_0}^u \frac{dP^\mu(u')}{du'} du'. \quad (5.6)$$

Using the Bondi frame where  $P^\mu(u_0)$  is given by (2.8), we get the energy and momentum evolution for initial data (5.4) with  $q = 0.5$  and  $w = 0.5$ . They are represented by the orange curves in Figure 22 below. Just by looking at these curves we can not notice anything wrong, but the final momentum and velocity do not match with direct numerical computations using just the expressions (3.22). Then, we perform a supertranslation in order to fix it, getting to the green curves. In our case, a supertranslation is just a shift in the graph because momentum time derivative in (5.6) is computed only using  $Q(u \geq u_0, \theta, \phi)$ , without any frame dependence, *i. e.*, since only the initial momentum expression changes in (5.6), we just add an offset constant term to the graph. This gives a different initial Bondi momentum  $P^\mu(u_0)$  to compare with the stationary solution. This means that one of the following sentences is true: either we can not compute Bondi momentum with (2.8) at  $u_0$ , or (5.6) is not the proper momentum evolution. For the

<sup>6</sup> See Figure 15b.

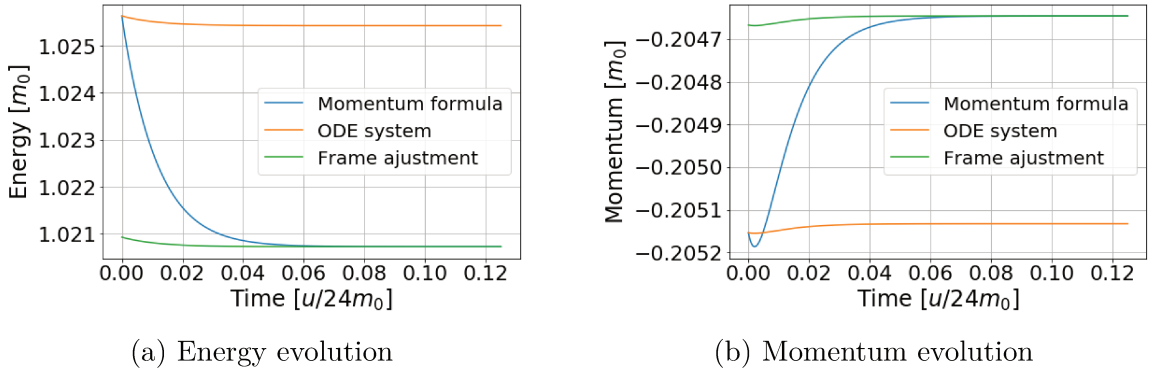


Figure 22 – Bondi energy and momentum  $u$  evolution for (5.4) initial data with  $q = w = 0.5$  and 250 integration steps from  $u_0 = 0$  until  $u = 0.125/24m_0$ . The orange and green curves are the solutions of (5.6) for (5.4) in different Bondi frames of reference. The blue curves were built with direct calculation of Bondi momentum with the formula (2.8).

sake of comparison we also plot a couple of blue curves, representing direct momentum calculations with (2.8) formula for each  $u \geq u_0$ .

To let it clear where the problem is, we perform a boost in (5.4) initial data in order to stop the system<sup>7</sup>. Then, we evolve the stopped system  $Q'(u \geq u_0, \theta)$  and compute the same graphs for Bondi momentum evolution in Figure 23 as done before. A big contradiction turns to be evident: the evolved quantities can not be compatible

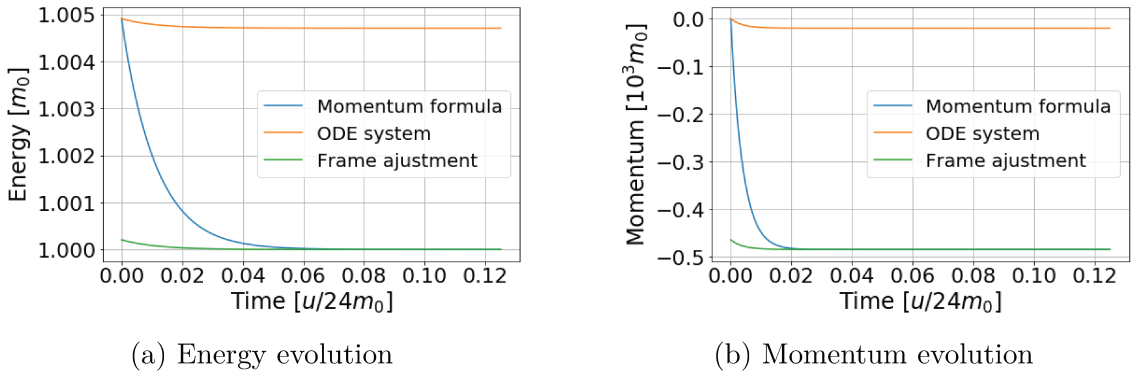


Figure 23 – Bondi energy and momentum  $u$  evolution for stopped (5.4) initial data with  $q = w = 0.5$  and 250 integration steps from  $u_0 = 0$  until  $u = 0.125/24m_0$ . The orange and green curves are the solutions of (5.6) for (5.4) in different Bondi frames of reference. The blue curves were built with direct calculation of Bondi momentum with the formula (2.8).

with both final Schwarzschild momentum and the initial null velocity. This means that we indeed need the second term in (2.21) in order to evolve Bondi momentum for a general initial data  $Q(u, \theta, \phi)$ , *i. e.*, the notion of asymptotic frame  $j^\mu$  presented in section 1.3 changes significantly during the emission process. The reader may notice that even the

<sup>7</sup> See the end of section 2.1 for the stopping procedure.

blue curves are wrong and they are presented just for the sake of comparison, since (2.8) is only valid at  $u = u_0$  and  $u \rightarrow \infty$ .

The mistake of computing momentum evolution by the wrong methods led numerical results into misleading interpretations in some works before. In [27, 26, 28], the general BL-2 case (4.12) has been associated with a non-head-on collision, an initial condition impossible to be analyzed with RT spacetimes because of the presence of angular momentum. To avoid making any false assumption, we are satisfied with (2.22) calculations in this work. A complete discussion about Bondi momentum change for finite time distances is presented in [36].

### 5.3 Kick velocity

If RT initial data does not have enough symmetry in its center of mass frame, the source has a preferred direction of GW emission, leading to recoil felt by the source. Since analytical results are not available for any of these cases, we will investigate recoil properties with numerical calculations of kick velocity ( $\mathbf{v}_k$ ), defined in (2.22). In Figure 24, we compute  $\mathbf{v}_k = -v_k \hat{\mathbf{z}}$  and  $\Delta$  for BL-2 using (5.4) initial data stopped at  $u_0 = 0$ . When

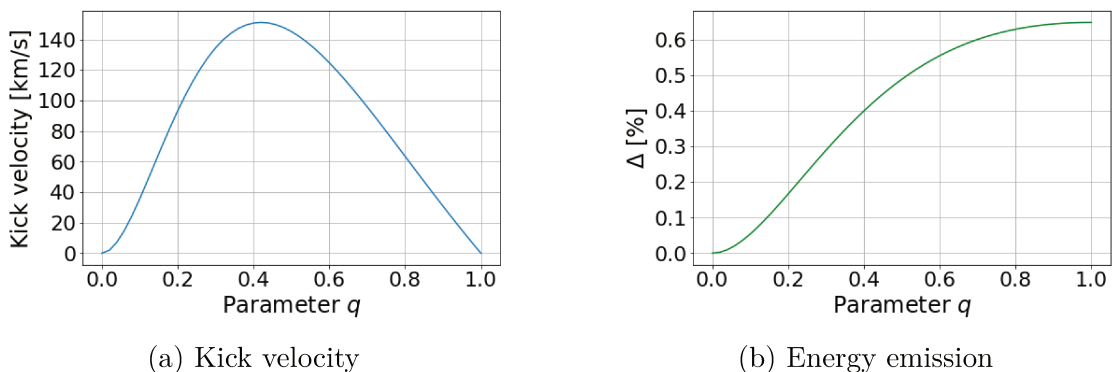


Figure 24 – Numerical calculations of  $\Delta$  and  $v_k$  for (5.4) initial data with  $w = 0.5$  for 50 values of  $q$ . The evolution was done with 2000 integration steps from  $u_0 = 0$  until  $u = (24m_0)^{-1}$ .

$q = 0$  we just have the stationary solution from the beginning of evolution, then  $v_k$  and  $\Delta$  are both null. For  $q = 1$  we have the equal mass collision case, there is no kick and  $\Delta$  has its highest value. Between  $q = 0$  and  $q = 1$  recoil is present, the maximum of  $v_k$  is at  $q = 0.4(2 \pm 2)$  and  $\Delta$  strictly increases.

To understand  $v_k$  in all different reference frames, we perform Lorentz boosts in all physical quantities computed and plot it in Figure 25 below. Observers in other Lorentz frames always see a lower kick because of the transformation rules applied to initial and final velocities of the source. Kick velocity never changes its sign<sup>8</sup>, but it goes

<sup>8</sup> Here the recoil is always of “antikick” type, since the smaller blob velocity is aligned with  $\mathbf{v}_k$ . We remember the reader that the “antikick” phenomenon is defined and explained in section 2.3.

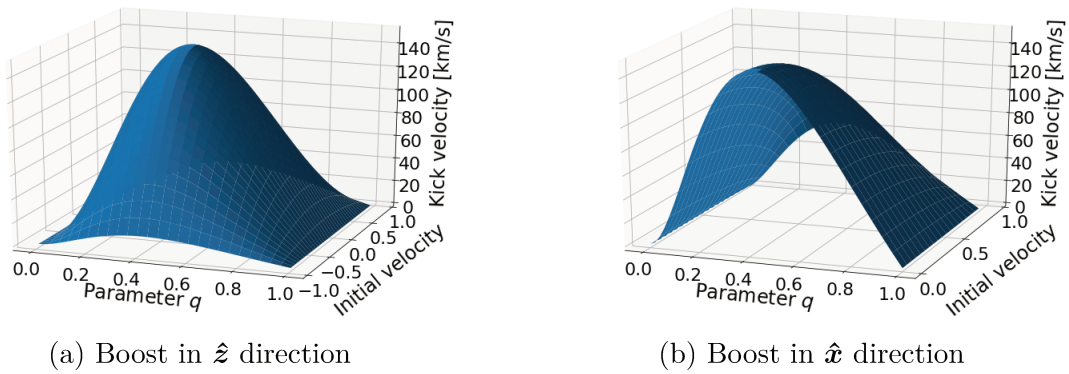


Figure 25 – Kick velocity values for results in Figure 24a boosted in the direction of the axis of symmetry (a) and in a perpendicular direction (b).

to zero when the system is boosted with arbitrarily high velocities in the direction of the symmetry axis.  $\Delta$  does not change for any boost in Figure 25b, but it is slightly altered by boosts in Figure 25a, mainly in the region near  $q = 1$ . All  $v_k$  associated with any BL-2 general initial condition (4.12) are represented by one of the points in Figure 25, then the binary case is fully solved here and, joining results with the ones in section 4.1, we conclude that emission is more efficient for higher blob velocities in the center of mass frame and for asymmetry parameter  $q$  closer to unity.

Adding one blob, we can study the BL-3 initial data for  $w_i \hat{n}_i$  vectors disposed at the vertices of an equilateral triangle. We choose the case where  $\alpha_1 = q\alpha_2 = q\alpha_3$  and  $\hat{n}_1 = \hat{z}$ , that follows in Figure 26. The kick velocity  $\mathbf{v}_k = -v_k \hat{z}$  is qualitatively the same,

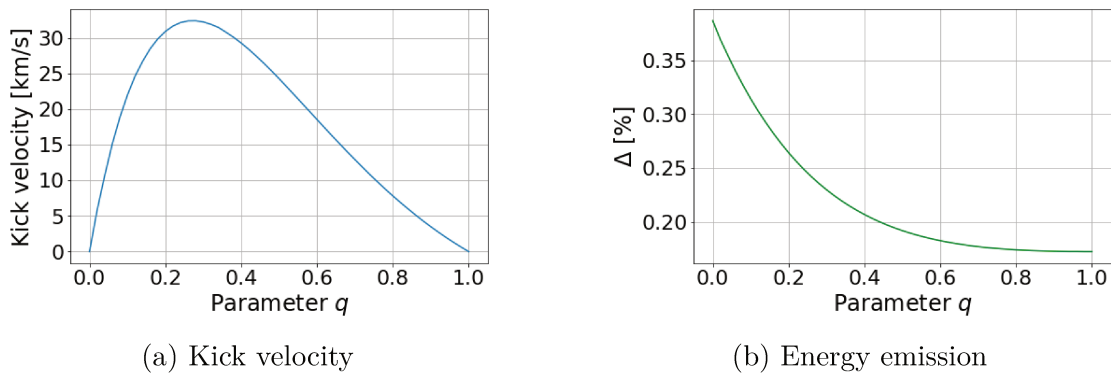


Figure 26 – Numerical calculations of  $\Delta$  and  $v_k$  for BL-3 equilateral triangle initial data with all  $w_i = 0.5$  for 50 values of  $q$ . The evolution was done with 2000 integration steps from  $u_0 = 0$  until  $u = (24m_0)^{-1}$ .

but with maximum at  $q = 0.2(8 \pm 2)$ , since the geometry has changed. Also, the amount of kick is lower because emission is less directed and less efficient in this system. As discussed in section 4.3, if initial data has less curvature inhomogeneities,  $\Delta$  will be smaller, which is illustrated by Figure 26b since  $\Delta$  is maximum at  $q = 0$ , the BL-2 initial condition. In this case we also have the effect of “antikick” too, since the smaller blob velocity is

directed at  $-\hat{z}$ , the same direction as the change in velocity. Then, we should see the system decelerating after merger in such situation.

Figure 27 shows results of Figure 26a boosted in two different directions. All

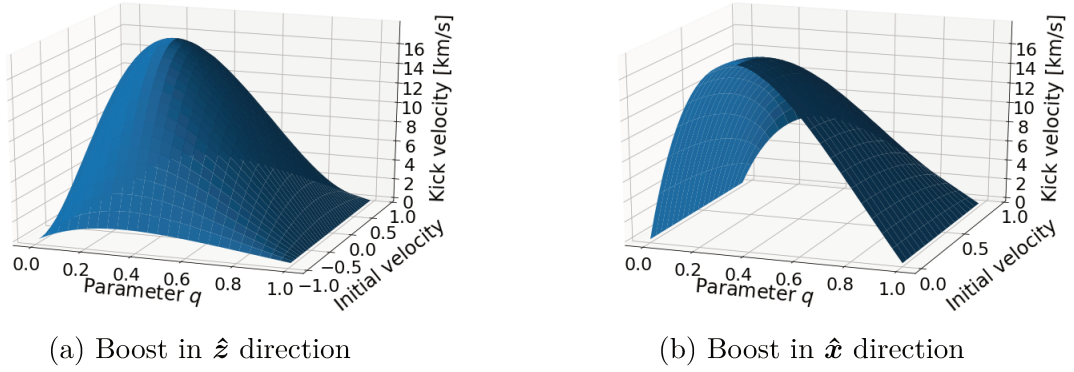


Figure 27 – Kick velocity values for results in Figure 26a boosted in the direction of the axis contained by the planes of symmetry (a) and in a normal direction (b).

previous considerations about  $v_k$  and  $\Delta$  due to frame changing are true again, but this time the graph does not contemplate all range of possible parameters for blob velocities  $w_i$  of this initial condition and more scenarios are needed to be considered, but we are not worried in fully solving BL-3 here.

Another interesting case to investigate is BL-4 initial data with  $\alpha_1 = q\alpha_2 = q\alpha_3 = q\alpha_4$  and all  $w_i = 0.5$ . To fix the other parameters, let us take  $\hat{n}_i$  vectors disposed at the vertices of a tetrahedron with  $\hat{n}_1 = \hat{z}$ . Values of  $\mathbf{v}_k = -v_k\hat{z}$  and  $\Delta$  for this system follow in Figure 28. Maximum  $v_k$  is at  $q = 0.3(4 \pm 2)$  and now the kick is even smaller

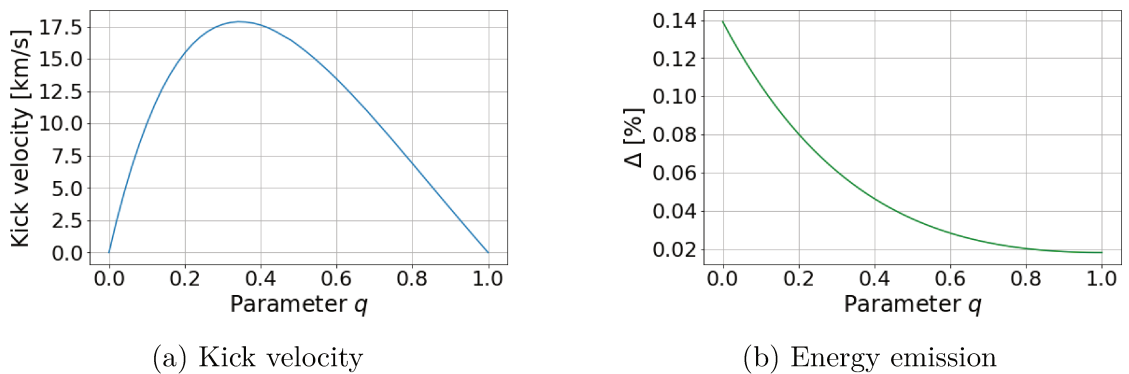


Figure 28 – Numerical calculations of  $\Delta$  and  $v_k$  for BL-4 tetrahedron initial data with blob velocities  $w_i = 0.5$  for 50 values of  $q$ . The evolution was done with 2000 integration steps from  $u_0 = 0$  until  $u = (24m_0)^{-1}$ .

because another blob is involved, the emission is, once again, less directed and  $\Delta$  is lower. Since  $v_k$  is parallel with the velocity of the less massive blob, this system also suffers an “antikick”.

Trying to understand the role of blob velocities in the kick, we build initial data based on the case illustrated in Figure 18a. We take BL-3 with  $\alpha_1 = q\alpha_2 = q\alpha_3$ ,  $w_1 = 0.5$ ,  $w_2 = w_3 = 0.4$ ,  $\hat{\mathbf{n}}_1 = \hat{\mathbf{z}}$  and demand that blob velocities cancel out. In this case we find  $\mathbf{v}_k = -v_k\hat{\mathbf{z}}$  and  $\Delta$  values plotted in Figure 29. Here, we used different blob velocity

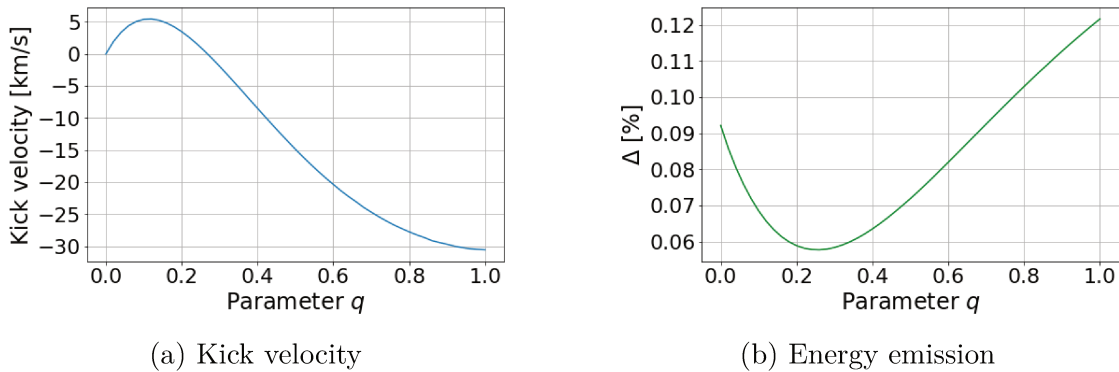


Figure 29 – Numerical calculations of  $\Delta$  and  $v_k$  for a BL-3 initial data with  $w_1 = 0.5$ ,  $w_2 = w_3 = 0.4$  and 50 values of  $q$ . The evolution was done with 2000 integration steps from  $u_0 = 0$  until  $u = (24m_0)^{-1}$ .

intensities in order to build a system with changing sign  $v_k$  and we found some cases without “antikick”. Recoil is not of “antikick” type for values higher than  $q = 0.2(6 \pm 2)$ , the case for which  $v_k$  is zero. For free, we also get an example with non monotonic  $\Delta$ , with minimum at the same value of  $q$  for null recoil. The maximum of  $\Delta$  is at  $q = 1$  in this case, since the blob associated with  $\hat{\mathbf{n}}_1$  has a considerably higher blob velocity ( $w_1 > w_2 = w_3$ ), adding more kinetic energy to the initial condition and, consequently, to the amount of energy emitted through GWs.

Then we see a pattern, when a system does not present recoil and we start shrinking one of its blobs, emission is more efficient in the direction of this smaller blob and the source suffers an “antikick”. Guided by our geometric intuition, we conjecture this as true. We call the attention of the reader to the hypothesis of shrinking only one blob for this to be true, since we can also show an example of sign change in  $v_k$  shrinking two blobs at the same time, and the rule will not be applied. As an example, we choose  $q\alpha_1 = \alpha_2 = \alpha_3$  and all  $w_i = 0.5$  for the BL-3 equilateral triangle with  $\hat{\mathbf{n}}_1 = \hat{\mathbf{z}}$ . The values of  $\mathbf{v}_k = v_k\hat{\mathbf{z}}$  and  $\Delta$  follow in Figure 30. Now we shrank both blobs related to  $\hat{\mathbf{n}}_2$  and  $\hat{\mathbf{n}}_3$  with the same  $q$  parameter and two effects competed with each other to determine the direction of recoil. For values higher than  $q = 0.4(3 \pm 1)$ , the direction of  $\mathbf{v}_k$  is opposite to the blob velocity vector of the bigger blob, then it is “antikick” type, the same as for the case of only one smaller blob. But, if the shrinking blobs get too small, the stopping boost demands too big intensity, and they will acquire a very high initial velocity in the center of mass frame. Because of this great kinetic energy compared with the bigger blob, the Bondi mass distribution is closer to the case with only one less massive blob, the kick inverts and  $v_k$  changes its sign. The highest value of  $\Delta$  and  $v_k$  with “antikick” is in the case

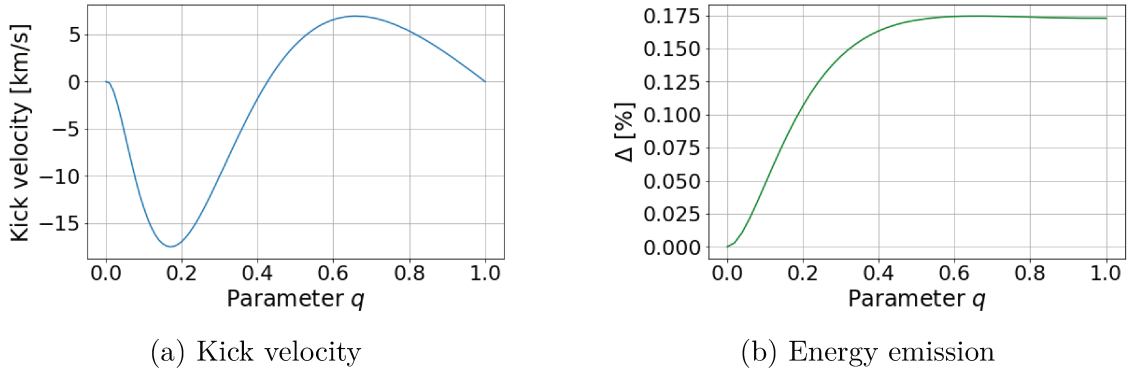


Figure 30 – Numerical calculations of  $\Delta$  and  $v_k$  for a BL-3 equilateral triangle initial data with blob velocities  $w_i = 0.5$  for 100 values of  $q$ . The evolution was done with 2000 integration steps from  $u_0 = 0$  until  $u = (24m_0)^{-1}$ .

$q = 0.6(6 \pm 1)$ , while for the other regime the maximum recoil intensity is at  $q = 0.1(7 \pm 1)$ .

We end this section stating that kick velocity is directly connected with inhomogeneities in the geometry of initial data to be evolved [44], then asymmetries in  $M_B$  angular distribution in the center of mass frame can be used as a qualitative guide to predict when and to which direction will a system present recoil.

## 5.4 BL- $n$ Pyramids

An interesting fact about BL- $n$  initial conditions is that these systems may present new physical properties as we add more blobs to it. For example, recoil is always “antikick” type for BL-2, but adding just one blob we can produce different kinds of kick. Also, in the center of mass frame, the BL-2 case is always axisymmetric, BL-3 may be planesymmetric and BL-4 might have no symmetry at all. Adding one more blob to BL-4 also gives us a new feature, but to see it we need to look at a specific family of initial data, the BL- $n$  pyramids, which are illustrated below with two examples in Figure 31. To build



Figure 31 – Bondi mass aspect of two BL- $n$  pyramid cases with  $w_i = 0.8$  and equal  $\alpha_i$  parameters. Black arrows represent the  $\hat{n}_i$  vectors out of scale and planes of reflection in (b) are represented in orange.

a BL- $n$  pyramid we just need a regular BL- $(n - 1)$  polygon with  $\hat{\mathbf{n}}_i$  vectors in the  $z = 0$  plane, and then we add a new blob with velocity in the direction of  $\hat{\mathbf{z}}$ , which can be seen as an apex of a regular basis pyramid.

The new feature of those systems is that we can have an example with all  $q_{ij} = 1$ , equal blob velocity intensities ( $w_i = w_j \forall i, j$ ),  $\hat{\mathbf{n}}_i$  vectors summing up to zero and still get recoil. The tetrahedron itself (Figure 31a) is a triangular based pyramid, but it is also a regular polyhedron and does not present recoil. The simplest case that fulfills all requirements above and also has  $v_k \neq 0$  is the BL-5 pyramid, represented in Figure 31b. As done in section 5.3, we choose  $\alpha_1 = q\alpha_2 = q\alpha_3 = q\alpha_4 = q\alpha_5$ , set  $\hat{\mathbf{n}}_1 = \hat{\mathbf{z}}$  as the apex and solve Figure 18b initial data with all  $w_i = 0.5$ . Values for  $\mathbf{v}_k = -v_k\hat{\mathbf{z}}$  and  $\Delta$  follow in Figure 32. When  $q = 0$  we just have the ordinary BL-4 square, then  $v_k = 0$  and GW

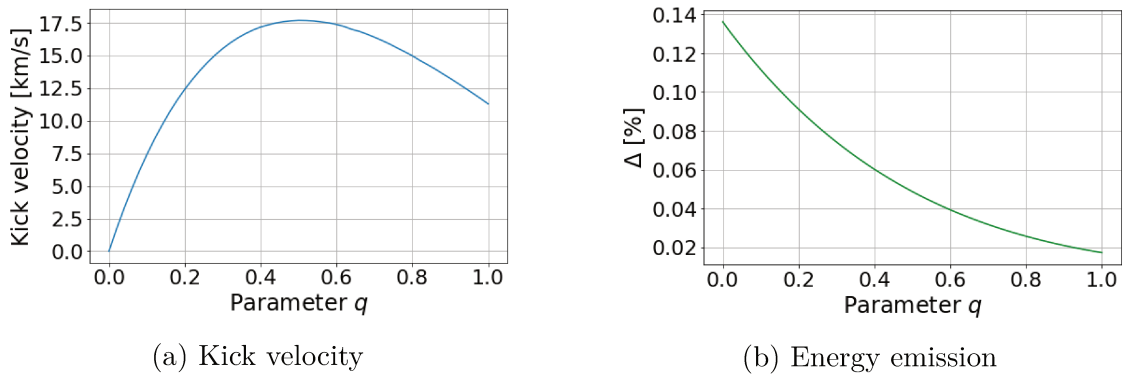


Figure 32 – Numerical calculations of  $\Delta$  and  $v_k$  for BL-5 pyramid initial data with blob velocities  $w_i = 0.5$  for 50 values of  $q$ . The evolution was done with 2000 integration steps from  $u_0 = 0$  until  $u = (24m_0)^{-1}$ .

emission is most efficient. Between  $q = 0$  and  $q = 1$  recoil is present, as expected. The maximum of  $v_k$  is at  $q = 0.(50 \pm 2)$  and  $\Delta$  strictly increases as we add mass to the smaller blob. The main difference in this case is that we have recoil for  $q = 1$ , since we have broken the symmetry of reflection with respect to  $z = 0$  of the BL-4 basis by adding an apex to it. Also, because the velocity of the smaller blob is aligned with the kick, we have again the “antikick” phenomenon for all values between  $q = 0$  and  $q = 1$ .

To end the examples, all values of  $v_k$  and  $\Delta$  for BL- $n$  pyramids initial data with equal  $\alpha_i$  and  $w_i$  parameters up to thirty vertices follow in Figure 33. In the graph, BL-3 is a degenerated case of pyramid and BL-8 has the highest recoil intensity. As stated in the end of section 4.3 for double pyramids,  $\Delta$  seems to slowly approach some value, but here we know that, even for arbitrarily large  $n$ ,  $\Delta$  will always be a finite amount lower than the regular polygons case, since some of the energy of the system must produce kick and the final Schwarzschild BH will have some kinetic energy at  $u \rightarrow \infty$ .

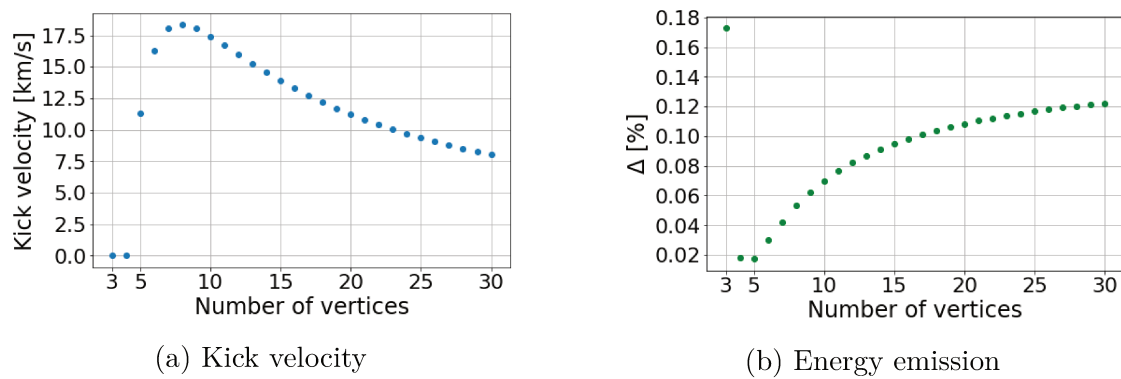


Figure 33 – Numerical calculations of  $\Delta$  and  $v_k$  for BL- $n$  pyramid initial data with blob velocities  $w_i = 0.8$  up to  $n = 30$ . The evolution was done with 2000 integration steps from  $u_0 = 0$  until  $u = (24m_0)^{-1}$ .

# Conclusion

In this work we studied compact sources of GWs, with focus on physical properties of RT spacetimes and their changes due to GW emission. We started with a historical [introduction](#) about the subject, that helped us to understand which tools we would need to develop in order to get the right calculations, and to interpret their physical meaning properly. We introduced those tools in [chapter 1](#) starting by Weyl scalars in [section 1.1](#), that helped us to determine which metrics could indeed represent an isolated system emitting GWs. In [section 1.2](#) GS-Theorem and  $(2 + 2)$  foliations gave us a natural coordinate system to study GWs, and also allowed us to understand the role of shear and twist of null congruences in spacetime. Then, in [section 1.3](#), the asymptotic behavior of shear led us to Bondi 4-momentum definitions and conservation laws, which showed us how to compute physical properties of the source. Finally, the most powerful tool studied was the BMS group in [section 1.4](#), which taught us the right way to fix all degrees of freedom in our initial data in order to determine Bondi momentum, and also explained how to perform any action of the Poincaré group on any asymptotically flat metric that can be written in Bondi coordinates.

In [chapter 2](#) we restricted ourselves to the simplest solution of Einstein’s equations for a compact body surrounded by GWs, the case of RT spacetimes. With the aid of rotations and Lorentz boosts generated by the BMS group, a definition of source velocity based on Bondi momentum was verified to be right in [section 2.1](#). Using the natural  $(2 + 2)$  foliation for the metric, we could look at RT equations as the evolution of an initial value problem in [section 2.2](#), and also presented its stationary solution, a Schwarzschild BH with constant velocity. In [section 2.3](#) we explained which kind of real systems could be described by RT spacetimes, and also got motivated with the “antikick” phenomenon for the post-merger phase of a binary collision of BHs. In [section 2.4](#) we briefly discuss the main restrictions on probing the global causal structure of RT spacetimes.

The last technical issue was the solution of the non-linear PDE evolution equation, and it was handled with a Galerkin spectral method in [chapter 3](#). Spherical harmonics were crucial not just to develop all strategies to build an algorithm that solves generic cases of initial conditions, but also to help understand any kind of simplifications that come from the symmetries of the system. Without the considerations stated in this chapter, any numerical calculation would take much more computational time and many results could not be attainable.

In [chapter 4](#) we discussed initial data, which encodes all connection with real physical systems. The BL initial data is the most well known case studied, representing the

post-merger phase of a binary head-on collision of BHs, so we started from it in order to investigate possibilities of real systems. In [section 4.1](#) we introduced the definition of blobs - based on their velocities - in order to better understand the axisymmetric case. Then, in [section 4.2](#), we used the Lorentz boost to analyze this binary collision in any reference frame, concluding that there was a mistake about the study of non-head-on collisions in previous literature, since the initial data studied in some works was just the frontal case, but written in a frame where the symmetry was not trivially recognized. In [section 4.3](#) we proposed an extension of previous initial conditions by adding more blobs to it, the BL- $n$  systems, that represent the post-merger phase of a head-on collision of  $n$  BHs. Along [chapter 4](#), we also calculated the fraction of energy emitted by GWs for many systems without recoil, computing mass consumption during the process. In each calculation we pointed direct connections between efficiency and curvature inhomogeneities, indicated by deviations from the sphere in Bondi mass aspect angular distributions in the center of mass frame.

In the last chapter, we settled down all strategies to develop the algorithms for numerical calculations and analyzed uncertainties involved in these computations ([section 5.1](#)). In [section 5.2](#), we used the programs to understand the importance of time variation in the notion of asymptotic reference frame during the emission process, which makes Bondi momentum comparisons really difficult to be evaluated for finite time distances. This effect has not been taken into consideration in some of numerical calculations in previous literature, leading to wrong physical interpretations. Then, in [section 5.3](#), we solved the BL-2 efficiency and recoil for all possible range of parameters, and also examined kick velocity and fraction of energy emitted for several BL- $n$  systems, getting some interesting cases involving inversion of recoil direction if the mass of some of the BHs involved were chosen to be smaller. All those examples led us to the connection between gravitational recoil and asymmetries in Bondi mass aspect angular distribution.

Finally, it is important to let it clear that we think BL- $n$  is a natural extension of ordinary BL initial data, since blob velocities transform exactly as ordinary velocities should do after Lorentz boosts, in the same way that happens for BL-2. Even so, we point the necessity of future works around BL- $n$  examples, in order to help probing their physical interpretation and potential to describe real systems.

# Bibliography

- [1] Heaviside, O. & Whittaker, E. *Electromagnetic Theory*, chap. Appendix B, 455 – 466. No. v. 1 in AMS Chelsea Publishing Series (American Mathematical Society, 1893). URL <https://books.google.com.br/books?id=Er0jVOHBQSYC>. Cited in page 15.
- [2] Poincaré, H. Sur la dynamique de l' electron. *Comptes rendus de l'Académie des Sciences* **140**, 1504 – 1508 (1905). Cited in page 15.
- [3] Einstein, A. Näherungsweise Integration der Feldgleichungen der Gravitation. *Sitzungsberichte der Königlich Preußischen Akademie der Wissenschaften (Berlin)* 688–696 (1916). Cited in page 15.
- [4] Carroll, S. M. *Spacetime and Geometry: An Introduction to General Relativity*, chap. 7, 274 – 322 (Cambridge University Press, 2019). Cited in page 15.
- [5] Kennefick, D. *Traveling at the Speed of Thought: Einstein and the Quest for Gravitational Waves* (Princeton University Press, 2007). URL <http://www.jstor.org/stable/j.ctt19w72w0>. Cited in page 15.
- [6] Einstein, A. & Rosen, N. On gravitational waves. *Journal of the Franklin Institute* **223**, 43 – 54 (1937). URL [https://doi.org/10.1016/S0016-0032\(37\)90583-0](https://doi.org/10.1016/S0016-0032(37)90583-0). Cited in page 15.
- [7] Pirani, F. A. E. Invariant formulation of gravitational radiation theory. *Phys. Rev.* **105**, 1089–1099 (1957). URL <https://link.aps.org/doi/10.1103/PhysRev.105.1089>. Cited 2 times in pages 15 and 16.
- [8] Petrov, A. *Einstein Spaces* (Pergamon, 1969). URL <https://doi.org/10.1016/C2013-0-02070-1>. Cited 2 times in pages 16 and 19.
- [9] Cervantes-Cota, J., Galindo-Uribarri, S. & Smoot, G. A brief history of gravitational waves. *Universe* **2**, 22 (2016). URL <https://doi.org/10.3390/universe2030022>. Cited in page 16.
- [10] Goldberg, J. N. & Sachs, R. K. Republication of: A theorem on Petrov types. *General Relativity and Gravitation* **41**, 434–444 (2009). URL <https://doi.org/10.1007/s10714-008-0722-5>. Cited 2 times in pages 16 and 24.
- [11] Bondi, H., Pirani, F. A. E. & Robinson, I. Gravitational waves in general relativity. III. Exact plane waves. *Proceedings of the Royal Society of London. Series A, Mathematical and Physical Sciences* **251**, 519 – 533 (1959). URL <https://doi.org/10.1098/rspa.1959.0124>. Cited in page 16.

- [12] Robinson, I. & Trautman, A. Spherical gravitational waves. *Phys. Rev. Lett.* **4**, 431–432 (1960). URL <https://link.aps.org/doi/10.1103/PhysRevLett.4.431>. Cited in page 16.
- [13] Sachs, R. Gravitational waves in general relativity. VI. The outgoing radiation condition. *Proc. R. Soc. Lond. A* **264**, 309–338 (1961). URL <http://doi.org/10.1098/rspa.1961.0202>. Cited in page 16.
- [14] Newman, E. & Penrose, R. An approach to gravitational radiation by a method of spin coefficients. *Journal of Mathematical Physics* **3**, 566–578 (1962). URL <https://doi.org/10.1063/1.1724257>. Cited 3 times in pages 16, 21, and 24.
- [15] Newman, E. T. & Tamburino, L. A. Empty space metrics containing hypersurface orthogonal geodesic rays. *Journal of Mathematical Physics* **3**, 902–907 (1962). URL <https://doi.org/10.1063/1.1724304>. Cited in page 16.
- [16] Robinson, I. & Trautman, A. Some spherical gravitational waves in general relativity. *Proc. R. Soc. Lond. A* **265**, 463–473 (1962). URL <http://doi.org/10.1098/rspa.1962.0036>. Cited in page 17.
- [17] Bondi, H. Gravitational waves in general relativity. *Nature* **186**, 535 (1960). URL <https://doi.org/10.1038/186535a0>. Cited in page 17.
- [18] Bondi, H., van der Burg, M. G. J. & Metzner, A. W. K. Gravitational waves in general relativity, VII. Waves from axi-symmetric isolated system. *Proc. R. Soc. Lond. A* **269**, 21–52 (1962). URL <http://doi.org/10.1098/rspa.1962.0161>. Cited in page 17.
- [19] Sachs, R. Gravitational waves in general relativity. VIII. Waves in asymptotically flat space-time. *Proc. R. Soc. Lond. A* **270**, 103–126 (1962). URL <http://doi.org/10.1098/rspa.1962.0206>. Cited in page 17.
- [20] Foster, J. & Newman, E. T. Note on the robinson-trautman solutions. *Journal of Mathematical Physics* **8**, 189–194 (1967). URL <https://doi.org/10.1063/1.1705185>. Cited in page 17.
- [21] Rendall, A. D. Existence and asymptotic properties of global solutions of the Robinson-Trautman equation. *Classical and Quantum Gravity* **5**, 1339–1347 (1988). URL <https://doi.org/10.1088/0264-9381/5/10/012>. Cited in page 17.
- [22] Singleton, D. On global existence and convergence of vacuum Robinson-Trautman solutions. *Classical and Quantum Gravity* **7**, 1333–1343 (1990). URL <https://doi.org/10.1088/0264-9381/7/8/012>. Cited in page 17.

- [23] Chruściel, P. T. Semi-global existence and convergence of solutions of the Robinson–Trautman (2-dimensional Calabi) equation. *Communications in Mathematical Physics* **37**, 289–313 (1991). URL <https://doi.org/10.1007/BF02431882>. Cited in page 17.
- [24] Prager, D. A. & Lun, A. W.-C. Numerical integration of the axisymmetric Robinson–Trautman equation by a spectral method. *The Journal of the Australian Mathematical Society. Series B. Applied Mathematics* **41**, 271–280 (1999). Cited in page 17.
- [25] Macedo, R. P. & Saa, A. Gravitational wave recoil in Robinson–Trautman spacetimes. *Physical Review D* **78** (2008). URL <http://dx.doi.org/10.1103/PhysRevD.78.104025>. Cited 3 times in pages 17, 33, and 35.
- [26] Aranha, R. F., Soares, I. D. a. & Tonini, E. V. Mass-energy radiative transfer and momentum extraction by gravitational wave emission in the collision of two black holes. *Phys. Rev. D* **81**, 104005 (2010). URL <https://link.aps.org/doi/10.1103/PhysRevD.81.104005>. Cited 4 times in pages 17, 35, 53, and 65.
- [27] Aranha, R. F., Soares, I. D. & Tonini, E. V. Mass-energy and momentum extraction by gravitational wave emission in the merger of two colliding black holes: The non-head-on case. *Physical Review D* **85** (2012). URL <http://dx.doi.org/10.1103/PhysRevD.85.024003>. Cited 6 times in pages 17, 44, 46, 48, 53, and 65.
- [28] Aranha, R. F., Soares, I. D. & Tonini, E. V. Gravitational wave recoils in non-axisymmetric Robinson–Trautman spacetimes. *The European Physical Journal C* **74** (2014). URL <http://dx.doi.org/10.1140/epjc/s10052-014-3097-7>. Cited 4 times in pages 17, 51, 53, and 65.
- [29] Batista, C. On the pursuit of generalizations for the Petrov classification and the Goldberg–Sachs theorem (2014). URL <https://arxiv.org/abs/1311.7110>. 1311.7110. Cited 2 times in pages 20 and 21.
- [30]ourgoulhon, E. 3+1 formalism and bases of numerical relativity (2007). <https://arxiv.org/abs/gr-qc/0703035>. Cited 2 times in pages 23 and 25.
- [31] Kinnersley, W. Type D vacuum metrics. *Journal of Mathematical Physics* **10**, 1195–1203 (1968). URL <https://doi.org/10.1063/1.1664958>. Cited in page 24.
- [32] Brewin, L. A simple expression for the ADM mass. *General Relativity and Gravitation* **39**, 521–528 (2007). URL <http://dx.doi.org/10.1007/s10714-007-0403-9>. Cited in page 25.
- [33] Mädler, T. & Winicour, J. Bondi–Sachs formalism. *Scholarpedia* **11**, 33528 (2016). URL <http://dx.doi.org/10.4249/scholarpedia.33528>. Cited in page 26.

- [34] Aranha, R. F., Soares, I. D. & Tonini, E. V. The Bondi-Sachs 4-momentum in non-axisymmetric Robinson-Trautman spacetimes. *Classical and Quantum Gravity* **30**, 025014 (2012). URL <https://doi.org/10.1088/0264-9381/30/2/025014>. Cited 3 times in pages 27, 34, and 37.
- [35] Newman, E. T. & Unti, T. W. J. Behavior of asymptotically flat empty spaces. *Journal of Mathematical Physics* **3**, 891–901 (1962). URL <https://doi.org/10.1063/1.1724303>. Cited in page 27.
- [36] Gallo, E., Lehner, L. & Moreschi, O. M. Estimating total momentum at finite distances. *Phys. Rev. D* **78**, 084027 (2008). URL <https://link.aps.org/doi/10.1103/PhysRevD.78.084027>. Cited 2 times in pages 28 and 65.
- [37] Boyle, M. Transformations of asymptotic gravitational-wave data. *Physical Review D* **93** (2016). URL <http://dx.doi.org/10.1103/PhysRevD.93.084031>. Cited in page 30.
- [38] Muller, R. A. The twin paradox in special relativity. *American Journal of Physics* **40**, 966–969 (1972). URL <https://doi.org/10.1119/1.1986722>. Cited in page 31.
- [39] Pasterski, S. Implications of superrotations. *Physics Reports* **829**, 1–35 (2019). URL <http://dx.doi.org/10.1016/j.physrep.2019.09.006>. Cited in page 32.
- [40] Rezzolla, L., Macedo, R. P. & Jaramillo, J. L. Understanding the “antikick” in the merger of binary black holes. *Physical Review Letters* **104** (2010). URL <http://dx.doi.org/10.1103/PhysRevLett.104.221101>. Cited 4 times in pages 35, 38, 39, and 40.
- [41] Bakas, I. The algebraic structure of geometric flows in two dimensions. *Journal of High Energy Physics* **2005**, 038–038 (2005). URL <http://dx.doi.org/10.1088/1126-6708/2005/10/038>. Cited in page 36.
- [42] Pollney, D. *et al.* Recoil velocities from equal-mass binary black-hole mergers: A systematic investigation of spin-orbit aligned configurations. *Physical Review D* **76** (2007). URL <http://dx.doi.org/10.1103/PhysRevD.76.124002>. Cited in page 39.
- [43] Holmes, P., Lumley, J. L. & Berkooz, G. *Galerkin projection*, 129–154. Cambridge Monographs on Mechanics (Cambridge University Press, 1996). URL <https://doi.org/10.1017/CB09780511622700>. Cited in page 43.
- [44] Jaramillo, J. L., Macedo, R. P., Moesta, P. & Rezzolla, L. Black-hole horizons as probes of black-hole dynamics. I. Post-merger recoil in head-on collisions. *Physical Review D* **85** (2012). URL <http://dx.doi.org/10.1103/PhysRevD.85.084030>. Cited 2 times in pages 52 and 69.

- 
- [45] Hannay, J. H. & Nye, J. F. Fibonacci numerical integration on a sphere. *Journal of Physics A: Mathematical and General* **37**, 11591–11601 (2004). URL <https://doi.org/10.1088/0305-4470/37/48/005>. Cited in page 59.

# Appendix

## APPENDIX A – Aberration of light effect

The aberration of light effect is a direct consequence of Lorentz spatial contraction and time dilation. It states that measurements of angles of light ray trajectories change for different inertial observers in Minkowski spacetime, even if their basis vectors  $(\hat{x}, \hat{y}, \hat{z})$  are aligned. To deduce it, we use a static rigid rod of length  $L$  seen by an inertial observer  $A$ . In the reference frame of  $A$  the rod is placed with one of its endings at the origin and with an angle  $\theta$  with respect to  $\hat{z}$ . An observer  $B$  with constant velocity  $v\hat{z}$  with respect to  $A$  will see the  $z$  component of this rod with smaller length, as pictured in Figure 34 bellow.

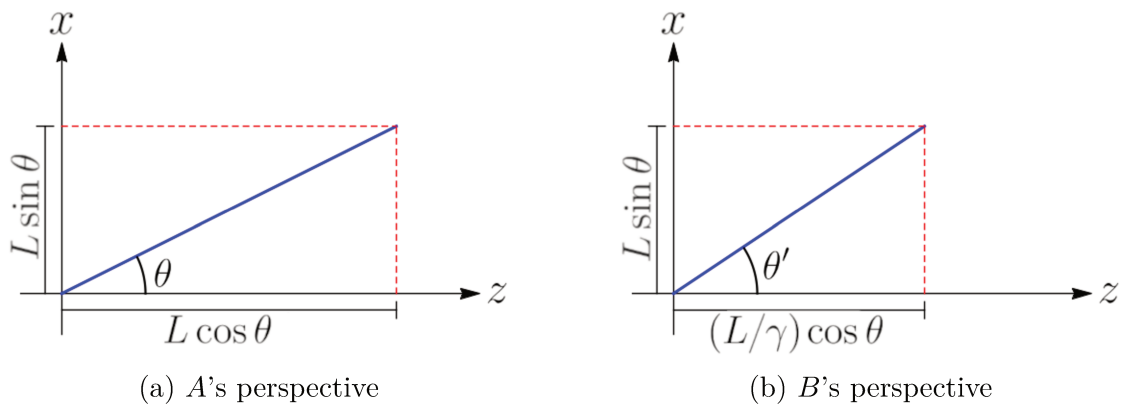


Figure 34 – Perspectives of the rod for each observer. The picture illustrates the change in angle to each observer's perspective.

The new angle  $\theta'$  that the rod makes with  $z$  will be given by

$$\sin \theta' = \frac{L \sin \theta}{\sqrt{L^2 \sin^2 \theta + (L/\gamma)^2 \cos^2 \theta}} = \frac{\sin \theta}{\sqrt{\sin^2 \theta + (1 - v^2) \cos^2 \theta}} = \frac{\sin \theta}{\sqrt{1 - v^2 \cos^2 \theta}}, \quad (\text{A.1})$$

where  $\gamma = (1 - v^2)^{-1/2}$  is the Lorentz factor.

Because of this fact, observers in different inertial frames will not agree with the predicted trajectory of light ray paths in each other frames. To see this, let  $A$  observe a spherical pulse of light emitted at the origin. He waits  $T$  seconds in order to the pulse radius to be at a distance  $L = T^1$ . We know that  $B$  will see a spherical pulse as well, but using Lorentz transformations we can determine how would  $A$  guess that  $B$  sees the pulse. The predicted angular distribution of the time that light rays arrive at  $L$  is

$$T' = \gamma(T + vL \cos \theta) = \gamma T(1 + v \cos \theta). \quad (\text{A.2})$$

Rotating  $v\hat{z}$  to a general direction  $v\hat{n}$ , (A.2) becomes

$$T' = \gamma T(1 + v\hat{n} \cdot \hat{r}), \quad (\text{A.3})$$

<sup>1</sup> Remember the speed of light is always set as  $c = 1$  in this work.

with  $\hat{\mathbf{r}}$  being the unitary radial vector.

With the information that speed of light is the same in all inertial frames, we can derive the spatial shape of the pulse  $A$  believes that  $B$  sees. Since

$$\frac{L}{T} = \frac{L'}{T'} = \frac{\sqrt{(L/\gamma)^2 \cos^2 \theta + L^2 \sin^2 \theta}}{T\gamma(1 + v \cos \theta)} = \frac{L \sqrt{1 - v^2 \cos^2 \theta}}{T \gamma(1 + v \cos \theta)}, \quad (\text{A.4})$$

we have that  $\sqrt{1 - v^2 \cos^2 \theta} = \gamma(1 + v \cos \theta)$ , leading (A.1) into

$$\sin \theta' = \frac{\sin \theta}{\gamma(1 + v \cos \theta)}, \quad (\text{A.5})$$

and this is the angle change between the frames for light rays. Using the fundamental equation of trigonometry, we write another equation

$$\cos \theta' = \frac{\cos \theta + v}{(1 + v \cos \theta)}. \quad (\text{A.6})$$

This makes possible to find an expression for the angular change in the light rays direction when  $B$  has velocity  $v\hat{\mathbf{n}}$  in any direction

$$\hat{\mathbf{r}}' = \frac{(\hat{\mathbf{n}} \cdot \hat{\mathbf{r}}) + v}{(1 + v\hat{\mathbf{n}} \cdot \hat{\mathbf{r}})} \hat{\mathbf{n}} + \frac{\hat{\mathbf{r}} - (\hat{\mathbf{n}} \cdot \hat{\mathbf{r}})\hat{\mathbf{n}}}{\gamma(1 + v\hat{\mathbf{n}} \cdot \hat{\mathbf{r}})}, \quad (\text{A.7})$$

which gives the predicted shape of the spherical pulse seen by  $B$ , but in the perspective of  $A$ .

# APPENDIX B – Selection rules for integration of the multiplication of many spherical harmonics

The integration of a product of  $N \geq 1$  spherical harmonics on the sphere,

$$I = \int_0^{2\pi} \int_0^\pi \prod_{i=1}^N Y_{l_i}^{m_i}(\theta, \phi) \sin \theta d\theta d\phi, \quad (\text{B.1})$$

has the following selection rules for non zero value of  $I$ :

$$L = \sum_{i=1}^N l_i \text{ is even,} \quad (\text{B.2})$$

$$\sum_{i=1}^N m_i = M = 0, \quad (\text{B.3})$$

$$\max\{l_i\} \leq L/2. \quad (\text{B.4})$$

The rules (B.2) and (B.3) are easy to justify by performing the  $\phi$  integration and the coordinate change  $x = \cos \theta$ , leading to

$$I = 2\pi \delta_{M,0} \int_{-1}^1 \prod_{i=1}^N \sqrt{\frac{(l_i - m_i)!}{(l_i + m_i)!}} P_{l_i}^{m_i}(x) dx, \quad (\text{B.5})$$

with  $M = \sum_{i=1}^N m_i$ . It is clear that (B.5) ends as an integral over the symmetric interval  $[-1, 1]$  and the integrand has the same parity of  $L$ , then only the even case is not null.

To prove (B.4) we need to consider 4 cases. For  $N = 1$  we know that only  $l_1 = 0$  is not null, so  $l_1 \leq l_1/2$  works. For  $N = 2$ , the orthogonality relation (3.3) demands  $l_1 = l_2 \implies \max(l_1, l_2) = \frac{l_1 + l_2}{2} \leq \frac{l_1 + l_2}{2}$ . For  $N = 3$  we use

$$Y_{l_1}^{m_1}(\theta, \phi) Y_{l_2}^{m_2}(\theta, \phi) = \sum_{k=|l_1-l_2|}^{l_1+l_2} \langle l_1, 0, l_2, 0 | k, 0 \rangle \langle l_1, m_1, l_2, m_2 | k, n \rangle Y_k^n(\theta, \phi), \quad (\text{B.6})$$

where the bracket terms are the usual Clebsch–Gordan coefficients, leading (B.1) to

$$I = \frac{4\pi(-1)^{m_3}}{2l_3 + 1} \langle l_1, 0, l_2, 0 | l_3, 0 \rangle \langle l_1, m_1, l_2, m_2 | l_3, -m_3 \rangle \quad (\text{B.7})$$

with the famous selection rules  $|l_1 - l_2| \leq l_3 \leq l_1 + l_2$ , which are equivalent to (B.4). For  $N > 3$  we first demand, without loss of generality,  $l_1 \leq l_2 \leq \dots \leq l_N$ , than let

$k_1 = l_1$ ,  $n_1 = m_1$  and one can write

$$I = \frac{4\pi(-1)^{m_N}}{2l_N + 1} \sum_{\{k_j\}} \prod_{i=1}^{N-2} \langle k_i, 0, l_{i+1}, 0 | k_{i+1}, 0 \rangle \langle k_i, n_i, l_{i+1}, m_{i+1} | k_{i+1}, n_{i+1} \rangle \quad (\text{B.8})$$

where  $2 \leq j \leq N - 2$ ,  $k_{N-1} = l_N$  and  $n_{N-1} = -m_N$ . Then, from each pair of Clebsch-Gordan coefficients we have  $k_{i+1} \leq l_{i+1} + k_i \implies l_N \leq \sum_{i=1}^{N-1} l_i \implies (\text{B.4})$ .